Universidade de Aveiro Departamento de Engenharia Ceramica e do Vidro
2010

Lingfei Zhang

Espumas e cerâmicos densos à base de Cordierite: preparação, caracterização e modelação

Foam and bulk cordierite ceramics: preparation, characterization and modelling

Universidade de Aveiro Departamento de Engenharia Ceramica e do Vidro
2010

Lingfei Zhang

Espumas e cerâmicos densos à base de Cordierite: preparação, caracterização e modelação

Foam and bulk cordierite ceramics: preparation, characterization and modelling

Dissertação apresentada à Universidade de Aveiro para cumprimento dos requisitos necessários à obtenção do grau de Mestrado em Ciência e Engenharia dos Materiais (EMMS), realizada sob a orientação científica do Professor Doutor Jose Maria Ferreira, Professor do Departamento de Engenharia Cerâmica da Universidade de Aveiro

Thesis submitted to University of Aveiro for fulfilment of the requirements for the degree of Master of (European Master in Material Science), held under the scientific guidance of Professor Dr. Jose Maria Ferreira, Professor of Department of Ceramics and Glass Engineering at University of Aveiro, Portugal

Acknowledgment

This Thesis was carried out under the guidance of supervisors, Professor Jose Maria Ferreira and Dr Susana Olhero. First of all I thank Professor Jose Maria Ferreira for offering me such as wonderful opportunity to do MSc research in his group. This opportunity to work with ceramics processing, characterization and modelling gives me tremendous benefit in strengthening my skills in material processing and modelling. Throughout the MSc thesis Professor Ferreira had gave me great help in experiment setup and discussion though he had an extreme busy schedule.

In the meantime, I worked with Dr Susana Olhero and she helped me wholeheartedly without any reservations. The experience working with such a wonderful person is memorable and beneficiary. Dr Olhero has trained me in all kinds of experiments and I would specially thank her for giving me training in ceramics suspension preparation and measurement of which I have been expecting for long time. I really thank for her advice and efforts.

Dr Fernando Oliveira at LNEG (National Laboratory of Energy and Geology) provided generous assistance in setting Impulse excitation of vibration measurement of Young's modulus of bulk and cellular ceramics.

The help from Professor Margarida Almeida is also important part of the success of this work in terms of administration. And the acknowledgement also goes to EMMS consortium that offered generous support in Scholarship which makes my memory stay in Portugal.

I also want to express my thanks for the staffs in my group who also offered me advice whenever they are available.

Finally, I wish to say thanks to my parents who support me spiritually and financially. There is one special person Miss Yujin Ham who accompanies me throughout my life with her endless love.

The Board of Examiners

presidente

Prof. Doutora Margarida Almeida
professor auxiliar da Universidade do Aveiro

Prof. Doutor José Maria Ferreira
professor associado da Universidade do Aveiro

Prof. Doutor Fernando Oliveira
Investigator principal com habilitação do LNEG, I.P.
professor associado do Instituto Superior Técnico

palavras-chave Cordierite, Cerâmica, estrutura celular e espuma, Impulse Excitação, o método de Mori-Tanaka, raios-X a tomografia computadorizada, quantitativos de Processamento de Imagem, Análise de Elementos Finitos.

resumo

Os materiais cerâmicos à base de cordierite são normalmente usados como materiais refractários devido às propriedades que possuem, tais como, excelente expansão térmica e elevada resistência ao choque térmico. Os pós precursores consistem numa composição estequeométrica de minerais à base de alumina, talco, α-quartzo, K-feldspato, caolinite e mulite, bem como uma pequena quantidade de calcite, cristobalite e fases vítreas derivadas da moloquite, obtidas pela calcinação da caolinite a elevadas temperaturas (1550ºC).

Os corpos em verde consolidados por enchimento por barbotina foram sinterizados ao ar a diferentes temperaturas: 1050, 1150, 1250, 1350, 1425 e 1500°C. Os resultados obtidos por difracção de Raios-X mostraram que a cristalização ocorre entre 1250 e 1350ºC e que a composição inclui não só cordierite mas também mulite, alumina e quartzo residual. Aumentando a temperatura de sinterização para 1500ºC, a única fase cristalina detectada é a mulite, juntamente com uma elevada fracção de porosidade envolta por uma abundante fase vítrea.

Além dos efeitos originados pela temperatura, a sinterização é também dependente do tempo. Por este motivo, o tratamento térmico foi efectuado ao fim de 2, 4 e 8 h de patamar de modo a relacionar as composições obtidas com o tempo de sinterização. As composições obtidas à base de cordierite-mulite-alumina apresentam baixo coeficiente de expansão térmico $2\sim4x10^{-6}$/K e resistência à flexão relativamente elevada, 90~120 MPa. As amostras sinterizadas a 1250ºC durante 2 e 4 h apresentam os valores mais elevados de resistência ao choque térmico (ΔT~350-400 K).

Além destas propriedades, os materiais à base de cordierite também apresentam baixa constante dieléctrica (entre 5 e 10) e um baixo factor de perda dieléctrica, o que faz deles materiais com forte potencial para aplicações em circuitos integrados como substratos dieléctricos. A constante dieléctrica em função da temperatura foi medida desde a temperatura ambiente até 600ºC, tendo-se verificado estabilidade das propriedades dieléctricas a 1 MHz em toda a gama de temperaturas testada.

As propriedades reológicas das suspensões à base de cordierite foram optimizadas de forma a obter uma boa impregnação do polímero. As propriedades mecânicas das espumas cerâmicas obtidas pelo método de replicação da espuma polimérica foram caracterizadas com base nas propriedades dos cerâmicos densos. O módulo de Young foi determinado pelo método de excitação por impulso. A teoria micro-mecânica para materiais heterogéneos conhecida como método de “Mori-Tanaka” foi aplicada para estimar o módulo efectivo das espumas cerâmicas. Dos resultados obtidos verifica-se um desfasamento entre os valores experimentais (1~2 GPa) e os teóricos (6~7 GPa). A tomografia computadorizada por Rais-X foi usada para estudar a estrutura tridimensional (3D) das espumas cerâmicas por análise de elementos finitos (FEA). As propriedades elásticas foram estudadas pelo cálculo da força de reacção na deformação elástica. Embora a estrutura tridimensional calculada das espumas cerâmicas represente apenas uma pequena fracção da estrutura, os resultados mostram que a correlação entre eles é fortemente melhorada pelo método de Mori-Tanak. A razão apontada para o desfasamento é a existência de uma estrutura interna oca, que não é tida em conta no modelo utilizado. Por outro lado, o método CT mostra que a estrutura porosa e a diferença no microestrutura poderá também ser simulada. O resultado da análise de elementos finitos mostrou que as espumas cerâmicas são muito quebradiças, o que é consistente com a observação experimental obtida nos testes de compressão.

keywords Cordierite, Ceramics, Cellular structure & foam, Impulse Excitation method, Mori-Tanaka method, X-ray Computed Tomography, Finite Element Analysis.

abstract

Cordierite ceramics have excellent thermal expansion and thermal shock resistance for applications such as refractory materials. The precursor powder consisted of a non-stoichiometric composition of minerals containing corundum, talc, α-quartz, K-feldspar, kaolinite and mullite as well as small amount of calcite, Cristobalite and glass phases probably derived from molochite, produced by calcining kaolinite at high temperature (1550 ºC). The green consolidates were sintered in air at 1050, 1150, 1250, 1350, 1425 and 1500°C. It was discovered by XRD that cordierite crystallization takes place between 1250 ^{o}C and 1350 ^{o}C while the composition includes not only cordierite but also mullite and alumina and residual quartz. At 1425^{o}C, the ceramics consisted of cordierite and mullite. With further increasing the sintering temperature to 1500 ^{o}C mullite was the single crystalline phase detected, together with a high porosity fraction embedded in an abundant glassy phase. Besides the temperature effects, sintering was also time-dependent, therefore heat treatment was conducted for 2, 4 and 8 h to study the sintering time–composition relationships. The cordierite-mullite-alumina heterogeneous ceramics were obtained with low thermal expansion coefficient of 2~4x10^{-6}/K and relatively high flexural strength of 90~120 MPa. Thermal shock resistance measurements demonstrated that the samples sintered at 1250 ^{o}C for 2 h and 4 h exhibited the highest thermal shock resistance values (ΔT~350-400 K).

Cordierite ceramics also exhibited very low dielectric constant (between 5 and 10) and low dielectric loss factor, showing a good potential for low dielectric substrate applications in integrated circuits. The dielectric constant as function of temperature was measured from RT to 600^{o}C, demonstrating to have very stable dielectric properties at 1 MHz across the entire temperature range.

The cordierite slurries were prepared with optimized rheological properties and impregnation conditions to coat the polymer struts by dip casting. The mechanical properties of ceramics foams fabricated by polymer replica method were characterised on basis of properties of bulk ceramics. The foam's effective Young's modulus was determined by Impulse excitation method. Micro-mechanical theory for heterogeneous material known as "Mori-Tanaka" method was applied to model the effective modulus of ceramics foam. The results showed that the agreement was not good between experimental (1~2 GPa) and modelling (6~7 GPa) data. In the meantime, Computed X-ray tomography was applied to study the actual 3D structure of ceramic foams for Finite Element Analysis (FEA). Elastic properties were studied by calculating the reaction force in elastic deformation. Although the calculated 3D structure of the ceramic foams represents only small fraction of the structure, the results showed that the agreement has greatly improved over Mori-Tanaka method. The reason of disagreement from the former method is the existence of internal hollow structure in ceramics struts, which is not taken into account in the model. On the other hand, CT method revealed the hollowed structure and the influence of such microstructure could be simulated. The FEA also showed that the ceramic foams are very brittle, which is consistent with the experimental observation under compression tests.

Table of Contents

List of Figures

Chapter 1

Chapter 2

Chapter 3

Chapter 4

List of Tables

Chapter 1: Introduction

1.1 MgO-Al_2O3-SiO_2 (MAS) system

MgO-Al_2O_3-SiO_2 (MAS) system is one of the most important mineral systems due to its abundance in Earth crust and mantle at ~ 88 wt.% (*wikipedia*). It has wide-ranging of industrial applications such as filler for joining SiC with excellent properties of wetting on SiC substrate which produced high flexural strength (342-480 MPa) up to high temperature of 800 ^oC [1]; kiln furniture due to their low density, good mechanical strength, incompressibility and thermal insulation properties; catalyst support [2, 3] as well as refractory material to develop components in rocket nozzle and coatings on turbine gas engine thanks to its excellent thermal shock resistance [4]. In recent years, this class of materials has attracted an increasing attention from foundry industry owing to the fact that ceramics foam made of MAS ceramics could be used as filters to molten metals in casting processes to increase the homogeneity and stability of the metal flow. Among them, cordierite ceramics is an interesting phase due to its excellent thermo-mechanical properties. Cordierite is a high temperature phase in MAS phase-temperature-composition diagram which was firstly studied by Rankin et al [5] in 1918. Therefore, cordierite ceramics are not so popular and in most cases they are only found in nature nearer volcanoes where high temperature is available. In Fig. 1.1 an illustration of MAS ternary phase diagram (TPD) is shown and several key phases are highlighted.

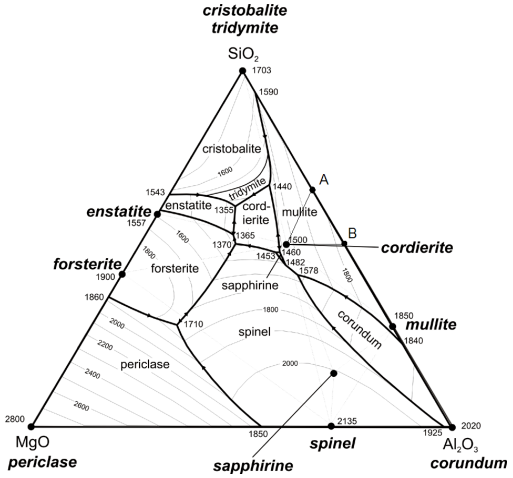

Fig. 1.1: Ternary Phase Diagrams for Ceramicists [6]

The TPD shows that upon compositions and temperatures, cordierite can transform into

mullite or co-exist with alumina. The stoichiometry based on TPD in Fig. 1.1 shows monolithic cordierite has molar ratio of $2MgO:2Al_2O_3:5SiO_2$, hence the chemical formula of cordierite is $Mg_2Al_4Si_5O_{18}$. This corresponding to a composition of 13.7 wt.% MgO, 34.9 wt.% Al2O3 and 51.4 wt.% SiO2. Under stoichiometric condition, the cordierite is crystallized at temperature around 1460 K or 1187 ^oC. However, most synthesis usually starts from powders of non-stoichiometric composition; consequently, cordierite, α-quartz, corundum and mullite are likely to co-exist with different heating schedules. Composite of cordierite and mullite are most likely seen co-existing due to Mg-deficiency in the precursor and they are similar in physical properties, but very different in mechanical and thermal expansion coefficients. The summary of properties of Cordierite and Mullite as well as two other MAS materials, Corundum and α-quartz are given in Table 1.1 (next page).

Logvinkov et al [7] studied the phase transition between corundum, mullite and cordierite under heat treatment. The study analyzed the phase composition after heat treatment for 2h at 1400 ^oC, 1450 ^oC and 1500 ^oC and cooled with various procedures. The heat treatment temperatures correspond to the subsolidus in phase diagram as seen in Fig. 1.1. In [7] the phase transition take places around subsolidus region and the solid state chemical reaction at four generic temperature ranges are summarized below:

(1) $T \leqq 988\ ^oC$:

$$10MgSiO_3+2MgO\text{-}Al_2O_3=5Mg_2SiO_4\ (\textit{forsterite})+ Mg_2Al_4Si_5O_{18}\ (\textit{Cordierite})$$

(2) $988\ ^oC<T<1386\ ^oC$:

$$2Mg_2Al_4Si_5O_{18}+15Al_2O_3=4MgAl_2O_4\ (\textit{Spinel})+5Al_6Si_2O_{13}(\textit{Mullite})$$

(3) $1386\ ^oC<T<1460\ ^oC$:

$$4Al_6Si_2O_{13}+ Mg_4Al_{10}Si_2O_{23}(\textit{Sapphirine})=13Al_2O_3+2Mg_2Al_4Si_5O_{18}$$

(4) $T>1460\ ^oC$:

$$4MgAl_2O_4+ Al_6Si_2O_{13}=2Al_2O_3+ Mg_4Al_{10}Si_2O_{23}$$

It appears that cordierite can be obtained at lower temperature. However, the aforementioned solid state reaction route is on assumption that precursor materials are pure oxides. In real cases, the non-stoichiometry in precursor powder could cause significantly altered results of final composition, for instance the cordierite will not be found around 1000 ^oC in reaction (1); Spinel is also limited to form in reaction (2) which causes deficiency of spinel in reaction (4). Therefore the final composition above 1460 ^oC is pure mullite without Sapphirine.

Table 1.1: Physica, Mechanical, Thermal and Electrical properties MAS minerals [8]

Mineral name	***Corundum(99.5%)***	***α-Quartz***	***Mullite***	***Cordierite***
Physical				
Chemical Formula	Al_2O_3	SiO_2	$3Al_2O_3$-SiO_2	$2MgO$-$2Al_2O_3$-$5SiO_2$
Density, g/cm^3	3.89**	2.21	2.8	2.6
Water Absorption wt.% (R.T.)	0.5 - 3.0	0	0	0.02 - 3.2
Hardness, Moh's	1.0 - 1.5	7	8	7
Mechanical				
Compressive Strength, MPa	2600	650 - 1100	551	350
Tensile Strength, MPa	4.8	48	103.5	25.5
Modulus of Elasticity, GPa	375**	70	150	70
Flexural Strength (MOR), MPa	379**	80	170	117
Poisson's Ratio, ν	0.22**	0.17	0.25	0.21
Fracture Toughness, KIc, MPa x m$^{1/2}$	4**	-	2	--
Thermal				
Max. Use Temperature (* denotes inert atm.), ºC	1750**	1200	1700	1371
Thermal Shock Resistance, ΔT (ºC)	200-250	> 1400	300	500
Thermal Conductivity, W/m-K	24	1.4	3.5	3
Thermal Expansion Coefficient, (25 ºC-1000 ºC) 10^{-6}/K	8.39	0.45	5.3	1.7
Specific Heat, cp, cal/g-ºC	0.16	0.16	0.23	0.35
Electrical				
Dielectric Constant,1MHz	9.8**	3.8	6	4.7
Dielectric Strength, kV/mm	0.0002**	25 - 40	9.8	5.11
Electrical Resistivity, Ωcm	7 x 10^{14}**	6 x 10^{10}	10^{13}	10^{14}

*Although we have no reason to doubt the accuracy of the data presented, Ferro-Ceramic Grinding Inc. offers this information for comparison only, and disclaims any and all liability from error, omissions or inaccuracies, such that it does not constitute a warranty or representation for which we shall assume legal responsibility. http://www.ferroceramic.com/Cordierite_table.htm
**: data source: http://www.accuratus.com/alumox.html

In general, the equations above are used as guidelines only and not applicable to the powder with non-stoichiometric compositions. In addition to this, some phases in Fig. 1.1 are not stable at

ambient pressure for instance, enstatite+sapphirine+quartz could co-exists and stable at high pressure above 6 kbar while only cordierite and mullite phases are stable to co-exist at ambient pressure [9].

1.2 Cordierite

Cordierite was discovered by the French geologist Cordier in 1913 and named after him. Cordierite is considered as one of the potential materials to fabricate the advanced ceramics component in refractory environment and electronic industry due to its high modulus (~100 GPa), thermal shock resistance ($\Delta T>500$ K) properties, low thermal expansion coefficient (TEC) (~$1.5x10^{-6}$/K) and low dielectric constant as well as loss factor plus potential replacement materials for SiO_2 as substrate in electronic industry due to its similar TEC to silicon.

The thermal properties of cordierite depend on its crystal structure shown in Fig. 1.2. Literature reports refer to two crystal systems. Low temperature cordierite has a completely ordered orthorhombic structure (Cccm) with unit cell parameter a~17.06 Å, b~9.74 Å, c~9.34 Å, α=90, β=90, γ=90, [10-12]. At higher temperature it transforms into a hexagonal structure (P6/mmc) with lattice parameters a~9.7437 Å, b~9.7437 Å, c~9.3893 Å, α=90, β=90, γ=120 [10, 13] with long range ordering of Al and Si stable at about 1450 °C, before melting at 1460 °C. The unit cells of two crystal systems are shown in Fig. 1.2 respectively. The low temperature phase is metastable high quartz solid solution, commonly referred to μ-cordierite and its high temperature phase is known as α-cordierite with hexagonal structure that very slowly transforms to orthorhombic cordierite below 1450 ^{o}C following the crystallization of μ-cordierite [10].

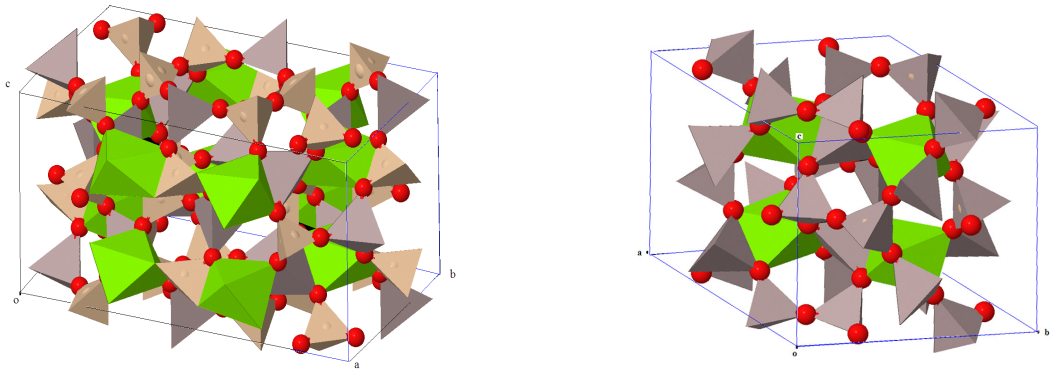

Fig.1.2: crystal structure: (left) orthorhombic, μ-phase; (right) hexagonal, α-phase;

The unit cell consists of octahedrons of Mg coordinated by 6 oxygen and tetrahedrons centred at Si and Al that are coordinated by 4 oxygens. However the octahedron and tetrahedron are geometrically asymmetric with different Mg-O-Mg, Al-O-Al or O-Mg-O and O-Al-O bond angles indicated in Fig. 1.3. The angle between the O and Al are 97.36°, 110.15° and 121.83° respectively. The Si atoms are also coordinated in tetrahedral structure however the distortion of the tetrahedron is less than that of Al-coordinated tetrahedrons. The angle between oxygen and silicon in tetrahedron are 108.67°, 110.40°, 110.34°. The octahedrons and tetrahedrons are interconnected within each other and form a complex molecular ring network shown in Fig. 1.4. The cordierite structure usually gives its bulk density (~2.5 g/cm^3).

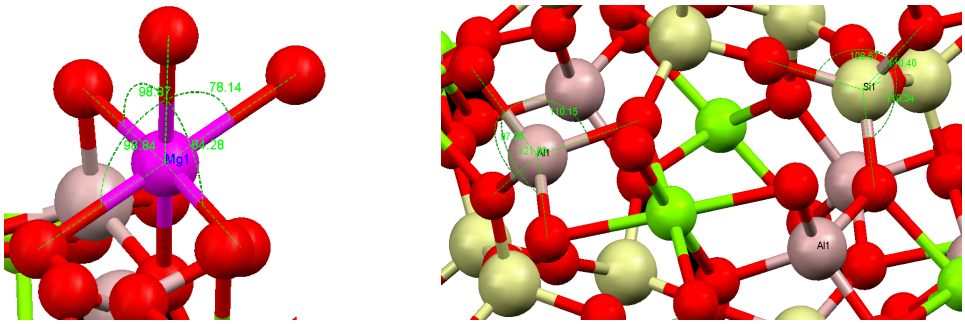

Fig. 1.3: (left) Mg-coordinated octahedrons; (right) Al-coordinated tetrahedrons and Si-coordinated tetrahedrons

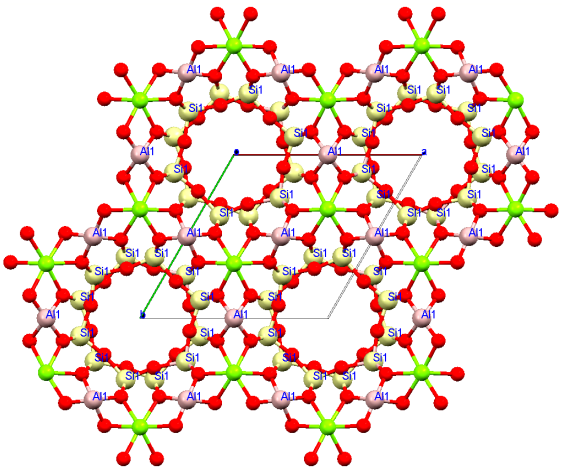

Fig. 1.4: overview of α-cordierite crystal structure from c-axis of the unit cell

The low thermal expansion coefficient of α-cordierite is the result of its relatively 'flexible' tetrahedral ring framework, and the anisotropic expansion of the octahedral framework of α-cordierite structure [11]. On the other hand, the ring structure-property relation was studied by Mirwald et al [12] from XRD data revealing that low thermal expansion is due to the ring rather

than silicates framework. No indication for structural modifications correlated with symmetry changes was observed during heating. Hochella et al [13] attempted to correlate the thermal expansion properties of cordierite with structural changes as a function of increasing temperature. The result was found that the expansion of a particular silicate framework depends on the temperature response of the framework itself involving Al–O–Al and O–Al–O angular changes, the expansion coefficient(s) of the non-tetrahedral bonds, if present, and the interplay between these two factors. This interplay of the tetrahedral framework is associated with the change in bond angles contributing towards lower expansion in space. The general idea is rather similar that cordierite structure has tetrahedral unit with different angles of O-Al-O/Al-O-Al as well as octahedral unit with variable angle of Mg-O-Mg and O-Mg-O as shown in Fig. 1.3. The structure is very flexible to re-arrange in space upon heating the interatomic distance is likely to increase however the increase will not result in volume due to re-arrangement of the tetrahedral and octahedral units. This gives cordierite very low expansion in volume upon heating compared to other mineral with more rigid structure i.e., Alumina or metals. However, one exception is that diamond has also very low TEC~$1x10^{-6}$/K and this is due to strong C-C bond which is highly resistant to thermal excitation. Hochella & Brown's attempt to correlated the very low TEC of cordierite to silicate framework structure in terms of stuffing cation (Mg in case of cordierite) and bond angles in the tetrahedral framework could not find a general mechanism for framework structure-thermal expansion relationship and concluded that the thermal expansion in cordierite is complex and variable [13]. Later, Roy et al [14] revisited the works in very low thermal expansion materials and claimed that the Mg stuffing plays a direct role in controlling thermal expansion because of large variation of Mg-O bond. Furthermore, they discussed that the key features that very low thermal expansion materials such as cordierite must have are: i) presence of structural holes, ii) flexible but rigid network of strongly bonded polyhedron. These are two main criteria for very low thermal expansion materials that cordierite satisfies both of them.

Cordierite ceramics found important applications in thermal-mechanical engineering used as refractory materials with the "Maximum use Temperature" up to 1371 ^{o}C (Table 1.1). It also shows excellent thermal shock resistance (TSR) behaviour as Oliveira et al [15] studied dense and foam's TSR by rapidly transferring the specimens from resistance furnace into distilled water and measured the retained flexural strength. The dense cordierite ceramics show half way reduction (67 to 40 MPa) of flexural strength at ΔT~325 K; and the flexural strength dropped to 1/3 or 1/4 of original value at ΔT=375 K [15]. Acimovic et al [16] studied the application of cordierite ceramics in foundry and parameters in producing refractory coating for sand mold. However, to the best knowledge of the author [16] the cordierite ceramics has not been put into any foundry application yet. Kaolinite based Cordierite was synthesized by Yamuna et al [17] and used as

materials for exhaust converter core thus extending the potential applications of Cordierite to environmental protection.

Apart from thermo-mechanical engineering applications, cordierite also has high potential in electronic packaging. Modern electronics industry requires smaller scale integrated circuit (IC) therefore capacitor has to be smaller in distance. This will increase the capacitance dramatically and the charge collected at the capacitor will affect the operation of the IC. The industry has been looking for replacement to SiO_2 that currently being used as IC material with lower dielectric constant and dissipation factor compensate the smaller distance. Cordierite is considered as one of candidate materials due to its low dielectric constant, e.g. ε_r=5 at 1 MHz and similar thermal coefficient expansion of $3x10^{-6}$/K to single crystal silicon [18] plus stronger flexural strength (100 MPa) compared to SiO_2 substrate. More recently, research on cordierite electronic application has been done and a very low dielectric constant (5.0-5.2) and dielectric loss (<0.008) [19, 20] were achieved from a batch sintered at 950 ^oC doped with 1.5 wt.%-3.0 wt.% ZnO [21, 22]. The thermal coefficient ($3.6\text{-}4.8x10^{-6}$/K) matches well that of silicon which promises better electronic packaging than when SiO_2 is used as substrate. The cordierite has low dielectric constant, which is also considered as an important requirement for mm-microwave dielectrics such as in [23] that Ni-substituted respective to Mg, namely $(Mg_{1-x}Ni_x)2Al_4Si_5O_{18}$ cordierite has microwave properties such as relative lower dielectric constant (6-11), very high quality factor up to 99,110 GHz (Q x *f*) as well as nearly zero temperature coefficient of resonant frequency and so on. On the other hand, one of successful candidates to replace traditional SiO_2 material is developed by Applied Materials, "Black diamond" which has been used in the IC industry. However, Cordierite has not only low-ε but also strong mechanical strength, thermal and chemical resistance and stability. Therefore the potential of cordierite in IC industry is still a hot topic nowadays.

The synthesis of cordierite has been a challenge due to high temperature required and porosity removal during heat treatment. However cordierite sinterability was also found not good due to narrow range of sintering temperature [24]. Tummala et al [25] reported that completed densification is achieved for cordierite glass powder by melting a mixture of the raw ingredients of given composition (13 wt.% MgO, 27 wt.% Al_2O_3 and 60 wt.% SiO_2) in alumina crucibles at 1500 ^oC for 2 h until it was completely homogenized. The molten glass was water quenched to form ''cullets''. The cullets have to be further ball milled with two steps to an average particle size around 2 mm. The sintering agent P_2O_5, B_2O_3 (B_2O_3 and P_2O_5<5 wt.%) was employed to reduce sintering temperature between 900-950 ^oC. Similarly Nandi studied glass frit preparation [26]. Kumar et al [18] studied and claimed that improved sinterability can be obtained by two approaches either changing the glass compositions with excess MgO [27] and less Al_2O_3 or

adding sintering aids such as P_2O_5 and B_2O_3. Chen [21] studied the addition of ZnO wt.% on crystallization behaviour in cordierite sintering and properties. Chen found that with increasing ZnO the batch melting temperature, glass transition temperature and crystallization temperature all decreases. Meanwhile, another method recently appeared to lower the sintering temperature is to based on sol-gel derived cordierite glass and the results showed the sintering temperature decreased below 1000 ^{o}C [20]. The starting agent of synthesis of cordierite could be mixture of stoichiometric pure MAS oxides however most works were more interested in using non-standard mixture of natural clays such as kaolin, talc and corundum [28]. Although using mixture of natural materials poses a problem of composition control however the saving of production cost from pure oxides is significant appealing factor that drives the research in understanding of behaviour and sintering schedule. In summary, the cordierite could be synthesized by glass crystallization method [11, 26, 29], sol-gel method, or solid-state reaction. However, the first two methods are not suitable for industrial scale production due to involved high cost reagents or more complicated synthesis procedures. Although the pure oxides with stoichiometric mixture yield high efficiency of production but the cost effectiveness drives the work of studying compositional variation effect from natural materials [30].

1.3 Mullite

In the MgO-SiO_2-Al_2O_3 phase diagram (Fig. 1.1), pure oxides of MgO, SiO_2 and Al_2O_3 could crystallise into other MAS minerals with different stoichiometric compositions at different temperatures. This is more perplexing in our investigation since the original cordierite precursor powder is made of natural materials with non-stoichiometric compositions. The composition of other minerals in the sintered sample has a significant influence on the thermal-mechanical properties such as thermal expansion, electrical and shock resistance. One of the most dominant phases which co-exist with cordierite at high temperature is Mullite, $Al_6Si_2O_{13}$ or $3Al_2O_3$-$2SiO_2$. The unit cell of mullite is shown in Fig. 1.5.

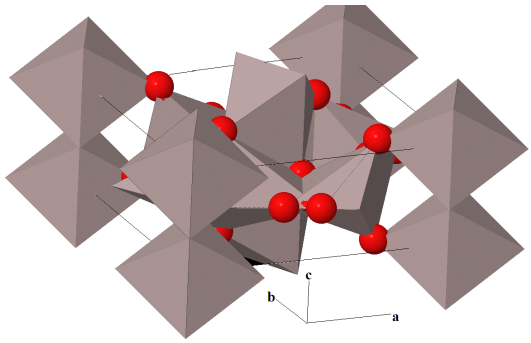

Fig. 1.5: crystal structure of mullite's unit cell

The most noticeable use of mullite is related to its refractory properties with melting point at 1840 ^{o}C. Mullite is also known as Aluminium silicate which is rare mineral on earth naturally formed and mostly from post-clay genesis. Mullite becomes dominating phase at high temperature above 1500 ^{o}C in case of Mg deficiency since cordierite or other phase has melt. Therefore it is most seen in nature near to volcanic site where it was firstly discovered in 1924 in volcanic rock in Scotland.

Mullite has two morphologies in platelet shape and needle shape. The needle shape mullite is desirable to be formed in cordierite ceramics matrix during heat treatment since it has beneficiary effect on increasing the fracture strength and thermal shock resistance over long cycle and large load [31]. The most important condition to form needle shape reinforced ceramics lying with the composition of silica and alumina and temperature as well as the environment being either reductive or oxygenated. When the composition and sintering gas environment are adjusted to desirable values needle mullite will form at 1200 ^{o}C [31] and the needles will interlock thus increasing the fracture strength. This potential increase of mechanical fracture strength has important implication in reinforcing the brittle porcelain. The formation of needle (tubular) shape mullite depends on the presence of crystallization centres which are often impurities. Pitak et al [31] studied the high temperature performance of materials consisting of needle shape mullite and showed it is an excellent structural material. The specimen consisting needle shape mullite from molten kaolin softens under load of 0.2 MPa at 1750 ^{o}C while the creep under the same load after 10 h hold is zero. However the sintered kaolin with 12% porosity shows softening at 1520 ^{o}C and 15% creep at 1200 ^{o}C with the same load.

1.4 Composite ceramics

Although there are many advantages (high modulus, hardness, chemical resistance, low thermal expansion and good refractoriness) of using ceramics as highly effectively structural materials, they also present some negative aspects. One of most noticeable disadvantages is the severely underestimated strength of ceramics, which is between 1/10 and 1/100 of the theoretical value predicted from interatomic bonding strength. This phenomenon has been explained in A. A. Griffith's theoretical fracture strength equation considering the existence of flaws, and the brittleness was explained as consequence of increased stress concentration in vicinity of micro-cracks or pores [32] given by:

$$\sigma_c = \left(\frac{2E\gamma_S}{\pi a} \right)^{1/2} \quad (1.1)$$

Where E is the elastic modulus of fully dense material; γ_S is the specific surface energy; and *a* is half length of internal crack. From this equation one can see that bigger the internal crack is, easier the ceramics will break. Equation (1.1) also implies that the fracture strength for ceramics materials is not likely the same due to statistical distribution of the micro-crack length. Apart from this, ceramics also presents image of being weak in shear and tension, brittle with K_{Ic} in region 1-12 MPa $m^{1/2}$ compared to Al alloys have K_{Ic} =25-50 MPa $m^{1/2}$. The brittleness of ceramics is due to the ionic bond that has much less flexibility to deform plastically compared to non-brittle materials e.g. metals. When the bond is broken the structure will completely fail. It is unlikely to change the interatomic bond nature however it is possible to add second phase to modify the ceramics materials. Therefore the development was focused on combining the advantages while reducing the drawbacks by reinforcing the ceramics with less hard but more plastic materials in order to relieve the stress concentrated around crack to maintain the structure in avoiding catastrophic failure.

Composite materials have attracted strong interests due to the nature that composite could combine two materials advantages and reduce or minimise the disadvantages from each phases. An example of composite is designed by using nanoparticles e.g., carbon nanotubes (~10^{-9} m) as reinforcing phase to modify and improve the physical or mechanical properties of matrices for instance polymer without sacrificing its lightweight property. The fact that addition of only small amount of CNTs induces an significant improvement on macro-scale properties has made nanocomposites highly attractive new classes of lightweight, high strength and multifunctional materials [33]. Polymer nanocomposites have achieved such success being reinforced with a wide variety of different nanoparticles and CNTs.

However, the idea of dispersing high modulus/strength CNT in cordierite or other ceramics faces difficulties in processing due to the fact that the CNT will likely decompose and react with oxygen-containing ceramics above 600 ^oC. In addition to this, CNTs are hydrophobic without surface chemistry modification in polar liquid such as water and most polymer resins. These cause a poor dispersion of CNTs in aqueous ceramics slurry which results in much lower mechanical properties enhancement than expected. Therefore, the carbon oxidation during sintering and adverse effect of poor dispersion hinders the development to obtain high mechanical properties of CNT reinforced ceramics composites. Despite this, CNT has been found successfully applied in pure metal, Aluminium [34, 35] and [36]; more recently, in non-oxygenated ceramics system for fracture toughening such as ZrB_2-SiC [37], Si_3N_4 [38]; Cho et al [39] reviewed the progress the CNT-loaded ceramic composite.; It is noteworthy that Estili et al [40, 41] claimed that reinforcement of oxygen containing ceramics α-alumina with CNT has

been successful by Spark plasma sintering (SPS). The SPS method enabled to avoid the problem of CNT oxidation [42]: The sintering was carried out at 1350 ^{o}C and the heating rate is 100 ^{o}C/min; The holding time at 1350 ^{o}C was 12 min; and the SPS was also in hot isostatic pressing condition with applied pressure of 75 MPa. The vacuum is 1.8 Pa or 1.8×10^{-5} bar. The sintering Die and punches are made of graphite resulting in a reductive atmosphere during sintering. The sample relative density was 100%. Very recently, an very interesting result has been reported by Wang et al [43] regarding the reinforcement of mullite ceramics matrix with CNT by hot pressing sintering. This is considered a breakthrough in terms of oxygen-containing ceramics reinforcement with CNT loading. The result in [43] showed the sample was sintered at 1600 ^{o}C with 5 vol.% of MWNT leading to 10% increase in bending strength and 78% increase in fracture toughness. The preparation was performed using hot pressing in Ar atmosphere at 30 MPa in graphite die at 1500, 1550, 1600 and 1650 ^{o}C for 1 h and the aim was to compare the mechanical properties of pure mullite prepared under the same conditions. Despite, the result in term of mechanical properties improvement is sceptical due to large error. However SEM images shows that CNT is not degraded in mullite matrix under Ar gas protection above 1500 ^{o}C. Despite the success claimed by the author, the mechanical properties were seen decreased at 1650 ^{o}C with the same CNT loading, which was not be able to explain well. Anyhow provided a hint to continue CNT-loaded cordierite composite research via conventional heat treatment route instead of SPS route in Estili et al work [40, 42].

To the best knowledge of the author, there is no report related to CNT-loaded composite ceramics with cordierite as primary phase. A wide-ranging ceramics-ceramics composites for cordierite were developed with modifying phases such as AlN [44, 45] (show optimum content of AlN for best mechanical performance with low-k and thermal stability). Studies on mechanical, electrical and thermal properties of cordierite composite have also appeared with other ceramics reinforcing or modifying phases such as Mullite [46-53], Zirconia [54-56], alumina [57] or alumina fibre [58], Mica [59], glass [60, 61], glass-fibre [62], forsterite (spinel) [63] as well as silicon carbide [64, 65] and SiC whisker [66] or SiC platelets, particles [67]. SiC was found very effective to reinforce the cordierite's fracture toughness from less than 2 MPa$^{1/2}$ to 3.5 MPa$^{1/2}$ with 30 vol% SiC whisker while the fracture strength was found the most effectively reinforced by adding SiC particles instead of whiskers from 170 MPa to 270 MPa while the SiC whisker addition at 30 vol% reinforced the fracture strength only up to 230 MPa [67]. Meanwhile SiC is also studied by Liu and Zhu et al [65, 68] to produce porous foam however the SiC foam requires high sintering temperature above 2100 ^{o}C which limits its application. Various ceramics are considered as bonding agents to fabricate the SiC foam among which Cordierite is considered one of the best candidates to sinter SiC foam at lower temperature.

Cordierite-mullite composite is often found in the literature used for refractory application. The mullite has different morphology and the shape of mullite grain appeared to be very influential to the cordierite-mullite composite [53]. Ibrahim showed [69] that excessive corundum is added in order to produce the required mechanical properties. The thermal shock resistance of cordierite composite according to ASTM standard by water quench test to ceramics body heated at 950 ^{o}C for 15 min and repeat this until the ceramics body fails. The sample showed excellent thermal shock resistance until 36 cycles [70]. Ozel et al [51] studied the processing of cordierite-mullite composite by tape casting or mixed with pre-produced mullite powder into cordierite starting powders. Their results showed that the mixing of mullite powder produced stronger strength of composite in the cordierite slip casting process due to better densification. The cordierite-mullite has also presented interesting electrical properties. The electrical properties as function of volume fraction of mullite in cordierite matrix has also been studied and of being subject to research [49]. The cordierite and mullite vol.% dependent electrical properties as well as dielectric properties versus porosity were examined systematically [49]. The author claimed that the composite with 70 wt.% cordierite fine powder and 30 wt.% medium particles exhibit the best electrical properties (dielectric constant ~7, dielectric loss=0.01-0.125). In the meantime, this composition shows excellent match TEC that of silicon as substrate material. Although addition of mullite does increase the dielectric constant from around 6 to 7 but the dielectric loss is decreased by 100%. The overall properties of cordierite-mullite composite are more favourable than that of neat cordierite.

As previously discussed, cordierite has been widely used in refractory materials such as kiln furniture, furnace support and some high temperature gas burner for instance, as well as advanced ceramics components for aerospace and so on. The most important properties of cordierite or cordierite-based ceramics composite lie with its excellent linear thermal expansion and thermal shock resistance. Thermal shock resistance (TSR) is widely studied among MAS ceramics such as Bauxite and Dolomite [71], cordierite/SiC composite [70, 72], mullite-cordierite composite, alumina–mullite–zirconia and alumina–mullite by slip casting [73] using water quench method. Yamuna et al [74] also tried IR heating to study thermal shock resistance in cordierite porous ceramics which showed advantages over water quench method. Recently, Tomba et al [75] employed the thermal shock induced stress in the cordierite ceramics disk and studied the effect of TSR by Finite element Analysis (FEM). In addition to this, the cordierite has been made to functional component such as honeycomb used as catalyst converter and the thermal shock resistance is studied and modeled based on the bulk materials by FEM, in which he found that the maximum thermal stress is less than the flexural strength of the material. The experiment supports

the FEM results that the honeycomb structure does not fail after flame heating up to the melting point [76].

In one word, cordierite-based ceramics is a very hot topic due to its unique properties. The most critical issue of cordierite-mullite-alumina composite research as mentioned in most literatures is the controlled formation of mineral phase with parameters such as sintering temperature, time, and starting materials. Banjuraizah et al [11] and Wu et al [77] showed that MgO excess distribution highly affects the cordierite formation efficiency and has effect on microstructural, thermal, mechanical and electrical properties of the ceramics sintered from non-stoichiometric/non-Standard precursor materials. However, the complete picture of roles of additives and binders in synthesis versus physical, thermal and mechanical properties is still an unaccomplished task. Thus, a good understanding, high efficiency sintering schedule from natural materials in terms of various properties is needed. In the following investigation, cordierite-mullite composite with other phases is synthesized and studied based on original powder of non-stoichiometric composition from commercial supplier. A more comprehensive work is beyond the scope of the present. However, the above-mentioned issues are expected to be addressed in near future.

1.5 Cordierite foam

Ceramics foams are cellular structure with struts made of bulk or bulk ceramics. It is found to be applied for instance in construction industry for thermal isolation, or as porous scaffolds for bone replacement made of bioactive ceramics. Ceramics foam is an important class of materials providing modest mechanical strength, shaping ability, hardness, durability, chemical inactivity, bio-compatibility. Apart from these, ceramics foam inherits the excellent thermal properties and are thought to be the most likely choice for filter and catalyst support with research interests [78]. One of the principal applications of ceramic foams in thermal engineering is lying with filter for high temperature fluid media due to its thermal stability (bulk TEC as low as 10^{-6}/K, Table 1.1), low thermal conductivity, low density and excellent thermal shock resistance. One of the noteworthy example is Zirconia foam has achieved thermal insulation properties equivalent to that of NASA space shuttle thermal protective tile but with much lower specific weight at 550 ^{o}C [79].

The foundry industry also has special interest in using ceramic foam in order to improve quality and productivity of metal casting which suffered from non-metallic impurity. The molten metal has typical temperature of 1000 ^{o}C and therefore the ceramic foam is required with

excellent mechanical-thermal properties [80]. The chemical stability is foreseen because molten metal contains very reactive species such as aluminium, titanium, hafnium and carbon. The thermal shock resistance is parameter to the component not to crack due to thermal expansion induced stress. Montanaro et al [79] has claimed that the thermal shock resistance is largely dependent on the foam cell size (increasing with increase of cell size) but weakly dependent on the density (also increasing with increase of density). However, the last but not the least t requirement to ensure good functional property is permittivity of the foam in terms of the cavity fraction and homogeneity of the foam which control the flow rate of the molten metal.

The structures of ceramics foam can be summarized in two types: 1) closed cell ceramics and 2) open-cell ceramics. The closed cell can be normally achieved by blowing air into molten materials or introducing foaming agent in the ceramics slurry. The closed cellular structure is formed and followed by calcinations at suitable temperature [2]. However closed cell ceramics foam can be used as thermal insulating or acoustic damping applications but hardly used as material for filtering or catalyst support which requires permittivity through the foam.

The ceramics fabrication is a difficult task due to the high temperatures required to sinter the green body into densified product. This is particularly troubling in case of ceramic foams since normal chemically induced foaming procedure will be burn out before the ceramics green body is sintered. Mutanaro et al [79] summarised the most conventional ceramics foam production approach in which two primary processing routes are applied. There are routes to fabricate Ceramics foams such as bubbles generation into a slurry or at green state with special thermal treatment, reaction sintering, control of sintering conditions in order to only achieve a partial densification, stacking of presintered granules or fibres, aerogel and sol-gel methods, pyrolysis of various organic additives and the method used in most studies also in this investigation, polymeric sponge/replicating method due to its simplification and low cost of chemical agents use [79, 81].

Open cell ceramic foams can made either by polymerizing (foaming) organic monomer in a ceramic slurry then dried and calcined [2]. However, the most used methods in producing ceramic foams is to coat the struts of a polymer preform with a ceramic slurry followed by drying and slowly (1 ^{o}C/min) burning out the polymer struts at intermediate temperature. Neto et al [81] studied the impregnation of cordierite foam using Polyurethane foam as replica and burned out polyurethane at 550 ^{o}C for 30 min followed by sintering at 1350 ^{o}C for 1 h. In this regard, polyurethane foam is most popular due to its non-toxic nature and versatility of microstructure control versus water content as foaming agent. The ceramics slurry usually contains particles

from 0.1~10 um with a suitable dispersant, and a binder/thickening agent to increase the bonding of the slurry on the surface of polymer strut [2]. The polymeric replica method has two variations, without, and with a thickening agent added to the slurry, the excess of which is then removed by blowing air or by squeezing after impregnation, thus obtaining a ceramic replica of the polymeric foam. The foams prepared former variation exhibit good air or fluid permittivity but lower mechanical strength, whilst the latter variation enables higher strength to be obtained due to high fraction of solid but decreases fluid permittivity.

An example of open cell with high porosity is shown in Fig. 1.6 illustrating the struts, cell and windows in a positive image of original polymer struts. The ceramic foams can be made with a wide range of properties and processing conditions via controlling the impregnation behaviour and rheological properties of the slurry. One of the most effective ways to control the microstructure and porosity is by squeezing the excessive slurries in different ratio to the original polymer struts.

However, the application of Ceramics foam is still limited because of their much lower mechanical strength in terms of Young's modulus and compression strength, thermal and dimensional stability compared to theoretical predictions with analytical model due to defect and porosity within the struts as demonstrated in Fig.1.6. The influence of experimental parameters on the mechanical properties will be revisited later in this thesis.

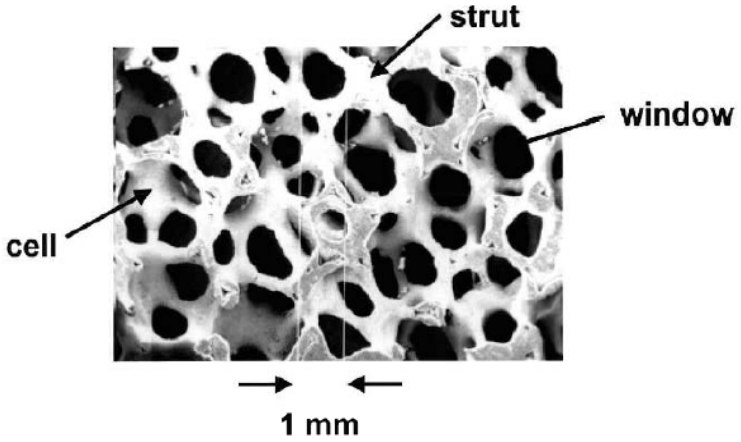

Fig. 1.6: typical open cell structure of Al_2O_3 with windows, strut and cell [2]

The structure illustrated in Fig. 1.6. shows many small pores distributed on the surface of the struts due to burning-out of polymer and shrinkage during sintering. Some researchers aimed at studying the preparation of ceramic suspensions with suitable rheological properties in order to improve the processing conditions of cordierite foams by the polymeric sponge method, avoid defects in the struts after sintering and enhance the mechanical properties with second

impregnation of slurry to fill the pores or defects [82].

The goal of the present work is to optimize the processing steps routes in order to obtain high specific modulus, high specific strength of cordierite foams for thermo-mechanical applications. The primary interest is to observe how the amount (wt.%) of dispersant and solid loading (vol.%) affect the rheological properties of the suspensions and the ability of polymeric foams. Susana et al [83] showed that precursor cordierite suspensions containing 45 vol.% solids dispersed with 0.8 wt.% Targon 1128 enabled good impregnating conditions. However this work did not considered the effects of either adding a thickening agent or of the slurry to struts weight ratio to control the microstructure homogeneity. A comprehensive study of rheological properties dependent effect on impregnation is beyond the timescale of this project at current stage, and the optimized parameters were selected from [83]. In this investigation, under the optimized rheological properties conditions of the slurry, the weight ratio of impregnating slurry to neat polymer struts is considered a critical parameter to control the structure of the foams obtained. The effects of drying conditions on the microstructure homogeneity of the foams were also studied using optical inspection. Microstructural characterization of as-produced ceramics foams was also performed by SEM (Scanning Electron Microscopy) and X-ray micro-tomography. Mechanical characterization tests included measurement of foam's apparent Young's modulus, Compression strength and Poisson ratio. Finally, modelling of mechanical properties is performed for cellular materials to simulate the mechanical behaviour of the experiment.

Chapter 2: Experimental techniques

2.1 Particle Size Analyzer

Coulter LS230 Laser spectrometer was used to determine the particle size distribution of the precursor powder dispersed in dilute aqueous suspension using the Fraunhofer optical model. The principle employed Coulter LS laser 230 lying with forward light scattering and Polarization intensity differential scattering (PIDS). This is discussed and compared to other particle size measurement principles by Taib et al [84]. The forward light scattering instrument consists of three main components: sensor, sample cell and particle counter. The particle is detected by scattered laser light whenever the particle is in the sample cell. The intensity alterations of laser light are collected by the detector. The particle size is proportional to the amplitude of the light intensity while the number of light pulses is used to determine the number fraction of the particles. The suspension is used with filtered tap water. The use of tap water is limited unless filtered due to bubble generation from degassing when the water temperature increases. According to [84] the bubble size could range between 100 to 500 μm and elimination by background measurement is not possible [85].

2.2 Scanning Electron Microscopy

Scanning Electron Microscope (SEM) is a type of electron microscopy technique that images the sample surface by scanning it with a high-energy beam of electrons. The electrons interact with the atoms that make up the sample producing signals that contain information about the sample's surface topography, composition and other properties such as electrical conductivity. The SEM is carried out on Hitachi SU-70 microscope installed at University of Aveiro.

The microscope is equipped with EDX (Energy Dispersion X-ray) module and PC terminal in order to analyse the elemental compositions and digitalise the image in real time. The types of signals produced by SEM including secondary electrons (SEs); back scattered electrons (BSEs), characteristic X-rays, light (cathodoluminescence), specimen current and transmitted electrons. These signals require specialized detectors that are not usually all present on a single machine. The signals result from interactions of the electron beam with atoms at or near the surface of the sample. In standard detection mode, secondary electron imaging or SEI is commonly used. The SEM can produce very high-resolution images of a sample surface, revealing details about 1 to 5 nm in dimension. Due to the way these images are created, SEM micrographs have a very large depth of field yielding a characteristic three-dimensional appearance useful for understanding the

surface structure of a sample. A wide range of magnifications is possible, from about 25 x (about equivalent to that of a powerful hand-lens) to about 250000x, about 250 times the magnification limit of the best light microscopes.

2.3 X-ray Powder diffraction

X-ray powder diffraction is used in this work as most important characterization to determined not only the phase identification during heat treatment but also quantitative phase fraction evaluation by whole pattern refinement analysis, also known as Rietveld refinement. X-way has been used in materials science with long history. It was discovered by physicist Wolfgang C. Roentgen in early twenties centruies, when Roentgen was working with a cathode ray tube similar to a fluorescent light bulb nowadays. He realized that he had discovered a previously unknown "invisible light," or radiation in a better sense, which was being emitted from the tube. He named the new ray X-ray, because in mathematics "X" is used to indicated the unknown property.

X-ray is a kind of electromagnetic wave and its wavelength could range from very hard region of 0.1 Å up to very soft 100 Å and this corresponds in terms of energy to the range of 100-0.1 keV. The energy of X-ray is described by its wavelength:

$$E = \frac{12.4}{\lambda} \text{ (keV)} \qquad (\lambda \text{ in Å}) \qquad (2.1)$$

The X-ray diffraction occurs based on the fact that X-ray will scatter at the periodical regular atomic lattice spacing. A real three-dimensional crystal is extremely large compared to the wavelength of incident X-ray and contains many sets of atomic planes. For diffraction, crystal must have the correct orientation with respect to the incoming beam, i.e. Bragg diffraction condition $2d\sin\theta=\lambda$, d is interplanar spacing, is the wavelength and θ determine the respective orientation between the crystal and incoming beam. Perfectly, infinite large crystal and perfectly collimated beam will allow the diffraction condition to be “exactly” satisfied. However, in reality, Strains, defects, and finite crystal size effects, as well as instrumental resolution due to collimation cause diffraction peaks to be broadened. In case of losing periodic arrangement of atoms in materials the diffraction pattern will show much more broadened feature which is characteristics to glass or liquid material. The diffraction patterns for perfect, imperfect and liquid/glass sample are seen in Fig. 2.1. For perfect crystals, $I(q)$, (I is the diffracted intensity and q is scattering vector) consist of δ functions (perfectly sharp scattering). For imperfect crystals, the peaks are broadened due to the factors of strains, crystallite size and instrument resolutions. For liquids and glasses, the diffraction intensity is a continuous, slowly varying function.

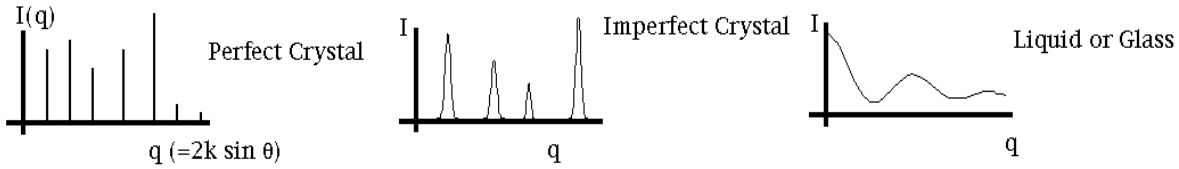

Fig. 2.1 diffraction pattern between perfect, real crystal and amorphous material (liquid or glass)

In actual study of ceramics material, one often find that the XRD patterns show superimposed feature of imperfect crystal pattern on the top of the amorphous pattern. This implies that the glass/liquid phase is formed and most of time unavoidable after sintering. This is due to the non-stoichiometric conditions that precursor oxides cannot fully react to form crystalline phase but transform into glassy phase. However quantification of the liquid/glass phase requires special sample preparation and data analysis skills which are not covered in this work.

X-ray diffraction has been also used for quantitative crystal structure study since introduction of Rietveld refinement in 1960's by H.M. Rietveld [86, 87]. Rietveld [87] showed that the profile refinement procedures by comparing to experiment was superior to any other methods involving either peak separation or use of total integrated intensity of groups of overlapping peaks. With Rietveld method, one of most preeminent drawback of powder diffraction method, i.e. loss of information as result of overlapped peaks has been tackled effectively. The original Rietveld method was designed to analyze the pattern from low resolution neutron powder diffraction. However the method has been extended to high resolution X-ray diffractometer with proper profile functions developed. The most important aspects of Rietveld method is the fitting could take into account parameters relating to the instrument or structure such as half width broadening without any sample's effect, 2θ zero offset, cell lattice parameters, temperature factors, atomic fractional coordinates, occupation numbers and so on in one analysis which speed up the efficiency of material analysis in a revolutionary way.

The Rietveld found its application particularly in quantitative phase (fraction) analysis (QPA) of mixed materials. There are primary two approaches in QPA called "traditional method" and "Rietveld method". Both methods are based on calculation of the peak reflection intensity. The reflection intensity from (*hkl*) of phase j is written as below:

$$I_j^{hkl} = I \frac{f_j}{V_j^2} L_{hkl} \left| F_{hkl,j} \right|^2 P_{hkl,j} A_j \quad (2.2)$$

Where, I: incident beam intensity, f_j: phase volume fraction, V_j: cell volume, $L_{hkl,j}$: Lorentzian polarization, $F_{hkl,j}$: structure factor, $P_{hkl,j}$: Texture factor, A_j: absorption factor. From (2.2) we see that the intensity of diffraction peak is directly proportional to the phase volume fraction, hence the weight fraction can be calculated provided each phase is known with its theoretical density can be calculated by X-ray diffraction analysis. The parameters in (2.2) are not necessarily known before QPA.

The traditional method to do quantitative phase analysis is based on internal reference by adding a known amount of additional phase to mixture and measure the peak intensity ratio. Therefore the amount of other phase can be calculated based on the ratio between their respective peak intensity to that of the known amount of internal reference as shown in (2.3).

$$\frac{I_j^{hkl}}{I_{\text{int}ernal}^{h'k'l'}} = K\frac{wt_j}{wt_{\text{int}enral}} \qquad (2.3)$$

However traditional method presents several unavoidable limits [88] such as the methodology to determine the peak intensity is often done to the height instead of peak integral; Only one or few peaks are used and this will produce error when preferred orientation is present; In case of peak overlapping the peak integral is difficult to be extracted as intensity. This principal error source urges the scientist to adopt alternative approach of QPA, namely Rietveld refinement.

In the Rietveld method, the peak is fitted with mathematical profile functions, thus differing from the internal reference method. Rietveld method uses a structure dependent approach including all crystal structure and sample microstructure information. However, Rietveld method also has limitations. When the structural information is not complete even for just one phase, the refinement work cannot proceed. The incorrect structural information will also affect the quantitative phase analysis in a significant way since the profile intensity is solely determined the crystal structural information. Recalling the usual intensity of Rietveld formula [88]:

$$I_i^{calc} = \sum_{n=1}^{Nphase}\frac{S_n}{V_n^2}\sum_k L_k\left|F_{k,n}\right|^2 S(2\theta_i - 2\theta_{k,n})P_{k,n}A + bkg_i \quad (2.4)$$

$S(2\theta_i\text{-}2\theta_{k,n})$ is peak broadening function which determines the shape of the peak, normally 4 types of shape functions are available in Bragg-Brentano geometry of diffractometer with θ-2θ coupled X-ray tube and detector, namely Gaussian, Cauchy, Voigt and Pseudo-Voigt as well as Pearson VII; $P_{k,n}$ is texture factor, A is absorption factor; which affects the height of the peaks; L_K is Lorentz-Polarization factor depending on instrument geometry, take off angle of monochromator, detector, beam size/sample volume and sample positioning (angular); $|\boldsymbol{F_{k,n}}|^2$ is

structure factor incorporated with temperature factor; bkg_i is the background function; V_n is the volume of unit cell [89]. Where S_n are now the scale factor for the phase j and comparing this to intensity formula for the *hkl* reflection in (2.2), the volume fraction or weight fraction of phase *j* can be written as:

$$f_j = \frac{S_j}{\sum_{n=1}^{N} S_i} \quad \text{and} \quad wt_j = \frac{S_j \rho_j}{\sum_{i=1}^{N} S_i \rho_i} \qquad (2.5)$$

N is the total number of phases in mixture, S_j is scale factor, ρ_i is density of phase, $S_i\rho_i$ is phase density of the phase. In (2.4) t the intensity of profile is calculated from the crystal structure and compared to the experimental data. The difference between them are minimized by adjusting the parameters such as crystal structure, sample size and instrument broadening as well as background and phase fraction. Therefore a quality of fit must be evaluated to the difference between the calculated and experiment, called "residual factor". The typical residual factor of Rietveld refinements are profile residual factor R_p, weighted residual factor "R_{wp}" and expected residual factor "R_{exp}" given by:

$$R_p = \frac{\sum_i |y_i(obs) - y_i(calc)|}{\sum_i y_i(obs)} \qquad (2.6), \quad R_{wp} = \left\{ \frac{\sum w_i \left(Y_i(obs) - Y_i(calc)\right)^2}{\sum w_i \left(Y_i(obs)\right)^2} \right\}^{1/2} \qquad (2.7)$$

$$R_{\exp} = \left[(N-P) \Big/ \sum_i w_i \left[y_i(obs)\right]^2 \right] \qquad (2.8)$$

Where Y_i(obs) is observed data point, Y_i(calc) is calculated data point from (2.4); The profile residual factor or weighted residual factor are used separately or simultaneously depending on software for instance GSAS uses R_{wp} and R_p while MAUD uses R_{exp} and R_p. N in (2.8) is total number of data points and P is total number of parameters taken into account in the refinement. And the ratio between R_{wp} and R_{exp} is called χ^2

$$\chi^2 = R_{wp} / R_{\exp} \qquad (2.9)$$

χ^2 is the goodness of the fit. Ideally it should be 1 however a practical guide is χ^2 usually required be less than 2 for simple and well crystalline phase. The χ^2 is often larger than 2 due to insufficient information of the model or poor quality of the data due to limited X-ray measurement time. Nevertheless, these days the Rietveld refinement is more and more popular used in challenging field such as dealing with complex mixture of phases (8-10) or semi-crystalline and amorphous phase. Therefore it is very often to see that R_p larger than 15 and χ^2 is larger than 2 which we still accept as a good refinement. The last but not the least is that the Rietveld refinement is also an extremely user experience related approach and the result could be

different or very different from one to another user for the same dataset. Someone even argued [89] that one or two years experience is needed in order to be able successfully use the Rietveld method independently.

The success to carry out a good QPA appears to be also dependent on choice of refinement strategy and software claimed by Connor et al [90]. Therefore we conducted a software benchmark to determine the most successful QPA strategy in our case. Currently several software are available either from commercial or free-of-charge sources. TOPAS is developed by Alan Coelho and commercialized by Bruker AXS. The other commercial one is used for trial in this investigation is "Siroquant" developed by Sietronics Australia. The advantage of using Siroquant is that the refinement benefit from using built-in mineral database containing structure of around 1800 most common minerals and compounds. However commercialization limits the usefulness of the software to us. In addition to this, free software such GSAS [91] developed by Los Alamos National Laboratory (USA), and MAUD [92] by University of Trento (Italy) are compared. The benchmark study is conducted for mixture of 3 oxides (V_2O_5, SnO_2 and ZnO) of good crystallinity with well-known structure. The weight fraction was pre-determined for comparison to those obtained from Rietveld method. In order to remove any ambiguities in choosing Rietveld Program due to data quality, the collection of data is perform over long time for very good intensity statistics. The typical recommended time Rietveld refinement is 2-5 h depending on the sample's phase complexity. Nevertheless we run the sample for 12 h. The result of QPA using GSAS and MAUD was shown in Table 2.1.

Table 2.1: QPA results from Rietveld Refinement

phases	weight(g)	wt.%	GSAS wt.%	MAUD wt.%
ZnO	3.292	25.528	29	***29.75***
SnO_2	8.1958	63.556	48	***61.29***
V_2O_5	1.4076	10.915	22	***8.96***

The result in Table 2.1 suggested MAUD gives a significant better agreement to experiment while GSAS showed the unsatisfactory agreement for SnO_2 and V_2O_5. Despite that both programs use the same algorithm shown in equation (2.5), the programs give different report on QPA is rather surprising.

The Rietveld refinement by GSAS is shown in Fig. 2.2 and by MAUD in Fig. 2.3 respectively. It was somehow surprising that the refinement by GSAS showed excellent quality of fitting in terms of difference curve and residual factor (see Fig. 2.2). However the QPA result in

Table 2.1 does not reflect a good agreement to experiment. This alerts us that a choice of program and strategy should be considered unless the cause of disagreement could be identified and tackled.

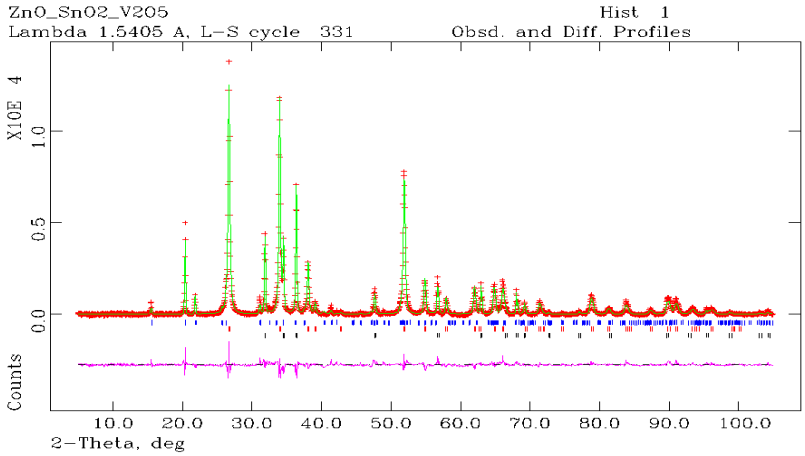

Fig. 2.2: refinement plot of ZnO-SnO_2-V_2O_5(GSAS): R_{wp}=8.33%, Rp=6.25%

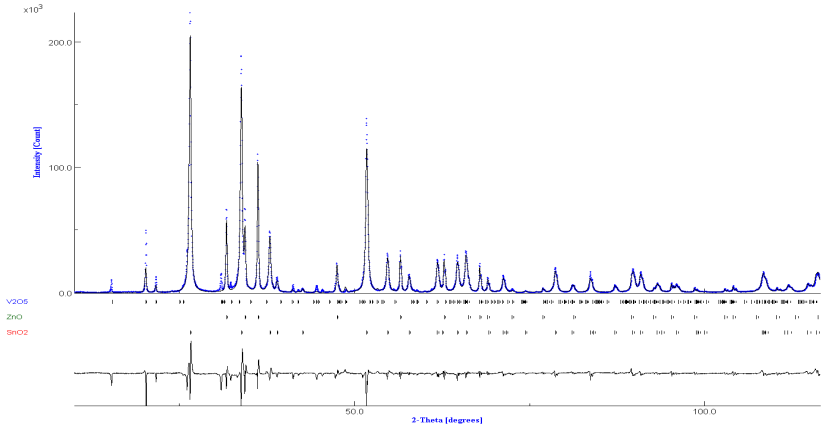

Fig. 2.3: QPA result of 12 h scan by Rietveld method (MAUD), R_{wp} ~17%

On the other hand, MAUD showed relatively worse quality of Rietveld fit, R_w~17% in Fig. 2.3. However, the QPA result is very close to experimental result. The deterioration of quality is supposed to relate to the incorrect model of background subtraction. However, a comparative study between GSAS, MAUD for mixture of ZnO, SnO_2 and V_2O_5 suggested that the MAUD should be used in QPA practice.

Finally, being a powerful investigation tool, X-ray diffraction also has disadvantage due to decreasing scattering power as function of diffraction 2θ. This gives problem in determination of small structural details within the higher angle (small d-spacing) peak region.

2.4 Mechanical properties Characterization

Mechanical properties are the most important to ceramics materials at ambient or non-ambient environment. The typical measurements include characterization of compressive and flexural properties. However, for ceramics samples, another measurement technique based on sonic vibration is also introduced due to difficulty in performing compression test to obtain Young's modulus. All measurements were conduced at room temperature in the study. However, the high temperature behaviour of ceramics modulus is an interesting subject to be determined with special setup in sonic vibration technique for advanced refractory application such as aerospace and rocket industry.

2.4.1 Compression

Young's modulus and Compression strength study were carried out for the cellular structure of ceramics by compression test. The specimen preparation does not follow dimension requirement of ASTM standard due to sample machinability hardship caused by ceramics brittleness. However, the equation (2.10) was used to calculate the modulus from ASTM standard.

$$E = \frac{WH}{AD} \qquad (2.10)$$

Where W is the load (N), and H is the initial height in m of the sample, A is the initial area (in m^2) of the sample and D is the intercept distance (in m) between point T and O on deformation axis as shown in Fig. 2.4. The point S is chosen arbitrarily [93]. The stress-deformation curves usually required to be measured 6 times prepared from the same batch [93]. However, this could not be easily achieved since the production ceramic foams with homogeneous microstructure are a difficult and time-consuming (2 weeks) process. Alternative strategy must be adopted such as one or two samples from the same batch are used to measure the Compression strength. The Compression strength is determined by finding the first maximum load divided by the cross sectional area of the cube in each measurement and mean value and standard deviation are calculated.

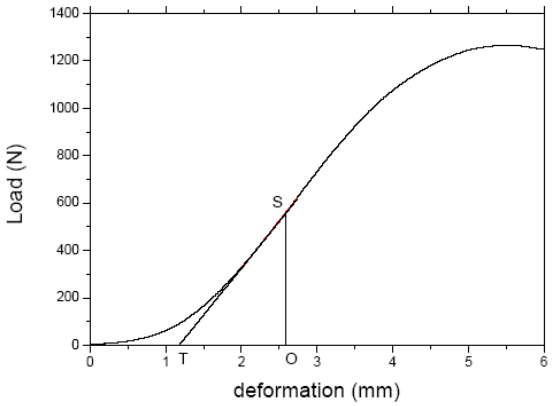

Fig. 2.4: Schematic illustration of calculating elastic modulus [93]

In general, a typical compressive behaviour of stress-strain curve of polymer foam with non-brittle struts material (unlike ceramics) is presented in Fig. 2.5; it shows that there are three stages in compression mode mechanical behaviour.

i. *Linear elastic region*, where stress is linearly proportional to strain;

ii. *Plateau region,* characterized by a maximum compressive stress at start and stress-independent deformation with increasing strain; this corresponds to a hardening effect;

iii. *Densification region,* final stage where the material is pressed and densified, hence exhibiting bulk behaviour.

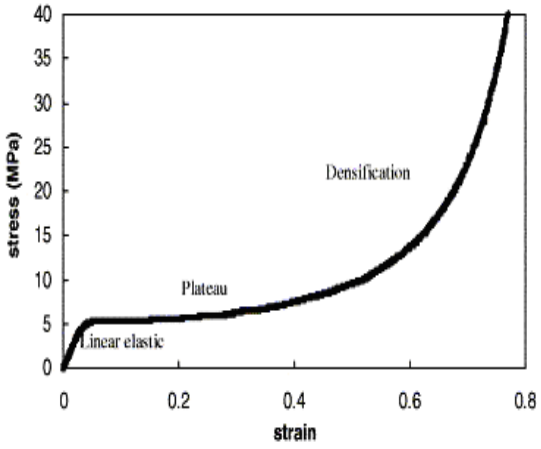

Fig. 2.5: Compression stress-strain curve of polymer foam [94]

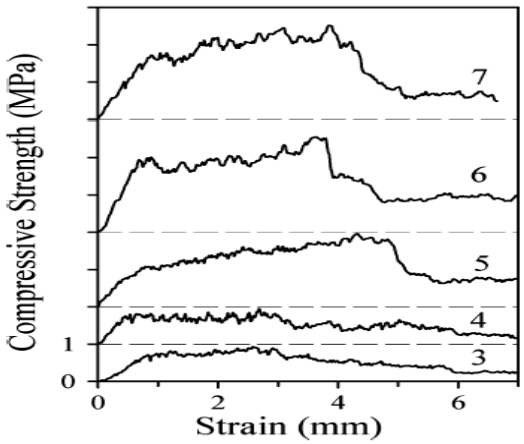

Fig.2.6: Compression stress-strain curve of ceramics foam [95]

From the slope of linear elastic region, the Young's modulus can be calculated and the intersection point between elastic region and plateau region gives the maximum compressive

strength. Polymer Foams have a high energy absorption capacity represented by the area below the curve in Fig. 2.5. This type of behaviour is complicated in case of ceramic foams as seen in Fig. 2.6; samples are numbered from 3-7 with different microstructures. Since the strut is made of materials with brittle nature and they cannot undergo large deformation. For instance, the high level of brittleness of ceramics struts of ceramic foam causes ceramics struts failure and breaks. Therefore, the stress-strain curve shows a zigzag behaviour until the cellular structure breaks down completely due to major event of crack propagation and hence stress drop to minimal as seen in Fig. 2.6. The Compression strength is defined at start of plateau of stress. However, the Young's modulus from compression test is dubious and often found to be significantly lower (by 2 or 3 orders of magnitude) than values given by sonic vibration measurements.

2.4.2 Flexural strength

Flexural strength is also known as bending strength or fracture strength which measures the trend or capability how much strength materials can resist on bending until fracture. It is a very important engineering property in structural and component design. The unit used for flexural strength is MPa in case of the force is in N and the area is in mm^2. The most typical measurement method for flexural strength is based on "three points" bending which is illustrated in Fig. 2.7.

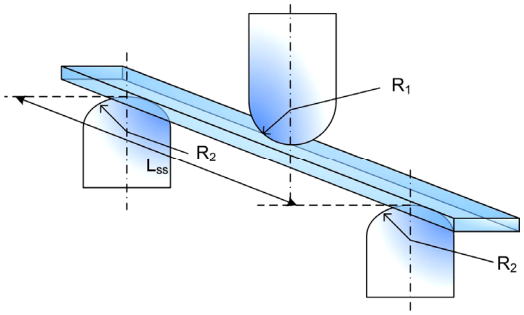

Fig. 2.7: illustration of three-point bending test of flexural strength [96]

The determination of flexural strength is carried out in two cases for sample with rectangular or circular cross section. For a rectangular bar, the calculation of the flexural strength is given by:

$$\sigma_f = \frac{3FL}{2bd^2} \quad \text{(for a circular cross section)}$$
$$\sigma_f = \frac{PL}{\pi R^3} \quad \text{(for a circular cross section)} \qquad (2.11)$$

Where, F is the load (N) at the mid-point of the sample, and $L=L_{ss}$ as seen in Fig. 2.7 is the length of the lower support span, b is width and d is thickness of the sample in mm; in case of circular cross section, R is the radius. The measurement method could also refer to procedures given by ATSM standard [97]. R_1, R_2 in Fig. 2.7 is not relevant in our investigation since the contact region between the sample and stressed point is not spherical but parallel surface.

The flexural strength represents the maximum stress experienced in the material at its moment of rupture. In practical application, the flexural strength is often equivalized to the Von Mises stress [98] in modeling. This is especially useful in cellular structure since the structure of cellular framework is random and the stress generated due to strain is not uniform. Somewhere in the cellular structure the stress exceeds the flexural strength earlier than other part. This implies that part will fracture earlier and the crack generated is likely to propagate to cause global mechanical failure. We will see the comparison between the experiment and modeling of the fracture of ceramics cellular structure in this work later on.

2.4.3 Impulse Excitation Measurement

The impulse excitation technique is based on the principle that solid will vibrate under external stimuli at its intrinsic frequency and the air around the solid will be excited at the same frequency and hence the sound wave is generated. The generated sound signal will be measured by the acoustic transducer and converted into electrical signal of waveform. The waveform is then analyzed by Fourier transform (FT) to obtain the frequency components of the waveform. The fundamental frequency of the waveform corresponds to the fundamental frequency of the solid harmonic mode.

The fundamental frequency of impulse excitation is connected to the solid materials properties such as Young's modulus (E) and shear modulus (G). This technique is often used in field of non-destructive test or non-ambient environment where conventional compression test is not possible. In case of ceramics or porous materials, this technique is advantageous since the ceramics often exhibit a very high modulus and the required force to compress the sample is huge and exceeds the machine's maximum force capability. In addition to this, the compression test requires the sample has a high level of flat surface in order to carry the load uniformly otherwise the non-uniformity of ceramics sample will produce cracks and propagate rapidly. Ceramics materials have very brittle nature and extremely small elastic deformation region; therefore, the specimen without perfect flat surface could collapse completely before starting elastic compression. On the other hand, ceramics are very difficult to machine in terms of dimension due to its brittleness and hardness.

The typical setup for impulse excitation measurement of Young's modulus and shear modulus is shown in Fig. 2.8. Note that the location of microphone and place of tapping with impulse is different in each case. The specimen must be placed on two nodes with distance of 0.224 L (L= specimen length) to each end in Fig. 2.8(a) [99]. The specimen is required to be long and thin in order to give the best result of measurement as large aspect ratio will simplify the calculation of geometry correction factor.

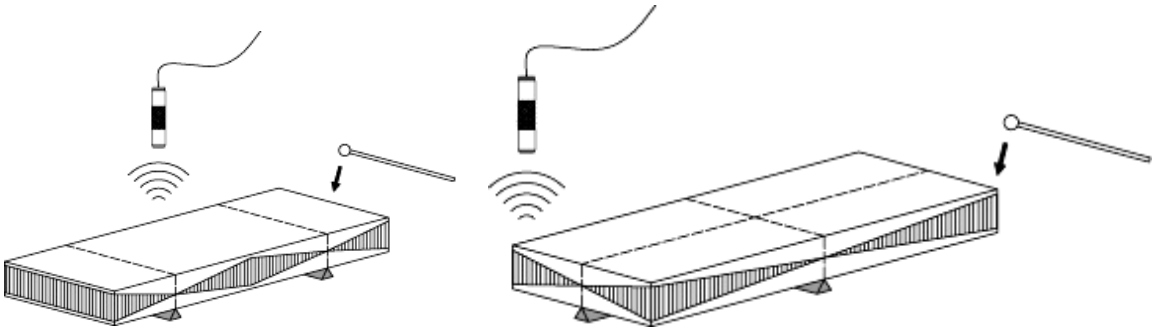

(a) (b)

Fig. 2.8: (a) setup for Young's modulus; (b) setup for shear modulus [99].

The measured waveform signal of damping sine wave is shown as in Fig. 2.9 used to calculate the frequency of flexural/torsion mode with Fourier Transform (FT) and the frequency is then used to calculate the Young's and shear modulus according to ASTM standard [99]. Usually the damping sine waveform signal is a composition of several single frequencies damping sine wave. The mathematical expression to the waveform from IE measurement $x(t)=Aexp(-\delta t)sin(\omega t+\phi)$: Where, A is pre-component, δ describes the damping decrease of the sound in the solid and f in terms of ω is the natural frequency. Ideally only single frequency after FT shows up but it is rarely seen. Other vibrations from higher harmonic mode or ambient support or experiment environment are also possible to be recorded and show up in the frequency domain after FT. One should use the most appropriate frequency for modulus calculation while others give rise to either too high or too low modulus results.

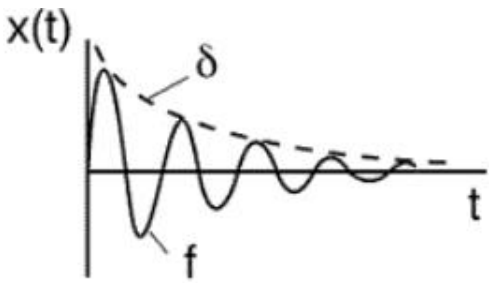

Fig. 2.9: the general shape of waveform measured in IE experiment

The calculation of Young's modulus is based on specimen's weight and dimensions:

$$E = 0.9465 \cdot \left(\frac{m f_f^2}{W} \right) \left(\frac{L^3}{t^3} \right) T \quad (2.12)$$

Where E=Young's modulus, f_f=Flexural frequency, m=mass, L=length, W=width, t=thickness and T is correction coefficient which is defined for two cases when L/t>>20 and L/t<20 in ATSM standard [99]. The IE technique is also applied to measure the shear modulus as shown in Fig. 2.8 (b). The shear modulus is determined by the specimen's dimension and weight as specified in ASTM standard [99] in equation:

$$G = \frac{4Lmf_f^2}{Wt} \left[\frac{B}{(1+A)} \right] \quad (2.13)$$

Where G=shear modulus, f_t=torsion frequency, m=mass, L=length, t=Thickness, A, B=correction coefficients. The correction coefficient A, B is dependent on the sample geometry which is defined in ASTM [99].

The Poisson ratio of ceramic foam is a reflection of the isotropy of cellular structure. The theoretical evaluation of isotropic material gives rise to ν=0.3. Poisson ratio can be calculated from measuring Young's modulus and shear modulus. However the Poisson ratio calculation is limited to isotropic materials and the Poisson ratio of anisotropic materials can not be determined using the impulse excitation technique. The relationship between E and G to calculate Poisson ratio is given:

$$\nu = \frac{E}{2G} - 1 \quad (2.14)$$

The Poisson ratio for ceramics material can also be calculated if this is not known prior to the experiment of shear modulus. Phani et al [100] gives an estimate for isotropic ceramics porous structure that the ratio E/G=0.391. Therefore, Poisson ratio can be calculated just by knowing E while shear modulus is difficult to be measured. In one word, the IE technique is particularly useful to mechanically characterize brittle ceramic foams or porous structure. The damping factor measured in the IE experiment is a reflection of defects existing in the dense material which cannot be seen. Therefore IE technique is also a qualitative mean to evaluate of the specimen porosity as defect when sound is propagated and damped in the materials.

2.5 Thermal properties measurement

DTA/TGA equipment was also used to characterise the phase transition/or chemical reaction

by locating the exothermic or endothermic peak while TGA is used to characterise the weight loss during temperature rising. The DTA is used to study the heat flow Changes in the sample, either exothermic or endothermic. The heat input into the sample can be detected relative to the inert reference. Therefore, a DTA curve is used to study materials transition that have occurred during heating/cooling, such as glass transitions, crystallization, melting and sublimation. The area under a DTA peak is the enthalpy change and is not affected by the heat capacity of the sample. The DTA use Al_2O_3 as inert sample on one side of the system on the other hand, the materials was placed with a voltmeter to record the power supplied. As temperature rises, the heat input into the inert sample will be equalized to that into the materials however when phase transition takes place the heat into the sample will be deflected in the voltmeter as the power is used as latent heat while the same amount of power is recorded for inert sample Al_2O_3. Therefore, the power under the peak area is considered to be enthalpy of the transition and the location of the exothermic or endothermic peak are considered to be the phase transition with maximum rate.

The thermal shock resistance was also carried out according to ASTM standard C1525-04 [101]. The retained flexural strength of ceramics after water quenching the specimens from elevated temperature was measured. This standard gives critical temperature at which the flexural strength is decreased by at least 30%. Although the standard does not determine the thermal stress generated as consequence of temperature rising, it can be calculated as proposed in [102]:

$$\sigma_{thermal} = \frac{\Psi E \alpha \Delta T}{1-\nu} \quad (2.15)$$

ΔT is the temperature difference between the sample and quenching medium prior to the quenching, α is linear thermal expansion coefficient while ν is Poisson ratio and ψ is the stress reduction factor. For very rapid heat transfer ψ is defined as 1 [15]. Therefore re-arranging (2.15) by replacing thermal stress with flexural strength of ceramics body σ_f, one could derive the analytical expression of thermal shock resistance as below:

$$\Delta T_C = \frac{\sigma_f (1-\nu)}{E\alpha} \quad (2.16)$$

(2.16) is an useful equation by which one can estimate the thermal shock resistance via measure of linear thermal expansion coefficient, Young's modulus, and flexural strength as well as Poisson ratio which are easily done. However, one should be also aware of that (2.16) does not take into account of thermal conductivity which has effect on ψ in (2.15), hence the (2.16) is normally regarded as estimate of performance and used for comparison purposes [15]. The (2.16) corresponds to the minimum temperature difference required to generate thermal stress that is enough to nucleate macro flaws within the ceramics body that cause significant mechanical strength degradation. However in practical, the thermal shock resistance is often much higher

than the calculated due to the porosity could dissipate the crack energy and hence stop the crack propagation.

2.6 Computed X-ray Tomography

X-ray tomography is an imaging technique used to study the internal microstructure of a material. It provides non-destructive test that reveals the actual 3D structure of the sample. In SEM experiment one could only obtain 2D information or surface after material fracture. In contrast to this, X-ray tomography allows one to study the actual 3D shape of the microstructural objects without any compromising to integrity. This provides an overwhelming advantage to materials scientist to investigate the composite material in which the embedded objects cannot be readily examined [103]. The theory behind this technique is based on X-ray radiography when an X-ray radiation is illuminated on a sample the transmitted beam is recorded which is dependent on its material absorption coefficient, such as density, the atomic number and the energy (when the beam is monochromatic) [104]. A large number of radiographs shown in Fig. 2.10(a) by rotating the sample in the X-ray beam between 0^{o} and 180^{o} [103, 104] are obtained. Instrument software is applied to the resulting radiograph images to produce 2D slice image in Fig. 2.10(b) and 3D volumetric structural information is accessible by adding up the 2D slice image as shown in Fig. 2.10(c) [103]. Provided the thickness of slice is small enough to ensure continuity of the structure, for instance, an example of 3D structure of cellular materials after 3D reconstruction as shown in Fig. 2.11.

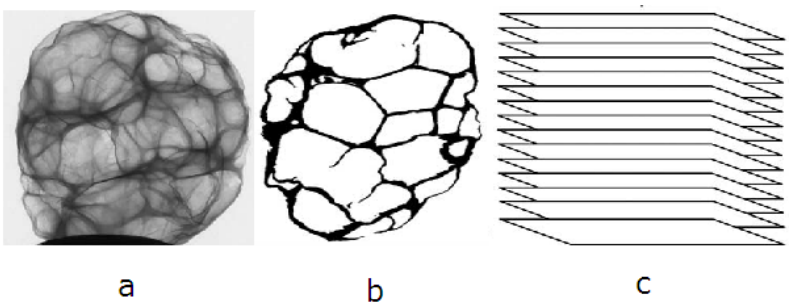

Fig. 2.10: *Reconstruction (a) radiography image (b) 2D slice image (c) set of 2D slices obtain from scanning to be used in the reconstruction of 3D actual structure* [103]

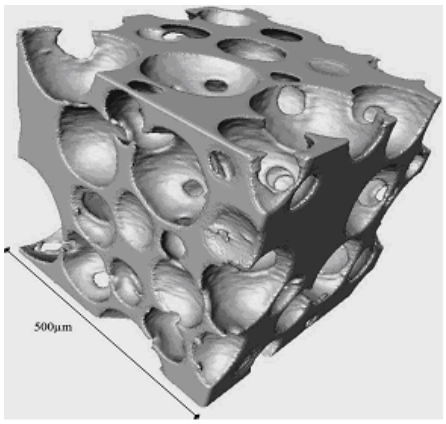

Fig. 2.11: *3D Tomography image of polymer foam [94]*

The prerequisite for carrying out a good quantitative volumetric study is a high X-ray scattering contrast between the interested objects and background. The results reveal that X-ray tomography is very suitable to study cellular materials due to X-ray scattering contrast from the air and the strut materials is usually good enough to be processed by imaging analysis.

2.7 3D structure model and Finite Element Analysis

Very recently, numerical techniques such as Finite Element Analysis (FEA) have been developed to simulate cellular materials' mechanical properties to Polyurethane foam [94, 105], Polyvinylchloride Foams [106] and Nickel metallic foam [107]. This was particularly successful using computerized X-ray tomography to render actual 3D structure of foam for FEA calculation. However, X-ray tomography method only covers small fraction of the foam which may introduce inaccuracy when the foam's microstructure is not homogeneous. In addition, the high cost of FEA method that requires tremendous computing capacity may limit its application. It is noteworthy that state-of-the-art X-ray tomography technique is able to provide resolution as good as 1 μm, thus leaving behind the study of smaller objects such as MWNTs (10-30 nm in diameter) embedded in composite material. Nevertheless, Tomography aided FEA method becomes more and more popular in composite material design to study mechanical properties of heterogeneous materials or components with non-trivial geometry, which can not be covered by analytical approach. We adopted this technique in study of cellular structure and mechanical property of the 3D structure by FEA. It proves the effectiveness in using non-destructive testing method to study the interior structure of ceramic foams, which, otherwise was impossible to study by any other means. The study starts with Tomography Image Processing using "AMIRA" or "AVIZO" which is commercially available to carry out the structure visualization. The structure was then converted into model by ImageJ which is compatible with the finite element program

"Abaqus/CAE" for simulation of mechanical properties.

The reconstruction of 3D structure is preceded with steps below:

1. Input the original slices image stack into AMIRA
2. Displaying the bounding box to check the size of volume to process is suitable
3. Applying Noise Reduction Filtering to smoothen the background
4. material labelling which distinguish the ceramics strut and air in slice image
5. generate 3D structure of cellular structure
6. Generate tetrahedron elements for grid file (*.inp) into FEM program

Once obtained the grid file, the file is used as input model into Abaqus/CAE for calculation. Abaqus/CAE is software developed by SIMULA, USA for finite element analysis. The structure produced in AMIRA is applied with boundary conditions that no surface will move except in Z-axis direction there is an applied displacement. The strut properties of ceramics foam has to be specified also before calculation. The Young's modulus and the Poisson ration are given from experiment of the bulk ceramics. The displacement is applied uniformly downward to produce compressive deformation and the force reacted as result of this displacement for this material is calculated. The reaction force component in Z-axis is used to calculate the stress on the compressed surface and hence the modulus. It is also noticed that the Von Mises stress is calculated as output file and the stress distribution across the ceramics body will be shown in colour contour map. This is useful since by comparing the calculated Von mises stress to the flexural strength from experiment we can determine when and where the ceramics will fracture and fail. The elastic properties can also be estimated from this simulation avoiding the machining hardship to ceramic foams introduced previously. The elastic properties of the ceramics foam by taking into account of hollow structure inside struts are compared to the modulus from Impulse Excitation measurement to check the validity of the model and effectiveness of FEM analysis.

Chapter 3: Experimental preparation

3.1 Ceramic Suspension

The ceramics suspension also known as slurry is made by aqueous dispersion method. The precursor powder was supplied by Rauschert. The powder is a mixture of natural minerals containing non-stoichiometric composition of Corundum (α-Al_2O_3), Talc (triclinic), α-Quartz (SiO_2), K-feldspar, Mullite ($Al_6Si_2O_{13}$), Kaolinite ($Al_2Si_2O_5(OH)_4$), trace amount of Calcite, Cristobalite, and glassy phase. The powder density measured by Pyconometry is around 3.0g/cm^3 at 20^{o}C. The suspension was made with a set of optimized parameters from previous work of Susana et al [83]. Hence, 45 vol% solid loading was applied by 0.8 wt.% Targon 1128 dispersant. Each batch of slurry contains 189.1 g of powder, 89.2 g of water and 1.5 g of Targon 1128 that were mixed. The Targon 1128 was firstly added into the distilled water and then the precursor powder was slowly added into the mixture under mechanical stirring in a glass beaker of 200 ml. After mechanical stirring of 5 mins, the slurry was transferred into a plastic bottle filled with alumina balls of different sizes and ball milled. The as-prepared suspension contains a lot of particle agglomerates in presence of dispersing agent. Therefore the suspension was subject to ball milling at low speed only to destroy the particle agglomeration. The particle size will not be reduced versus time with modest force upon particle analysis by Laser diffraction method. The schematic illustration of preparation of suspension is shown in Fig. 3.1.

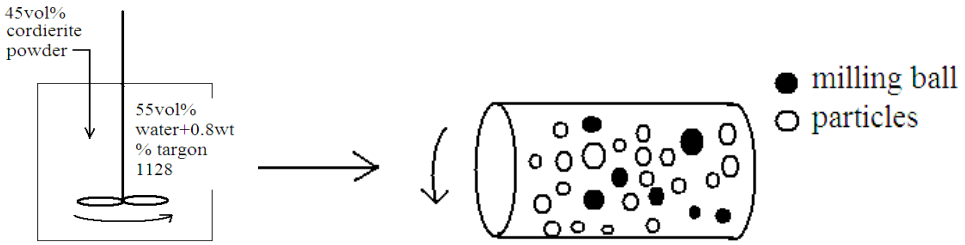

Fig. 3.1: Cordierite suspension preparation and ball milling;

3.2 Slip casting and dry pressing

The dense ceramic are prepared in two ways namely, slip casting and dry pressing. The slip casting is based on the ceramics suspension prepared in previous section that is cast onto plaster mould until the cast body becomes completed dried. Then the cast body is transferred to oven at 80^{o}C for 24 h until it reaches constant mass. However the deformation of slip cast sample is

serious due particle size segregation and a density gradient derived from a decreasing driving force as cake thickness increases. The slip cast sample must be grounded to achieve parallelism of surface for flexural strength measurement. The alternative route to prepare green body for flexural strength measure is using method introduced by A. Goel et al [108] that use 5 vol.% PVA solution corresponding to 2.5 wt.% PVA+97.5 wt.% powder). In our case, the rectangular bars of green state were prepared with PVA (polyvinyl alcohol) solution prepared by the following: 1.7 wt.% PVA solution of 200 ml was magnetically stirred in warm water (65 ^{o}C) for 7h until the PVA is completed dissolved as the solution becomes transparent. The PVA solution was then sprayed onto the as-supplied granulated powder of 400 g in a rotary mixer for uniform coating of PVA. The mixture of PVA solution and powder was seen as paste-like material due to excessive hydration with big particle agglomeration. Therefore the paste was grounded to smaller particles and filtered with 500 μm sieve to achieve uniform particle distribution. The powder was then dried in air for 24 h and the initial hydration of aforementioned filtered powder must be measured by drying a batch of mass 3.2 g in an oven at 90 ^{o}C until it reaches constant mass. The hydration was found around 15 wt. %. The complete time dependent drying behaviour of the aforementioned powder is presented in Fig. 3.2.

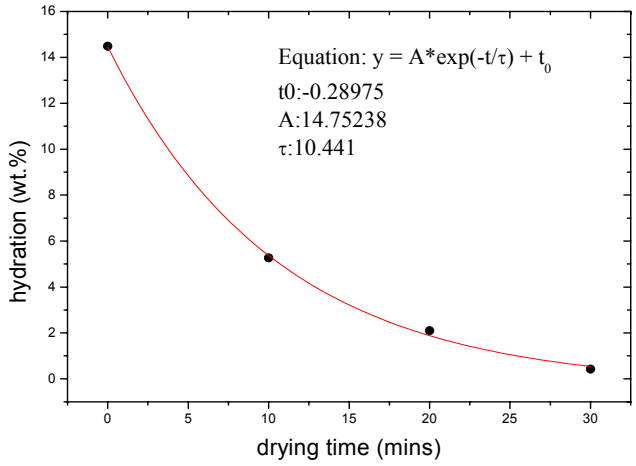

Fig. 3.2: drying behaviour of PVA solution coated precursor powder

The drying behaviour in Fig. 3.2 is an exponential decay function: $y=A*\exp(t/\tau)+t_0$ where, y is the hydration at time t from t=0 with pre-coefficient and decay constant of τ. Therefore the hydration could be controlled precisely by elapse of drying time with those parameters determined in Fig. 3.2. However, after applying the PVA solution, the pressed sample is still not pressed well after drying in air for 1 day due to unsuitable humidity level as seen in Fig. 3.3. Therefore, the drying-pressing strategy needs to be re-evaluated in our investigation to find the

optimal conditions of dry pressing.

Fig 3.3: dry-pressed bar of 1.7wt.% PVA binder with 15wt.% hydration

Fig. 3.4 show dry pressing behaviour with 2 hydration 0 and 2.5 wt. % at the same PVA binder wt. %. The hydration was achieved by following the time dependent drying curve in Fig. 3.2. It is clearly illustrated that a decrease of the hydration to 2.5 wt. % in powder enabled a very successful pressing with perfect shape as seen in Fig. 3.4. However the bar has to be completely dried before sintering. Therefore, further decrease of hydration to 0 wt. % was test for shaping capability. The bars however, showed small cracks at the edge or corner during handling or transporting in Fig. 3.4. This proved that completely dried powder with PVA binder is not preferential for dry-pressing. A suitable level of hydration is beneficiary to make the sample crack-resistant during handling and pre-sintering. With experimental evidences shown above, we conclude that at most 2.5 wt. % hydrated powder is suitable for dry pressing however we expect to see a more optimized hydration between 2.5wt. % and 0 wt. % upon further experiments.

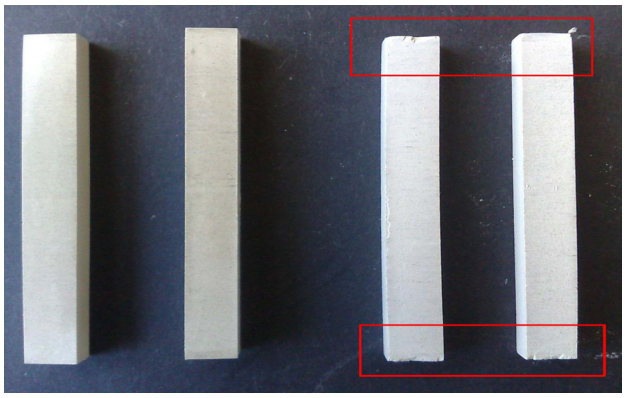

Fig. 3.4: dry-pressed bar of 1.7wt. % PVA binder with 2.5wt. % hydration (left two); with 0wt. % hydration (right two). The cracks are highlighted with red rectangles

3.3 Suspension impregnation of polymer replica

Polymer replica method is used to make ceramics foam. The polymer was supplied with three microstructure specification, namely 8 PPI, 22 PPI, and 30 PPI (PPI, Pore Per Inch). A visual inspection of the cell microstructure reveals that the 8 PPI and 22 PPI foam has an open cell structure. However 30 PPI polymer foam do not show significant open cell structure.

The manufacturing of ceramics foams is based on polymeric replica impregnated with ceramics slurry and involves multiple stages: The first step is to prepared ceramics slurry that has been introduced previously. The step by step procedures of making of ceramics foams at specific wt. % dispersant in this investigation and characterization are also presented in Fig. 3.5.

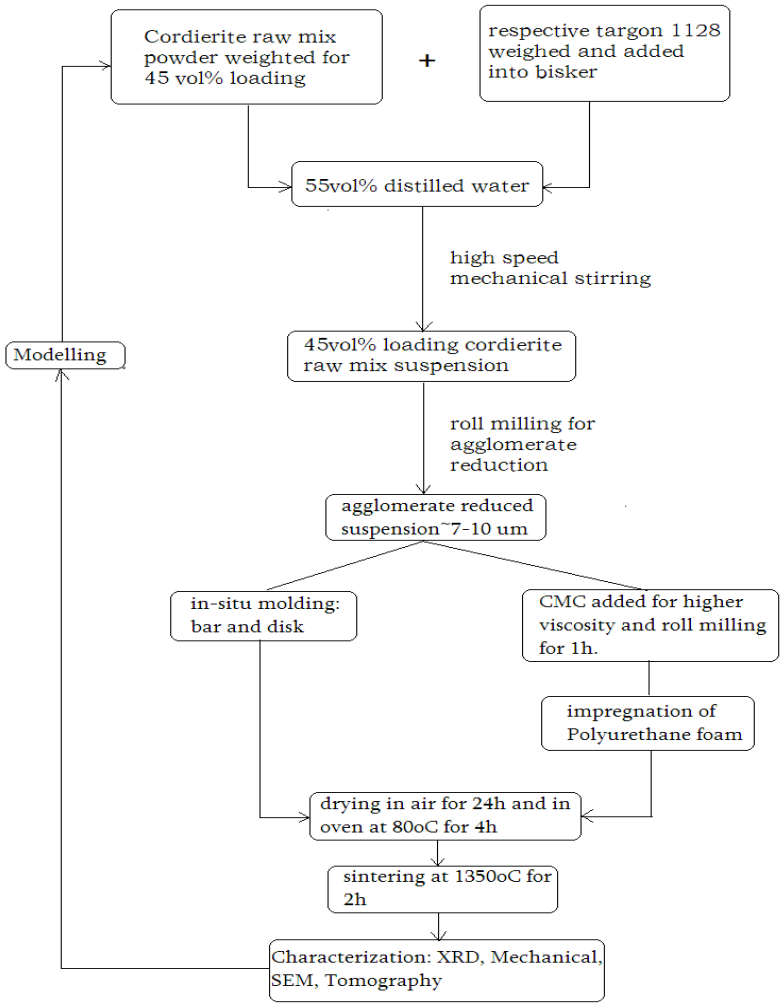

Fig. 3.5: step by step procedures and plan in making ceramics foam.

The 8 PPI, 22 PPI and 30 PPI polymer replicas were cut into cube or rectangular shapes for impregnation. Cubic or rectangular shape is suitable to perform compression test or Impulse

Excitation method. The polymer replica was impregnated with ceramic suspension with and without thickening agent to explore the best strategy to obtain homogeneous impregnation. The procedures of impregnation are following: i) pour the suspension onto the polymer replica; hand pressing should be applied to allow the suspension to flow into the interior structure of the polymer replica. However, excess suspension usually stay on the surface of polymer struts and, therefore, the coated polymer replica should be squeezed after impregnation to remove excessive slurry. The amount of suspension coating the polymer replica can be characterized by the weight ratio of polymer struts (PS) + impregnating suspension (PS+IS) to polymer struts (PS).

The polymer replica is referred to the polymer foam without impregnation. In our investigation, 300 mL of 45 vol% solid loading ceramic slurry was require to impregnate 200-300 cm^3 polymer replicas with dispersant and thickening agents. The weight ratio (PS+IS)/PS was recorded from the time of impregnation until the slurry impregnated foam was completely dried. This is proved to be crucial to obtain a good dispersion of cordierite slurry which has high viscosity. The slurry was impregnated at room temperature and placed in air for 24 h in order to remove the water gently to avoid crack on the surface. Then the green ceramic foams were subject to drying in oven at 90 ^oC for 12 h to completely dry the foam until constant mass before sintering.

There are two main parameters can be varied in dispersion preparation, such as the solid loading (vol. %) and the amount of dispersant (wt. %). The combination of these two parameters will be seen as the most influential factors to the mechanical properties. However, we only use the optimized parameters according to Susana et al [83] with 45 vol.% loading and 0.8 wt.% Targon 1128. In our investigation we examined the effect of rheological property on impregnation behaviour by adding 0.2 and 0.5 wt. % thickening agent “CMC” (Carboxymethyl Cellulose) to increase the viscosity of the suspension. The viscosity was seen very influential in the impregnation for instance, the suspension without CMC show high flow ability that hardly any suspension will rest on the polymer struts after impregnation and the suspension settled to the bottom. On the other hand, highly viscous suspension was obtained by adding 0.5 wt.% CMC after 1 h mixing in ball milling showed insufficient flow character for a proper impregnation of smaller polymeric structures, resulting in highly inhomogeneous distribution of the suspension upon squeezing. This has important negative effects to the homogeneity hence the applicability of the as-produced foams. Based on this fact, 0.2 wt.% CMC added suspension was chosen as optimal condition to prepare the ceramic suspensions with a good ability to coat the fine structured polymeric replicas, while suspensions containing 0.5 wt.% CMC were selected for impregnating larger pore size (8 PPI) replicas.

The drying behaviour was recorded in order to determine the optimal weight fraction of suspension to be impregnated with polymer replica. This is due to the fact that removal of excessive suspension after impregnation was manual based and it is not easy to control the suspension fraction by hand squeezing unless the weight is recorded. It turns out to be the most effective parameter in terms of controlling the homogeneity of the foam from impregnation.

3.4 Sintering and Post-treatment

Sintering was carried out for bulk ceramics and ceramics-coated polymer foam. The sintering temperature was conducted at 1250 ^{o}C and 1350 ^{o}C. This choice is based on XRD study shown later on that cordierite phase only form within temperature window above 1250^{o}C. In addition, 1350 ^{o}C is the maximum temperature of the furnace available for sintering ceramic coated polymer replica. Sintering at higher temperature such as 1425 ^{o}C and 1500 ^{o}C is possible for bulk ceramics. The bulk ceramics sintered at 1500 ^{o}C showed significant fractures or defects. This was attributed to formation of liquid phase above 1460 ^{o}C due to cordierite melting and hence the gas bubble occurred appeared in liquid phase. These results showed good properties were unlikely to be obtaining for sintering temperatures higher than 1350 ^{o}C. Stepwise sintering experiments were also carried out at 950 ºC and 1050 ^{o}C to study the phase transformation of original precursor powder along the temperature profile. The sintering schedule for slip cast bulk ceramics sample is illustrated in Fig. 3.6, consisting of a ramp of 5 ºC/min up to 1350 ^{o}C, a holding time of 2 h, followed by natural cooling.

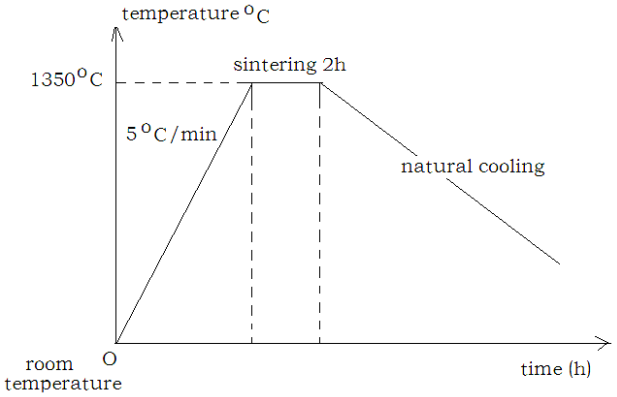

Fig. 3.6: Sintering schedule of bulk ceramics

The coated polymer replicas were sintered following a different schedule due to the slow burning out of the polymer struts. Susana [83] described the burning out of polymer struts should

be carried out gradually with small temperature ramp rate in order to minimise the crack of coated ceramics due to different thermal expansion properties of polymer and ceramics. The thermal heated stress will crack the ceramics before its densification if heating was carried out too rapidly. Therefore the temperature ramp for polymer burning out stage was set as 1°C/min up to 600 °C, followed by a holding time of 1 h. After the burning out, a ramp 5°C/min from 600 °C to 1250 or 1350 °C was applied with a holding time of 2 h at the maximum set temperatures. After that, the furnace switched off automatically and the samples cooled down naturally to room temperature in the furnace. The sintering temperature versus time history is presented in Fig. 3.7.

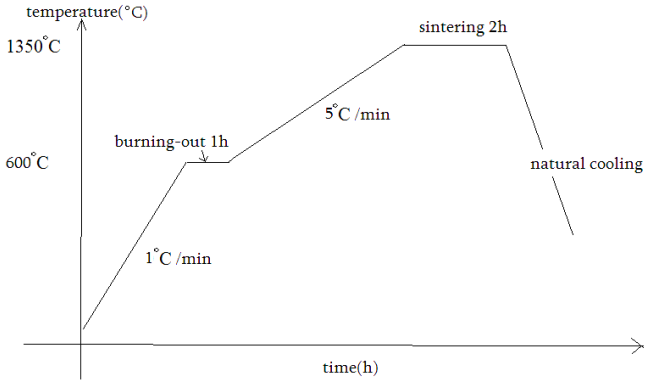

Fig. 3.7: sintering schedule of ceramics coated polymer foam

Sintered ceramic foams of 8 PPI and 22 PPI sintered at 1350 °C for 2 h were obtained as shown in Fig. 3.8. The ceramic foam was from impregnation of 0.5 wt. % CMC in suspension which increases the viscosity in order to avoid the de-coating of slurry from the surface of the struts. This was particularly beneficiary as seen in the Fig. 3.8 that 8PPI has homogeneous structure and excellent pore connection (left and middle) from visual inspection. The impregnation showed that the slurry could easily flow through the cellular structure and accumulate at the bottom, there 0.5 wt. % CMC was added to the slurry. However, the slurry the same slurry with 0.5 wt. % CMC showed less beneficiary impregnation to 22 PPI foam due to smaller pore size and higher viscous resistance to impregnation. 22 PPI foam started exhibiting partial closed cell with small fraction. The impregnation of 30 PPI foam with the 0.5 wt. % CMC slurry revealed to be completely ineffective as shown in Fig. 3.9. A visual inspection indicated that the as obtained ceramic foam consisted almost of closed cell structure and there were very few open cells. This is not favourable for most typical ceramic foams application such as molten metal filtration, catalyst coating and so on. This suggested that the rheological property should be tailor-made for various kinds of polymer replicas with different pore sizes.

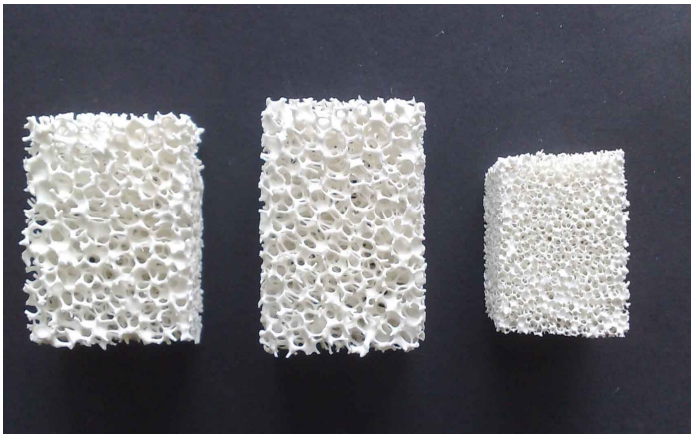

Fig. 3.8: 8 PPI and 22 PPI foams (45 vol. %, 0.8 wt. % Targon) with 0.5 wt. % CMC;

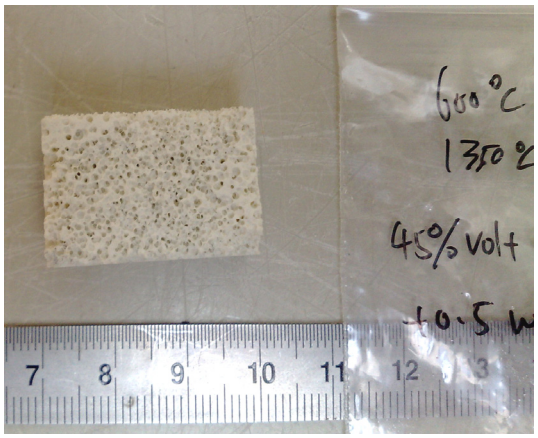

Fig. 3.9: 30 PPI foam (45 vol. %, 0.8 wt. % Targon) with 0.5 wt. % CMC (1 h)

Fig. 3.10 next shows that homogeneous 22 PPI ceramic foams could be obtained when impregnation was made with a suspension containing 0.2 wt. % CMC, which exhibited suitable rheological properties to penetrate the sponge and coated the struts with enough adhesive force. Quantitative homogeneity could be referred to Impulse Excitation technique, however, Fig. 3.10 (a) showed a high level of open cell which promise its application use; On the other hand, Fig. 3.10 (b) showed considerable closed cell structure on the side of the foam. We concluded that the apparent closed cell on the side wall was due to the slurry concentration due to a suction effect of the slurry upon recovering its initial height after squeezing. However this is considered not as detrimental effect since the closed cell structure on side could provide additional mechanical strength but not deteriorating the flow capability through the cellular structure from top to bottom. This also suggested need of a quantitative mean to characterize the impregnation for completely open cell structure on top/bottom and side surfaces to ensure the distribution of the slurry is identical in each processing batch. For instance, the initial weight of slurry after impregnation with a highly open cell structure should be recorded and the ratio between the initial weight and weight of polymer replica should be calculated to determine the optimal impregnation parameters for 8 PPI and 22 PPI foams.

The 22 PPI foam seen in Fig. 3.10 was impregnated with slurry modified with 0.2 wt. % CMC at (PS+IS)/PS ratio of 20. Fig. 3.10 (a) and (b) showed the top and side view of ceramics foam. A comparison was made from Fig. 3.10 (c) and (d) show the top view and side view of polymer replica before impregnation. This experiment also suggested that a suitable weight ratio between initial slurry to polymer replica could provide highly open cell structure. However, the

open cell on side of ceramics foam was seen very poor due to squeezing after impregnation to remove excessive slurry. The slurry was then remained on both sides. Nevertheless, this is not a problem for application as the ceramics foam with enough connectivity in its top-bottom direction is required for actual application. The high concentration of ceramics struts on side could provide enhanced additional strength without affecting any filtration applications.

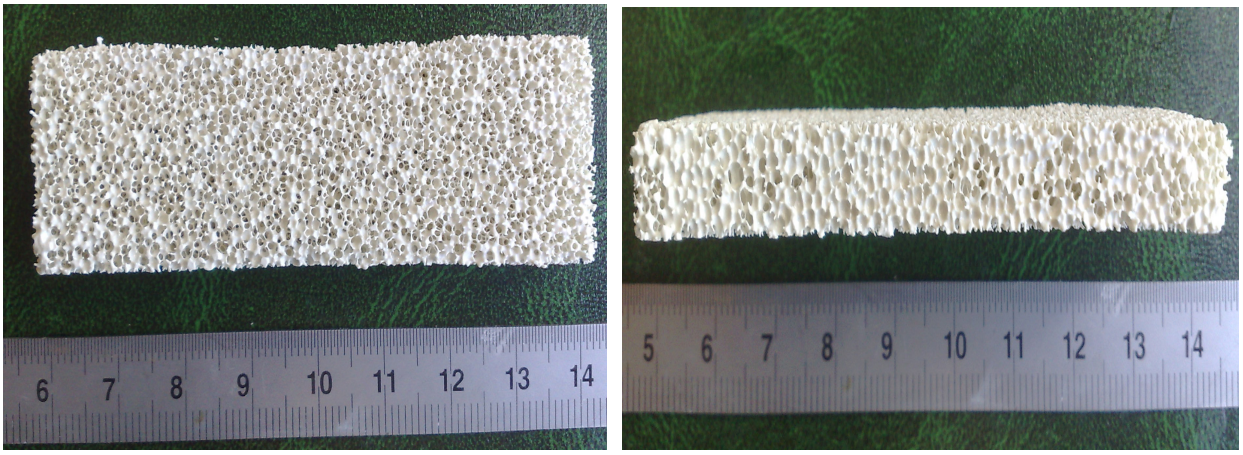

Fig. 3.10: (a) top view of the 22 PPI foam; (b) side view of 22 PPI foam

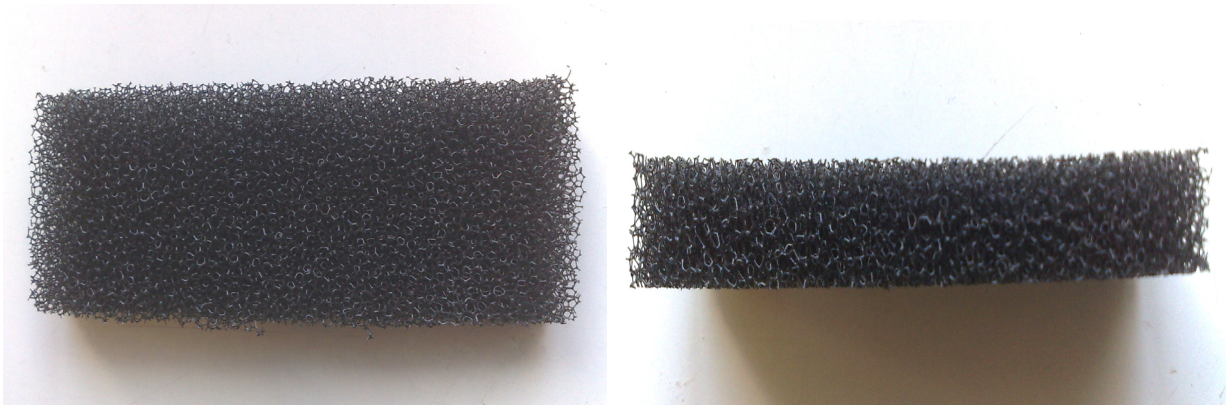

(c) top view of the 22 PPI foam before impregnation;

(d) side view of 22 PPI foam before impregnation

Chapter 4: Results and Analysis

The characterization of starting material is very important for understanding final properties of the bulk ceramics with different sintering schedules. In addition, the parameters such as particle size distribution, of as-supplied powder may also affect the green body properties that are studied. The rheological behaviour of ceramic suspensions prepared as describe in Chapter 3 was studied. The drying-out behaviour of impregnated foams was shown in details by evolution of weight ratio (PS+IS)/PS. The IE measurement evaluates the homogeneity of foam and was performed for selective samples. In addition, X-ray tomography was conducted to study the interior structure of foams and provided 3D actual structural model for Finite Element Analysis. On the other hand, the properties of dense struts of ceramic foams, i.e., microstructure, mechanical properties and compositional variation as function of sintering temperature and time were also studied for optimizing the processing conditions. The dielectric properties were also studied in order to learn about the best sintering schedule and the potential of sintered ceramics for electronic applications.

4.1 Characterization of starting powder

4.1.1 Particle size distribution

Fig. 4.1 shows the evolution of particle size distribution of as-received powder versus ball milling time. The as-received powder has a wide distribution and large mean particle size (the size for which half vol. % of the particles is smaller and the other half is bigger) of 13.2 μm with a tail extending up to > 100 μm. It is supposed that larger sizes are due to the presence of particle agglomerates and this was confirmed by SEM later on. Fig. 4.1 also shows that particle size distribution gradually narrows down and means size shifts towards smaller sizes with increasing ball milling time. After 24 h of ball milling the und mean value was ~6.8 μm, with a small fraction of tail extending up to ~50 μm. The mean particle sizes decreased to ~4.7 to ~2.5 μm after 1 and 2 weeks of ball milling, respectively. All suspension subject to ball milling has been prepared as previously described with 0.8 wt. % dispersant of Targon 1128.

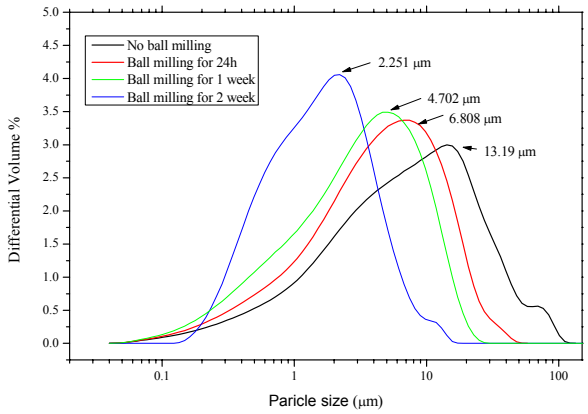

Fig. 4.1: particle distribution of as-received powder versus ball milling time

From the green body compacting point of view, smaller particle size and narrower particles size distribution lead to more homogeneous microstructure in the green body and hence less deformation after sintering. Neto et al [81] summarized the effect of particle size in relation to the sintering and concluded that particle size which normally limits the reactivity from the mixture of natural materials such as Talc, kaolin and alumina as most typical ingredients. Destruction of aggregates increases the specific area and reduces the distance between the particles and hence lowers the sintering temperature at which cordierite phase forms. Meanwhile, the particle size distribution plays important role in green density gradient in slip cast sample due to gravity effect during consolidation. The clogging effect that occurs in slip casting might even predominate over the gravity effect as explained by Ferreira et al [109]. In one word, the occurrence of particle segregation from gravity or clogging during the consolidation process will deteriorate the shaping ability and the reliability of the green body. The inhomogeneity of the particle packing also causes deformations after sintering due to differential shrinkage. In addition, the morphology of the particles also determines the packing ability of a powder with rounded particles being considered to have higher ability to closely fill the space. Milewski et al [110] showed that the green density could be significantly decreased when increasig the particle aspect ratio. The SEM observations in our investigation later on revealed that the particles of precursor powder are not spherical but exhibit a platelet-like morphology due to existence of talc and kaolinite.

In the present investigation, dense and cellular ceramics were made from the suspension with ball milling for 1 week in order to achieve good reactivity and compacting ability with mean particle size of 4.7 μm.

4.1.2 XRD study of composition

The starting powder consists of natural mineral materials without disclosed composition. Therefore X-ray analysis was carried out with Philip PANAnalytical X'Pert Multipurpose Powder Diffractometer (MPD) at Central Analytical Lab (LCA), University of Aveiro. Fig. 4.2 shows the XRD pattern of starting powder from 8° to 95° with angular step of 0.02°. The present of minor phase or deviations from the stoichiometric cordierite will lead to the formation of secondary phases as predicted from the $MgO\text{-}SiO_2\text{-}Al_2O_3$ phase diagram in Fig.1.1. In such context, the quantitative phase analysis (QPA) based on X-ray diffraction using standard silicon powder as internal reference was conducted. This method using internal reference is also favourable in quantifying glassy phase in reaction in big fraction.

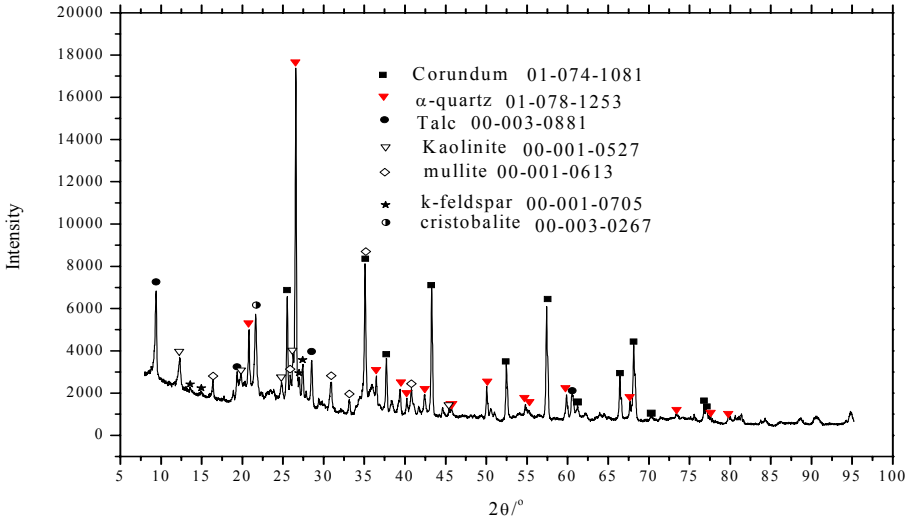

Fig. 4.2: XRD phase analysis of starting powder

The XRD results revealed the powder is a complex mixture of several natural materials or rare synthetic mineral such mullite. It contains at least of 7 types of minerals of crystalline phase namely corundum, α-quartz, Talc, Kaolinite, mullite, K-feldspar and Cristobalite (product of pre-calcinations of kaolinite) with ICDD PDF code. However there are still very few minor peaks left un-indexed and we consider that this is difficult due to the complexity of the as-supplied material. It is also noticed that there is a hump from 15-30º, which Johnson [111] has attributed to the presence of kaolinite calcined at low temperature (900 °C). The raw powder also shows existence of mullite, probably derived from kaolinite calcined at higher temperatures.

The silicon and starting powder were mixed by planetary ball milling for homogeneity and

then studied by XRD. The phase quantities were determined by Rietveld method as shown in Fig. 4.2. The Rietveld refinement plots show the green (observed) and the red (calculated) curves, as well as the difference (blue) curve between measured and calculated data.

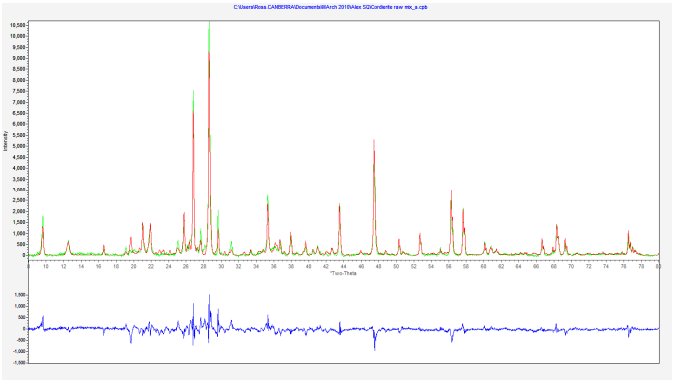

Fig. 4.3: Rietveld refinement of Cordierite raw mix powder, R_w (%) =17, Sig=4.2

Fig. 4.3 shows a reluctant agreement between the experimental and simulated curves. Nevertheless, the agreement is acceptably good provided the complexity of the starting material. The QPA was performed with software "*Siroquant"* developed by Sietronics Australia (http://siroquant.com/) under agreement of trial use to the program supplier. The result was validated by comparing the wt. % (16.68 wt. %) of silicon added to the starting powder to the wt. % refined from Rietveld refinement, 20 wt. %. The slight difference is likely due to imperfection of crystallinity of silicon powder. The result of quantitative phase compositions after re-calibration respective to pre-determined silicon wt.5 is shown in Table 4.1.

Table 4.1: minerals and composition of as-supplied powder

Minerals	**Chemical formula**	**Wt.%**	**ICDD Code**
Corundum	Al_2O_3	29.40	01-074-1081
Talc (triclinic)	$Mg_3Si_4O_{10}(OH)_2$	18.00	00-003-0881
α–Quartz	SiO_2	16.08	01-078-1253
K feldspar	$KAlSi_3O_8$	8.64	00-001-0705
Mullite	$Al_6Si_2O_{13}$	8.52	00-001-0613
Kaolinite	$Al_2Si_2O_5(OH)_4$	8.37	00-001-0527
Cristobalite	SiO_2(HT Polymorph)	4.64	00-003-0267
Glassy phase	n/a	6.35	n/a

Siroquant is newly appeared commercial software in Rietveld refinement for QPA and some comments are given by the supplier regarding the *Siroquant* results: the Chi^2 or goodness of fit number is approximately 3.4 and this is typical and R_w factor is good. The silicon content from

Rietveld refinement is slightly higher (17% weighed to 20% by refinement). This is acceptable considering the crystallinity of the sample. The Cristobalite phase is not a perfect fit meaning that the existence of this phase is in doubt but it is believed this was the best option. In one word, *Siroquant* provides quite satisfactory results compared to all programs available. However, the price of such program limited our further use after trial. In our following investigation, only MAUD is used to conduct QPA for XRD.

As previously addressed in 1.2 Chapter 1, sintering of cordierite via solid state route usually requires temperature above 1350 ^{o}C. In the present study, Talc and kaolin in the composition are found that would supposedly decrease the crystallization temperature, compared to the synthesis using pure metal oxides according to [11]. Also, Antisiferov et al [30] showed that compositional variations significantly affect the properties of cordierite and a preliminary calcinations of Talc has a considerable influence on the mechanical properties of cordierite formed by single stage solid state sintering. And, Talc could be obtained from a blend composition containing feldspar or pegmatite. Therefore, n the composition of Rauschert blend we found the K-feldspar which is added as fluxing agent in order to reduce liquidation temperature and hence allowing sintering in presence of liquid phase.

4.1.3 DTA/TGA study

The thermal properties and the sintering schedule of the as-supplied starting powder were studied by DTA/TGA. The DTA/TGA ramp rates were set at 5 ^{o}C/min (the same used in the sintering - Fig. 4.4) and at 10 ^{o}C/min (Fig. 4.5).

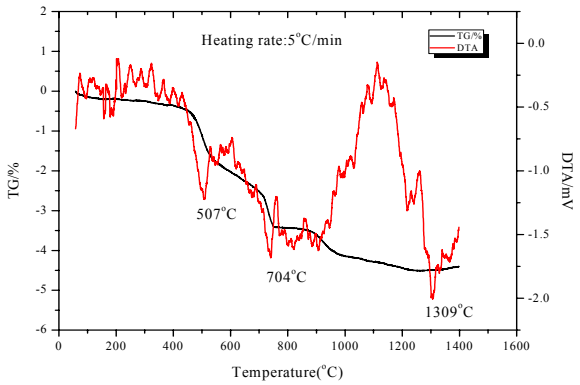

Fig. 4.4: DTA/TGA study of the as-received powder

Fig. 4.4. shows that precursor powder underwent weight loss steps characteristics of the

minerals present in the composition, namely of Kaolinite at about 450-550 ºC – centred at about 507 ºC and due to the loss of structural water, and Talc (and eventually minor amounts of other associated minerals such as Chlorite, Chrysotile and Calcite) at about 680-730 ºC–centred at about 704 ºC, and at 880-940 ºC, due to the loss of structural water and accompanied by the formation of ensatite ($MgSiO_3$) and silica [20, 112]. Fig. 4.4 also shows that DTA signal has low intensity to noise ratio, probably due to the low heating rate that mitigates the thermal differential effects between the sample and the standard material.

Fig. 4.5 shows the DTA/TGA plots of precursor powder at a heating rate of 10 ^oC/min. It can be seen that the endothermic peaks were shifted to higher temperatures, as expected, while the peaks appear are of higher intensity. The result also showed that the signal to noise ratio was improved for measurement at higher heating rate. Gonzales-Velasco et al [113] studied DTA curve of mixture with similar composition of 20.6 wt.% alumina, 34.5 wt.% kaolin, 40.4 wt.% talc, and 4.5 wt.% silica at higher rate, i.e., 15 ^oC per min, in which the first endothermic peak was in range of 550-650 ^oC while the second is around 900-950 ^oC. It appeared that the higher the temperature ramp the bigger shift to higher temperature peak, therefore the DTA study of phase transformation should be used with care when the heating conditions vary.

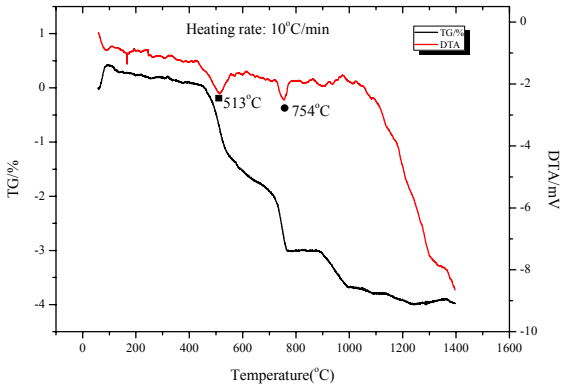

Fig. 4.5: DTA/TGA curves for as-received powder at 10^oC/min

The peak at first endothermic around between 500-550 ^oC also corresponds to transition of kaolin into metakaolin by losing hydroxyl group, OH and transition from α-quartz to β-quartz according to [113]. The XRD study in Fig. 4.6 revealed the result that kaolin's peak at 12.5^o has disappeared since metakaolin has amorphous structure. It is apparent that second endothermic peak was followed around 700-750 ^oC and this is supposed corresponding to the transition of Talc

to protoensatite which is high temperature polymorph of ensatite ($Mg_2Si_2O_6$), amorphous silica and water vapour according to [113]. However, the Quantitative Phase Analysis suggested that relative wt. % Talc has decreased but no apparent identification of protoensatite therefore the protoensatite transition is not mandatory.

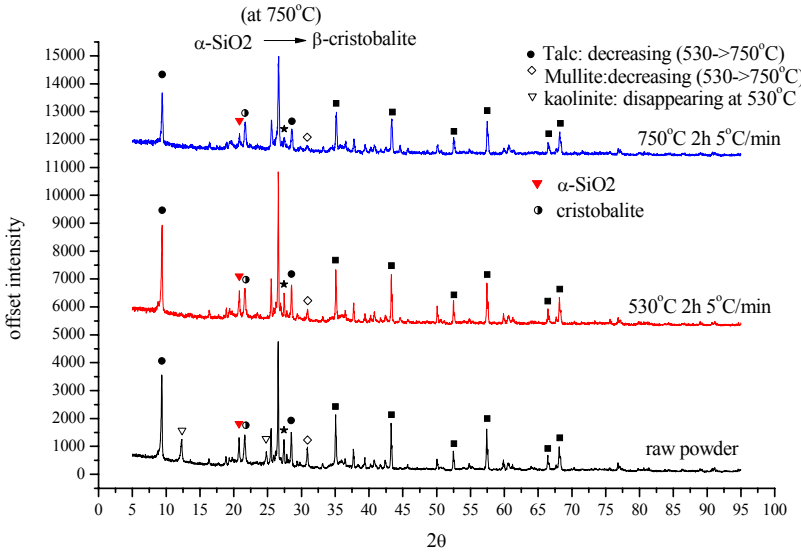

Fig.4.6: XRD for powder calcined at 530°C and 750°C for 2h;

Fig. 4.7 analyzed the phase fraction in the mixture calcined at first and second endothermic peaks. Kaolinite has not been included since it completely transformed to metakaolin above 530°C. It is noted that the relative ratio between α-quartz and β-Cristobalite varied significantly from 530 °C to 750 °C. However, the wt.% increase of mullite and corundum was not in agreement to the result by [113] in which the decomposition of metakaolin should increase the wt.% of mullite and corundum since the total weight of the mixture was decrease detected by TG curve. The likely reason to account for this difference could be lying with the fact that the DTA/TG test was run in inert atmosphere (Ar) while the sintering was conducted in air rich in oxygen. However, oxidization could not affect the amount of mullite and corundum. The problem was considered due to presence of other components of materials present in the starting powder that is not revealed due to commercial secret. Nevertheless, an *in-situ* XRD experiment in vacuum is expected to address the problem discussed above.

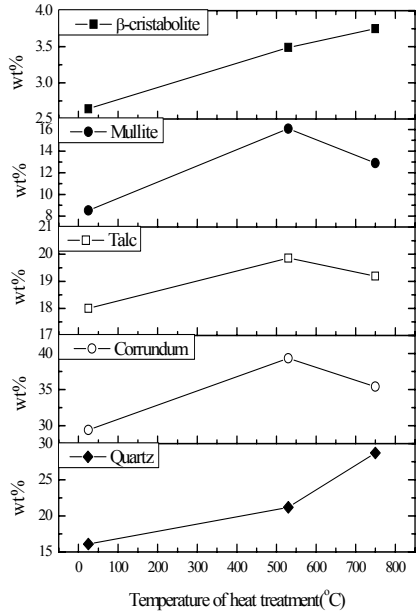

Fig.4.7: Rietveld Analysis of composition change in DTA (RT-750°C)

Finally, the peaks above 1300°C does not correspond to any transition of single oxides in the precursor powder but only their fusion according to [113]. The peak that is seen around 1309°C is therefore associated with the solid state reaction to form a-Cordierite that takes place between 1250-1400°C according to [113]. This study was also carried out in our XRD with variable sintering temperature and similar agreement was found.

4.1.4 SEM study of morphology

SEM studied the particle morphology and size distribution of starting powder. Fig. 4.8 shows strong particle agglomeration from the as-supplied precursor powder. It is also seen that the powder is in laminar morphology and the laminar structure appears to be in range of 2-10 μm similar to that found by particle size analyzer in Fig. 4.1. Those laminar flakes that situated at the top surface of the bigger particle underneath are picked up and a semi-quantitative image analysis with Feret diameters (The longest distance between any two points along the selection boundary of particle) of particles were evaluated by ImageJ* to determine the particle size distribution in Fig. 4.9.

* ImageJ is free-of-charge software dedicated to digital image processing and calculation developed by National Institute of Health, USA. http://imageJ.org

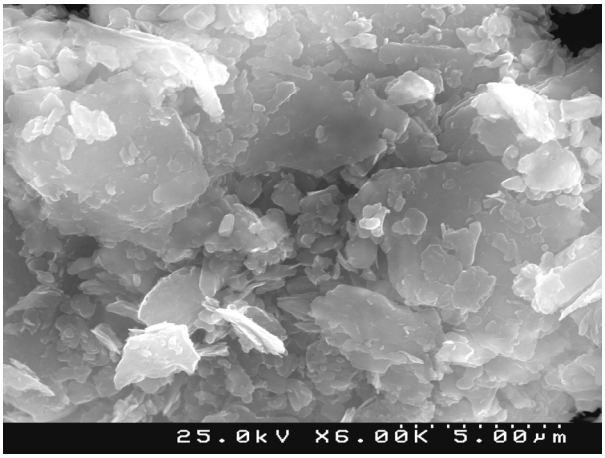

Fig. 4.8: laminar structure of as-received powder

Fig. 4.9 shows image analysis results from measurement of particles' dimensions along its longest axis. The number of particles that fall into certain size range is plotted versus the particle size therefore one could also obtain a semi-quantitative particle size distribution. The distribution showed that the most probable particle size is around 16 µm which drop significantly over 25 µm and approach to zero when the particle sizes is over 40 µm. This result is in agreement to the particle analysis that is found by laser diffraction around 13.19 µm.

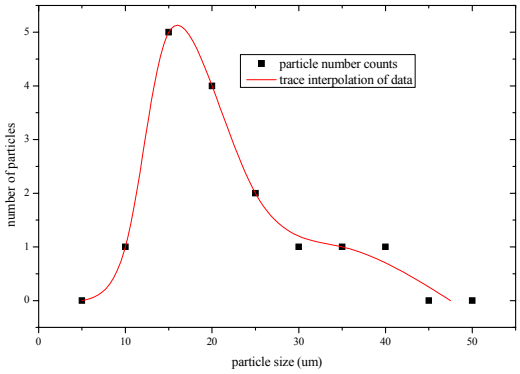

Fig. 4.9: particle size distribution by Image Analysis

4.2 Rheological and drying behaviour

The rheological properties of the suspension prepared with 45 solid vol.% loading and dispersed with 0.8 wt.% Targon 1128 were characterised the flow ability and viscosity. The ideal suspension must have adequate fluid character so as to impregnate the polymer replica thoroughly and uniformly, even for small cell size foams such as 22 PPI. However, it is difficult to make a good impregnation when the viscosity is too low and fluid character is too accentuated. This is particularly important in case of impregnating 8 PPI polymer which has rather large cell size. The

viscous character of the suspension is expected to be appropriately adjusted to enable a thin and uniform coating layer on the polymer struts.

Fig. 4.10 (upper portion) shows the flow (shear stress vs. shear rate) curves, and the corresponding viscosity vs. shear rate curves, respectively, for: (1) the starting suspension (containing 45 vol.% solids loading dispersed with 0.8 wt.% Targon in absence of thickening agent); (2) the starting suspension with added 0.2 wt.% of CMC as thickening agent; (3) the starting suspension with added 0.5 wt.% of CMC as thickening agent; (4) the suspension (3) but tested a second time after being at rest for 2 min. The pink curve in Fig. 4.10 (bottom, left), is the water dynamics viscosity ~0.001003 at RT for comparison [114].

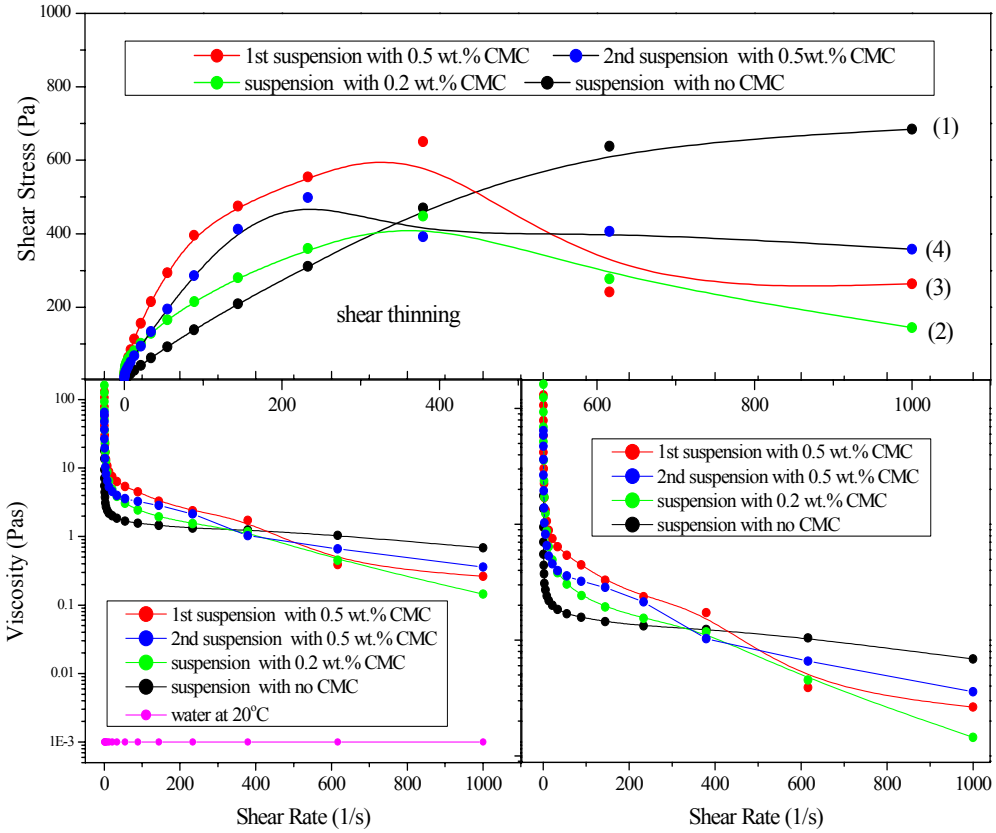

Fig. 4.10: rheology of 45 vol% solid suspension, 0.8wt. % Targon at different, 0,0.2,0.5 wt.% CMC

From Fig. 4.10 (top), it can be seen that suspension (1) exhibits shear thinning behaviour along the whole shear rate range tested. The shear thinning characteristics within the low shear rate range (up to about 385 1/s) gradually accentuated with increasing amounts of CMC (curves 2 & 3). However, the shear stress reaches maximum values at about 385 1/s), decreasing as the shear rate further increases. Such a decrease can be interpreted as: (i) a break down effect of

CMC chains under high shear rates. In that case, the resulting shorter molecular chains will not be able to bind to the same number of particles as before, and the viscosity is expected to decrease; (ii) an alignment of the adsorbed polymer chains along the flow direction, thus offering less resistance to flow. In order to ascertain which of the above phenomena would prevail in the present circumstances, the suspension (3) was tested a second time after being at rest for 2 min. The resulting curve 4 shows an overall similar trend, but with less levels of shear stress being required to deform the system. These results support the hypothesis that the CMC chains are somewhat degraded under high shear rates, but do not contradict the possibility for the adsorbed polymer chains to alignment along the flow direction. Accordingly, both should be considered at the present stage. More detailed studies will be required to shed further light on this issue, including higher number of repeated shear rate/shear stress tests with the same suspension and longer rest times between the tests, which are beyond the scope of this thesis.

The relevant practical information that can be drawn from Fig. 4.10 with the aim of pursuing the objectives of thesis are as follows: (i) increasing added amounts of CMC enhance the structuring effect of the suspensions at rest and near rest conditions, therefore, hindering the flow after impregnation of the polymeric replicas, thus contributing to obtain ceramic foams with uniform density; (ii) CMC binder should be dosed according to the structure of the polymeric sponge replicas; (iii) the suspensions with added CMC should not be submitted to high shear rate regimes since the degradation of polymeric chains occurring under that conditions will alter the rheological properties and thus, the control over the process.

Another way to characterize the suspension impregnation behaviour is to study the weight change of the polymer strut immediately after impregnation until fully dried. The polymer foam is often excessively coated and the excess suspension might block the cell open structure. The control of impregnation and open cell ratio vs. close cell can be obtained by the amount of ceramics slurry impregnated onto polymer struts. The experiment of impregnation vs. polymer's weight is illustrated in Fig. 4.11 and Fig. 4.12. The polymer after impregnation has to be squeezed to remove apparent excessive slurry to leave most of the cellular structure as open cells. However, if the slurry was removed too much the coating will be inadequate to cover the struts. Therefore, a trial-and-error experiment was planned to achieve homogeneous open cell structure and the (PS+IS) vs. drying time was recorded. It was found that the (PS+IS)/PS weight ratios have to be different for the 8 PPI foams if homogeneous coatings are to be obtained. The ratio was determined by the weight of (PS) and impregnated slurry (IS) immediate after impregnation (PS+IS) to the polymer struts weight (PS) shown in Fig. 4.11 and Fig. 4.12. The optimized ratio for coating 8 PPI and 22 PPI were found to be 16 and 20 respectively. This is considered an

effective mean of one-off control to microstructure based on impregnation since once the slurry dries out it is not possible to impregnate any more slurry.

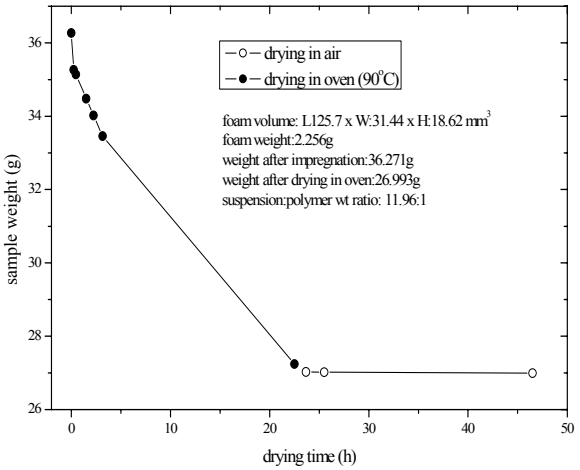

Fig. 4.11: 8 PPI ceramics green foam drying behaviour after impregnation 45 vol.% loading no CMC

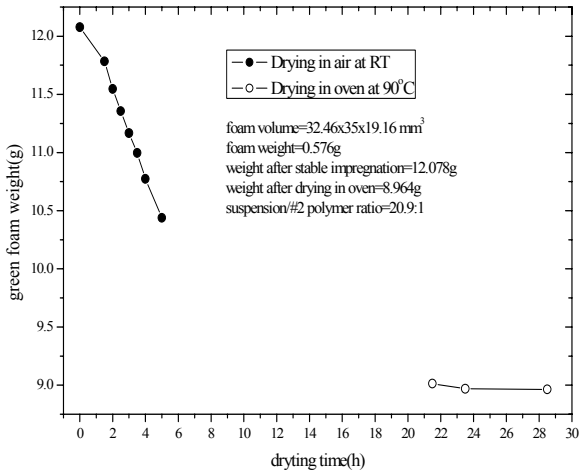

Fig.4.12: 22 PPI ceramics green foam drying behaviour after impregnation 45 vol.% loading no CMC

4.3 Composition and Microstructure of bulk

XRD was employed to study the composition relationship versus sintering schedule. Pyconometry was applied to measure the bulk density of the sample prepared under different sintering schedules. However, the relative density is not straightforward to obtain since the ceramic has a complex composition instead of being monophonic and monolithic. SEM study was performed to characterize the porosity of 2D surface which was assisted with quantitative image analysis under the assumption that 3D porosity is represented from image analysis. The porosity is related to relative density and compared to density calculation from XRD and relative density measurement by Archimedes method. The thermal expansion properties and thermo-mechanical stability (thermal shock resistance) are relevant for refractory applications. The foams made of cordierite-mullite ceramics were studied with non-destructive Computed X-ray tomography yielding actual 3D information of microstructure and providing the basis of numerical simulation for mechanical properties. Impulse Excitation technique was used to measure the Young's modulus and foam's homogeneity in order to counter the problem of machining the ceramics with precise geometry. Flexural and Compressive strength are characterized by unidirectional compression to give basic parameters for mechanical properties. In addition to this, the cordierite is also one of the most promising materials to replace current Integrated Circuits (IC) substrate that electronics industry requires due to its low-ε (dielectric constant). Therefore dielectric properties are shown at Room temperature.

4.3.1 XRD study

Fig. 4.13 showed result of X-ray pattern from the sintered product of powder raw mix. The pattern was analyzed using JADE MDI 5.0 first and we discovered that the cordierite phase has formed and occupy the primary proportion in the sintered body while mullite and Al_2O_3 are left presumably due to non-stoichiometry mixing that excessive mullite and Al_2O_3 are not consumed during sintering. All diffraction peaks well above the background is indexed and it is safe to say that the powder raw mix which consists of at least 5 minerals has now transformed into a mixture of Cordierite, Alumina, Mullite and small amount of residual quartz and cristobalite.

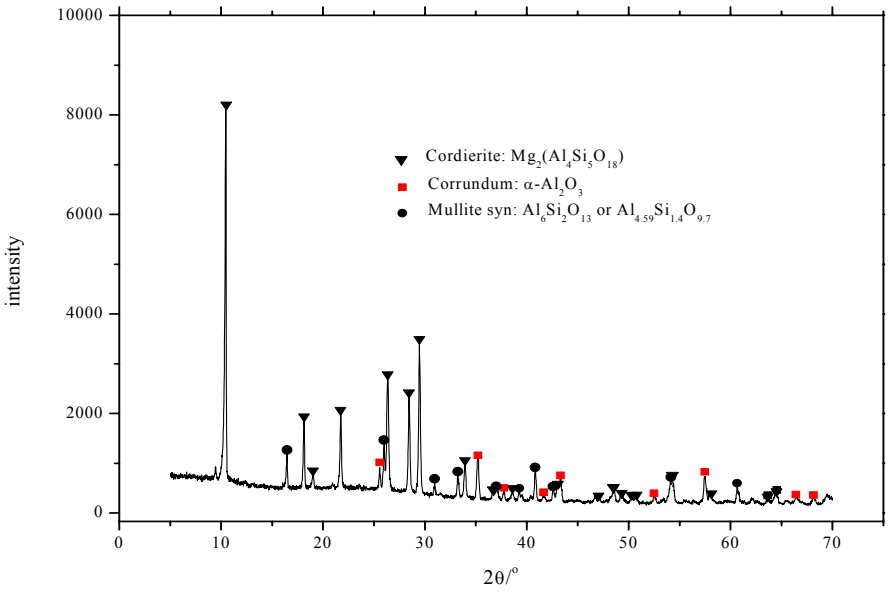

Fig. 4.13: XRD phase analysis of sintered powder at1350°C for 2h

Fig. 4.14 shows one example of quantitative phase analysis by using MAUD. The method is based on whole pattern refinement also known as Rietveld refinement. The refinement showed that the weighted residual factor is around 21% and the goodness-of-fit is 2.7. The result is consistent with the general guideline for QPA for mixture of complex phase required the Rwp is around 15% and GOF is around 2. However numerous attempts were tried in order to improve the fitting without success. The refinement for other XRD patterns showed similar Rwp and GOD (are not shown here) indicates that general error may occur in QPA interpretation. However we have to bear in mind with the fact discovered in Chapter 2 that MAUD is most favourable software in QPA in case of mixture of simple oxides. Therefore we show the QPA results that are given in Table 4.2

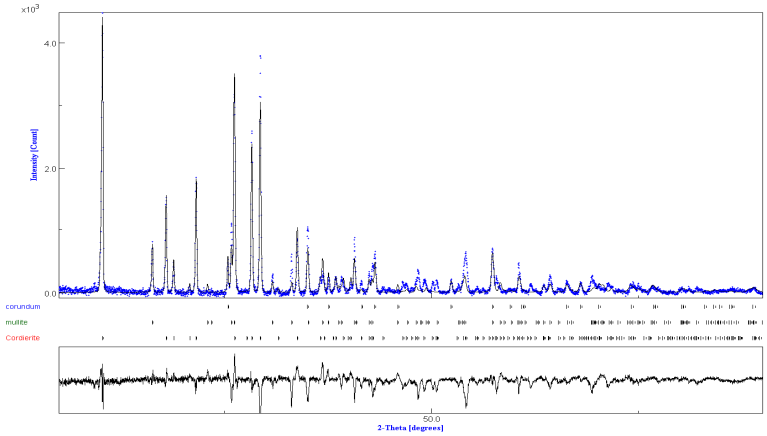

Fig. 4.14: Rietveld analysis of bulk ceramics at 1350°C for 2h, sig=2.7 R_w=0.21

Table 4.2: XRD Composition of bulk ceramics

Minerals name	Wt.%	Vol%
Cordierite	53.6	57.43
Mullite	34.89	34.71
Corundum	7.68	5.78
α-quartz	1.64	2.06
theoretical density	2.69	g/cm^3
apparent density	2.51	g/cm^3
relative density	93.3%	-

4.3.2 Variable temperature XRD

As we have seen from phase diagram in Chapter 1, the ternary ($MgO-SiO_2-Al_2O_3$) phase diagram (Fig. 1.1) is very complex in terms of phase transition and the phase evolution with temperature. Therefore, the as-supplied starting powder was studied using variable temperature XRD at different temperatures from 950 to 1500^oC. The temperature variable XRD patterns are seen in Fig. 4.15.

Fig. 4.16(a) shows another example of Rietveld refinement for the sample heat treated at 1250 ^oC, 2 h, and the quality of fit in terms sig=3.31, $R_{exp}(\%)=7.35$, $R_w(\%)=24.39$. A convention for good Rietveld refinement is R_w (%) <5. For complex mixtures of the phases, the R_w (%) is expected to be around 15-20. In our refinement, the R_w (%) is around 24 which are higher than this standard. However, it appears that further improvement is difficult to obtain since the (100) peak of cordierite around 10^o is always underestimated. This is likely due to background developed from glassy phase which is not easy to be accounted for in refinement. Fig. 4.16(b) shows Rietveld analysis of sample sintered at 1425 ^oC for 2 h. All other Rietveld refinements showed similar quality as in Figure 4.16(a), (b) and are not shown here. The results from Rietveld QPA are plotted in Fig. 4.17 to observe compositional variation as function of sintering temperature.

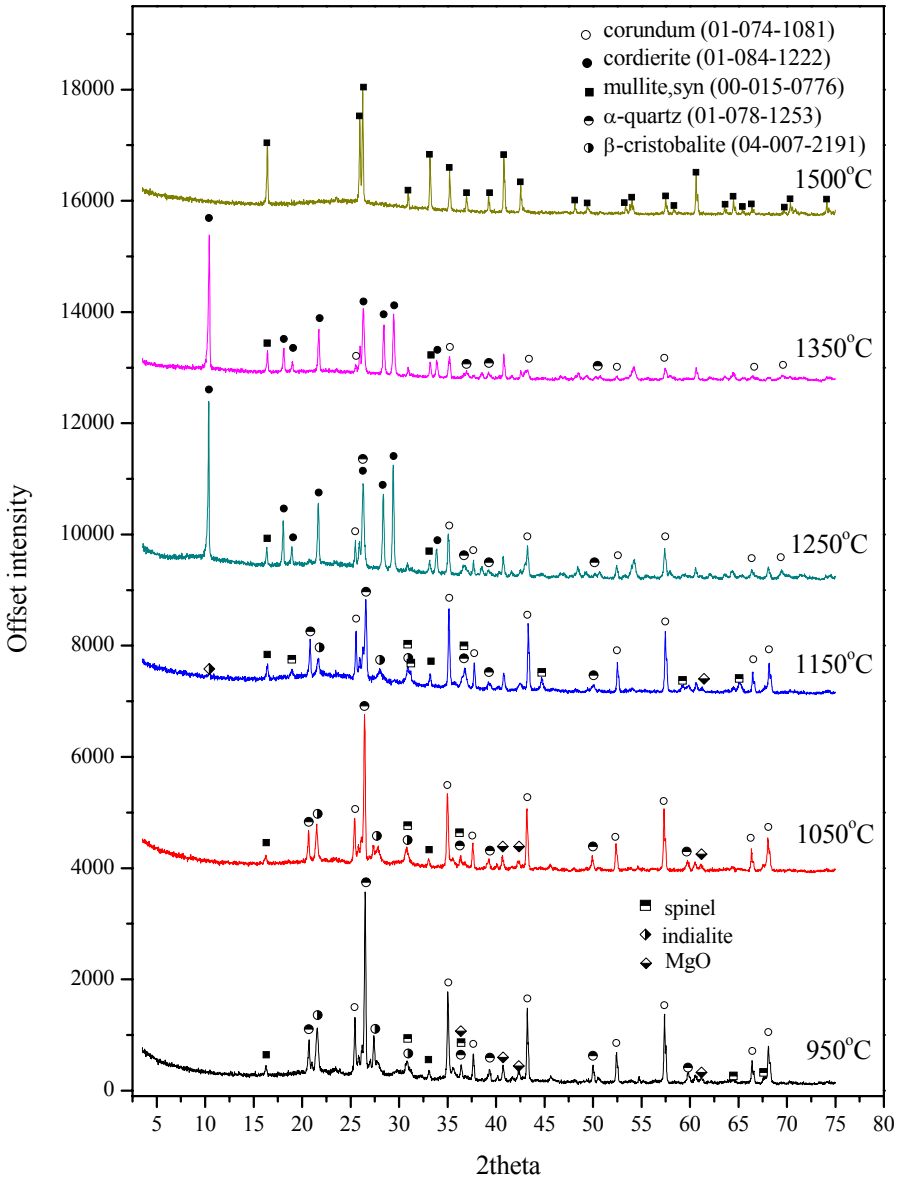

Fig.4.15: XRD phase study of sample from variable temperature with heat treatment for 2h

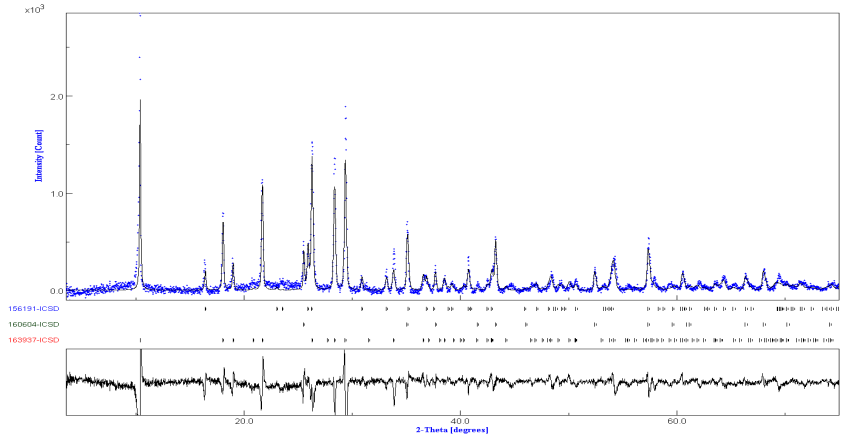

Fig. 4.16(a): Rietveld analysis of bulk ceramics at 1250°C 2h, sig=3.31, R_w (%) =22.39

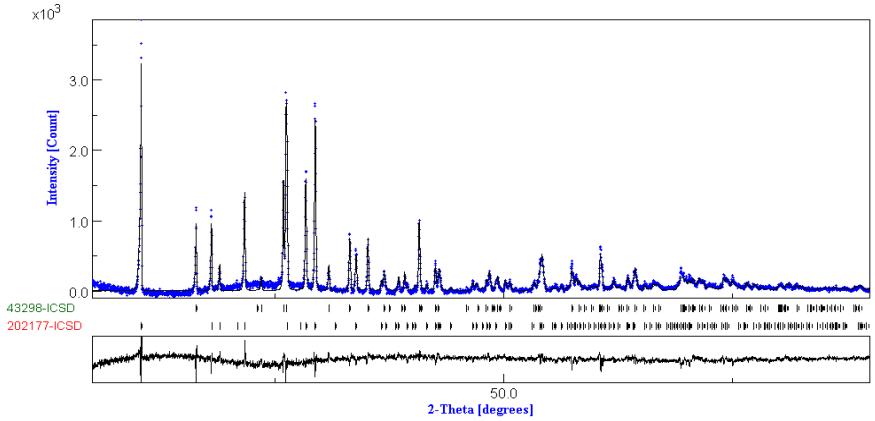

Fig.4.16 (b): Rietveld analysis of bulk ceramics at 1425°C for 2h, Sig=2.08, R_w (%) =11.27

The QPA study in Fig. 4.17 was only conducted with range between 950 - 1500 °C, which covers the temperature of cordierite crystallization according to the phase diagram in Fig. 1.1. One can see that the cordierite phase only exists within in a pretty narrow temperature range from 1250 °C to 1425 °C, whilst the wt. % cordierite at 1350 °C appears to be highest across the range. Mullite was seen as continuously increasing and the some mullite existed in the as-received cordierite raw powder. Khezrabadi et al [115] studied the formation of mullite with similar composition of starting materials and SEM studies revealed that the formation of mullite is due to kaolin and excessive alumina in the batch. However the content of mullite continues to increase with temperature increasing, being the main phase at 1500 °C. Although mullite has better mechanical properties than cordierite, the sintered sample does not show such advantage. This is due to the abundant liquid phase formed during high temperature sintering at 1500 °C and the evolving gaseous phase leading to many micro cracks within the sample. In some cases the micro cracks become macro cracks which are visible to naked eye and this will significantly decrease the mechanical strength.

Corundum, α-quartz and β-Cristobalite are both seen decreasing as temperature goes up. At 1425 °C, the other MAS oxide phases were completely reacted and monolithic cordierite (43 wt. %) and mullite (57 wt. %) are the only crystalline phases. Further increasing the temperature will cause melting of cordierite phase and mullite with highly porous structure due to cordierite melting is the single crystalline phase at 1500 °C.

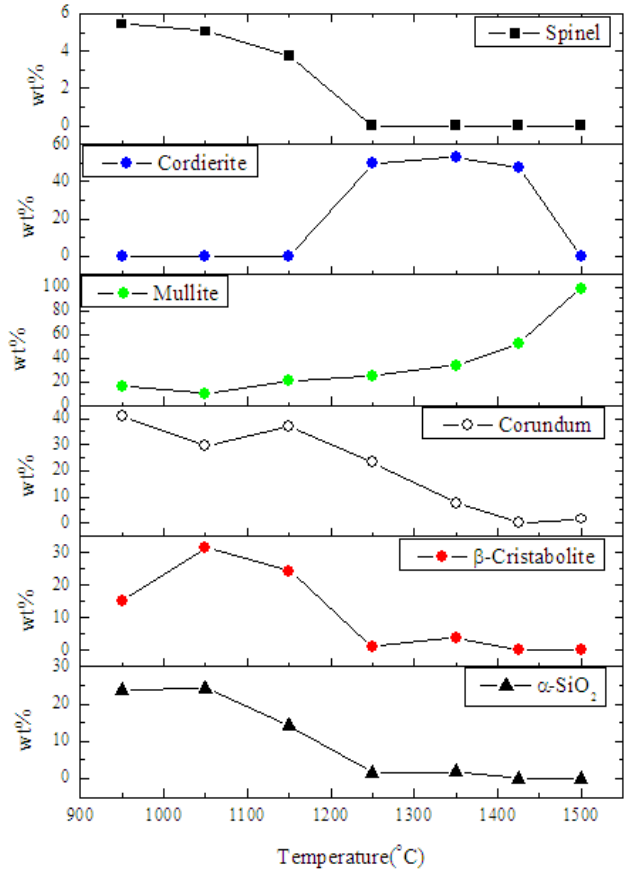

Fig. 4.17: Rietveld analysis of wt. % variation versus sintering temperature

XRD study shows that the cordierite phase is single dominant α-cordierite. This is in agreement with the work sintered with excess MgO mole ratio [11]. Xu et al [116] studied the cordierite synthesis via solid state reaction without additives from a mixture of rectorite $(Na,Ca)Al_4(Si,Al)_8O_{20}(OH)_4 \cdot 2(H_2O)$, Talc and Alumina. The sintering was conducted between 1200-1400 °C which is similar to this investigation. Xu found that the decomposition of cordierite takes place over 1350 °C and excessive liquid phase appeared and the sintered ceramics showed significant deformed shape and visible bubble formation on the surface as consequence. This result is in agreement to our findings from XRD result that cordierite phase disappeared above

1350 ^{o}C and the sintered sample has deformed shape and giant air bubbles across the body. According to X-ray diffraction data, Fig. 4.17, the formation of the cordierite phase seems to begin only above 1150 °C. This is somewhat higher than the result reported in [117]. However, we should be aware that additives such as Fe_2O_3, Bi_2O_3 and V_2O_5 were added, which significantly reduced the sintering temperature [117]. The sample consists of mullite, quartz, and magnesium silicate. It was also found that raising the additives wt.% and extending the heating time led to higher cordierite content, which is favorable for a higher mechanical strength and thermal stability of the monolith [117]. Nevertheless, the results reported by Johnson et al [111] that cordierite phase development started visibly at 1250^{o}C is in good agreement with our results as seen in Fig. 4.17, showing the characteristics peak roundabout at 10.4^{o} of 2θ. The agreement is also found well between our results in Fig. 4.17 to [111] that at 1350 ^{o}C the cordierite was the major phase. The cordierite phase fraction was found by Rietveld refinement at around 53% which is very close to reported value of 52% calculated under similar conditions [111]. In [111] the study showed that upon further heating from 1350^{o}C to 1420^{o}C, the cordierite phase fraction increased up to 90%. However the cordierite phase sintered at 1425^{o}C does not increase but decrease in our case illustrated in Fig. 4.17 and the mullite phase has continued to increase instead. This is due to the deficiency of MgO. Meanwhile, the characteristics peak was reported to diminish at 1440^{o}C due to melting of cordierite phase [111]. This is in agreement with sample heat treated at 1500^{o}C in our XRD study. We proposed excessive MgO introduced into the original powder could attain the higher formation of cordierite.

The reason why the crystallization temperature of cordierite was found to be higher in our study compared to the phase diagram and other people's work [27] is likely due to the compositional effects. Tsai et al [27] showed that the excess of SiO_2 and Al_2O_3 will significant increase the activation energy of α-cordierite formation and hence the temperature. Therefore the cordierite phase was only seen for heat treatment above 1250 ^{o}C as SiO_2 and Al_2O_3 were abundant in the original powder.

The QPA result shown in Fig. 4.17 has important implications in material design in case of using the as-supplied starting powder. The contents of cordierite and mullite have the most significant effects on the final properties and it is desirable to see that monolithic mullite and cordierite composite exists at 1425 ^{o}C.

Fig. 4.18 shows the temperature/time dependent XRD phase composition of the compacted raw powder upon sintering under different indicated schedules. According to Montrosi et al [118] not only sintering temperature but also the time play important roles in the formation of

crystalline phases. Therefore, this XRD study versus time was conducted to see temporal effects on crystallization in Fig. 4.18.

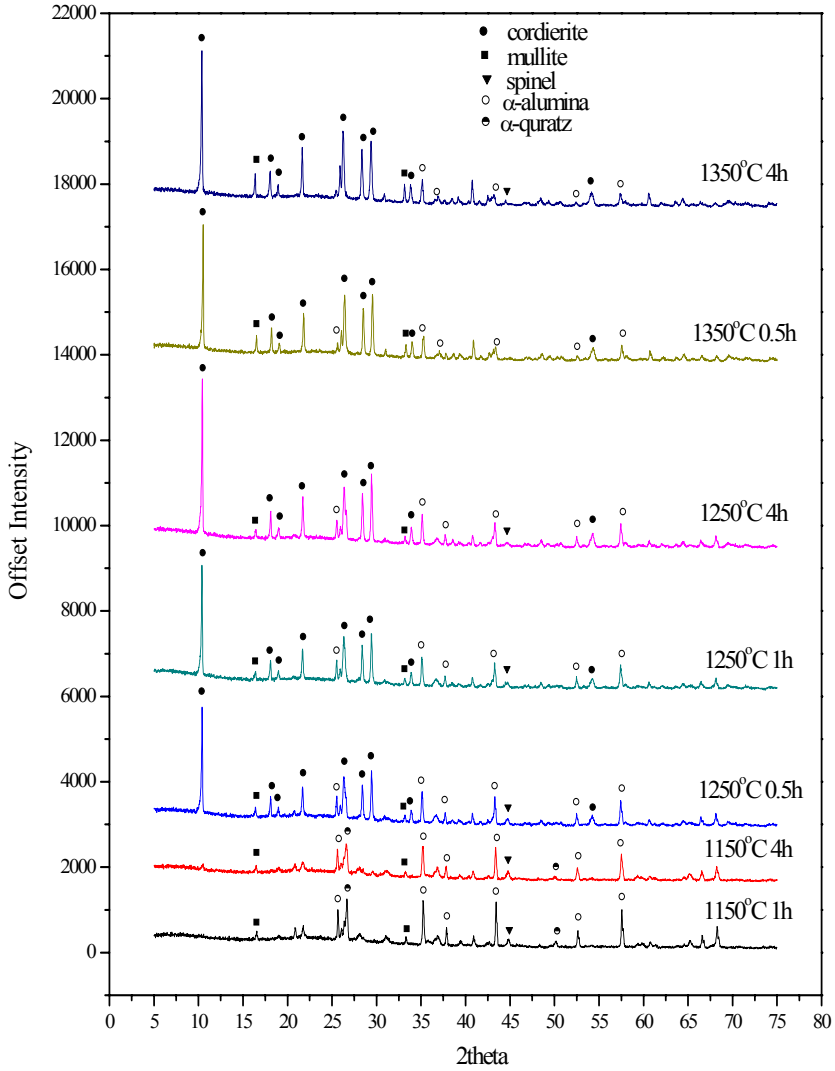

Fig. 4.18: XRD of cordierite sintered bar at various times and temperatures

At 1150 °C, a careful observation revealed the appearance of a peak around 10° from XRD pattern of 4 h compared to 1 h. The peak was ascribed to indialite instead of cordierite. The indialite is a polymorph of synthetic cordierite compared to natural cordierite. The comparison between patterns with indialite at 1150 °C for 4 h to that without indialite at 1150 °C for 1 h is illustrated in detail from Fig. 4.19. This result suggests that the indialite has not been formed after 1 h at 1150 °C, but it requires a longer time at this temperature to crystallize. Its formation could be facilitated by additives that decrease the activation energy, as reported by Montrosi et al [118]. And when the temperature was further increased to 1250 °C for only 0.5 h, the crystallization takes place overwhelmingly into cordierite revealed by XRD.

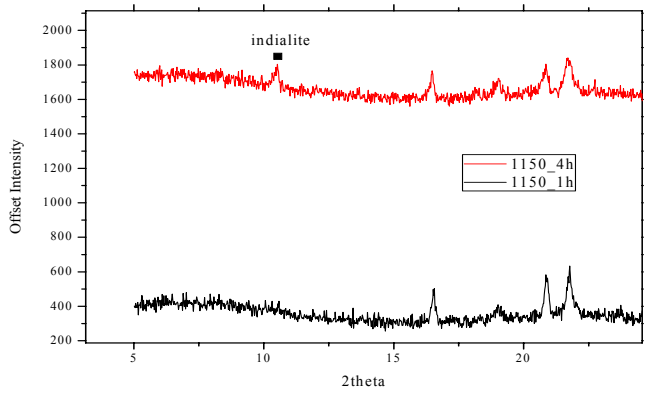

Fig. 4.19: XRD of cordierite sintered bar at 1150 °C for 1h and 4h

The spinel phase was also found from 1150 to 1250°C regardless of sintering time. However, it became invisible in the pattern of 1350 °C, 0.5 h and reappeared in pattern of 1350 °C of 8 h as indicated in Fig. 4.20. This suggested that further increasing the time probably does not provide benefit in terms of cordierite formation from this powder of non-stoichiometry composition since the cordierite phase could transform to spinel which does not provide as good thermal/mechanical/electrical properties as cordierite. Gonzales-Velasco et al conducted the time variable XRD study on cordierite crystallization at 1400 °C and discovered that the α-alumina and spinel was decreasing over increasing time and this is also supported by our data illustrated in Fig. 4.20 as the line corresponding to α-alumina decreases over increasing time. However, contrary to that disclosed in [113], we detected spinel phase after heat treating for 8 h. The true cause of this peculiar finding is under investigation.

The crystallization was seen to be clearly affected by the duration of heat treatment as demonstrated also in Fig. 4.20. The amorphous background was significant after 1 h of heat treatment, while the amorphous background decreased significantly upon increasing its duration. This suggests that crystallinity could be improved upon longer exposure to heat treatment. But this does not contradict to another route of improved crystallinity by adding nucleation agents such as TiO_2.

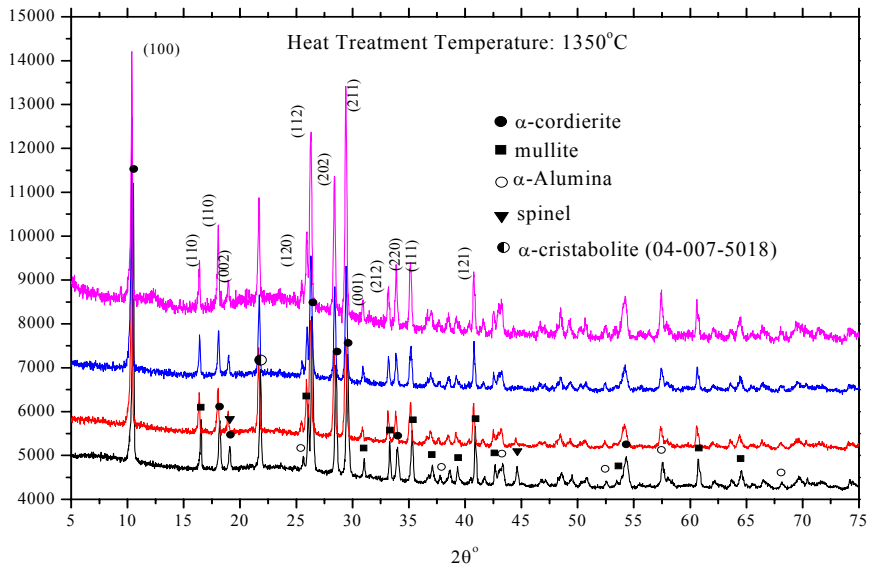

Fig. 4.20: XRD of cordierite sintered bar at 1350 °C for different lasting times

The properties of cordierite composite ceramics were found closely related to the fraction between cordierite and mullite. Therefore, we conducted a semi-quantitative estimate of fraction ration between two phase by comparing the peak intensity from (100) of cordierite and (110) of mullite. The reason we chose these two peaks is that there is no other phase peak located at the same position and the peak intensity is solely contributed from each phase respectively. Although as previously introduce, the use of peaks' intensity ratio is not the most reliable method for quantitative phase determinations. However, this comparison is made on the ratio of most intense peak between two phases existing in the same mixture, therefore it is safe to say that the ratio will give a semi-qualitative description whether the phase fraction is increased or vice versa. Figure 4.21 shows that the ratio between cordierite (100) and mullite (110) reaches maximum from sample sintered for 2 h. This is consistent with XRD results presented in Fig. 4.20 showing that further increase of sintering time will likely promote spinel phase instead of increasing cordierite phase fraction. Therefore, we determined that 2 h is an optimal time for heat treatment of the original powder.

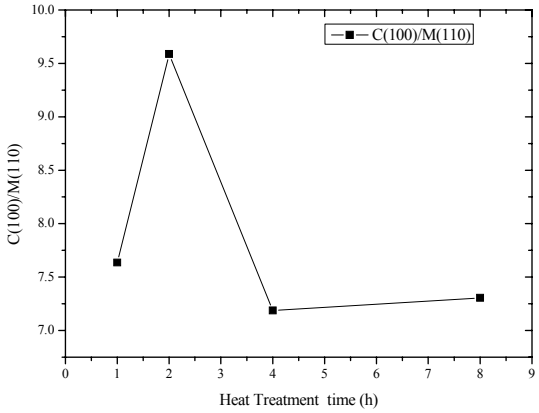

Fig. 4.21: intensity ratio between cordierite (100) and mullite (110)

4.3.3 SEM study with quantitative image analysis

The SEM micrographs of ceramics sintered at 1150, 1250, 1350 and 1500 ^{o}C for 2 h are shown in Fig. 4.22 to Fig. 4.24 and Fig. 4.26. The morphology changes as a function of sintering temperature. The mullite formation with its characteristics needle-like grains is not apparent from the lower sintering temperatures. The images were taken at two magnifications of x200 for porosity studies with quantitative image analysis and x3000 to reveal the presence of needle shape mullite grains. Fig. 4.22 (a) shows that the average pore size is very small compared to those at 1250 ^{o}C and 1350 ^{o}C. With increase of temperature, the average pore size increased significantly. Although no significant porosity differences could be observed between 1250 ^{o}C and 1350 ^{o}C, the changes in average pore size and shape (aspect ratio) are likely to affect the mechanical and thermal properties.

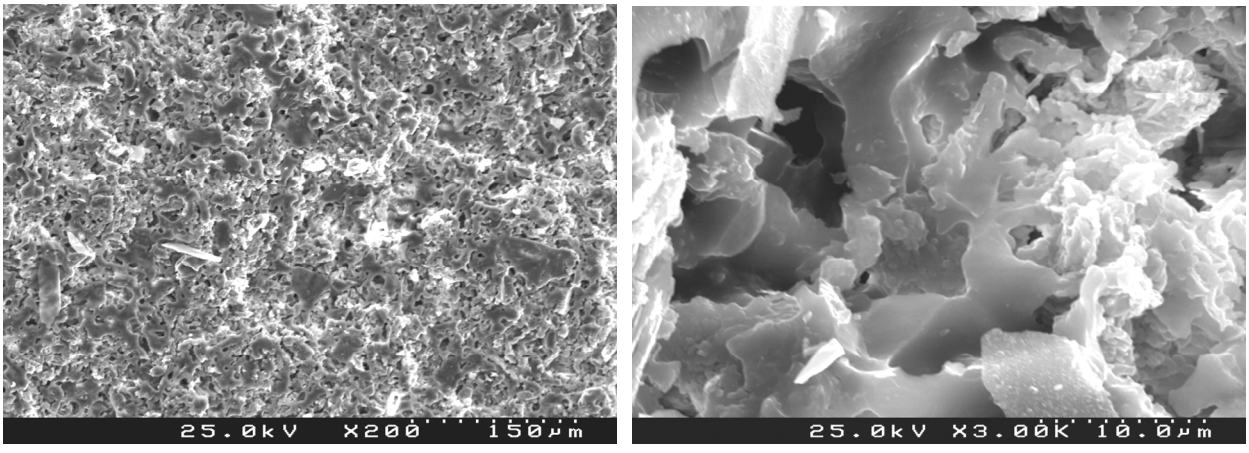

Fig. 4.22: 1150 ^{o}C 2 h (a) porosity study; (b) alumina-mullite-silica microstructure

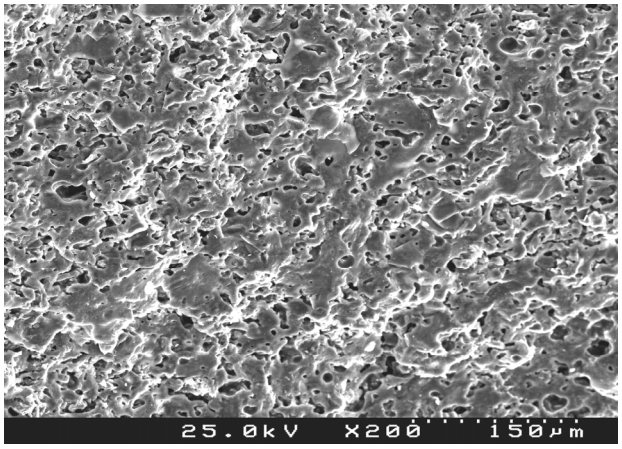

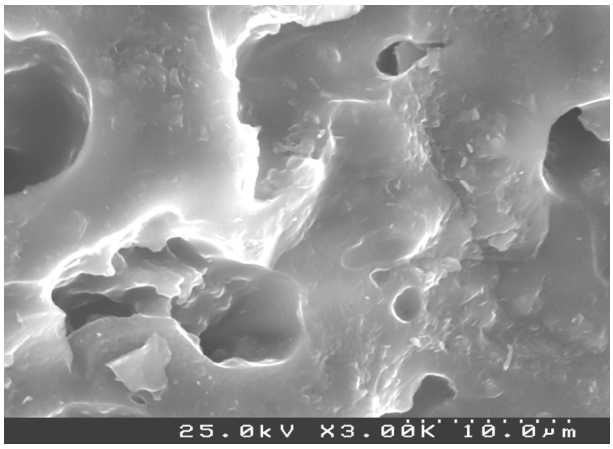

Fig. 4.23: 1250 °C 2 h: (a) porosity study; (b) mullite-cordierite composite microstructure

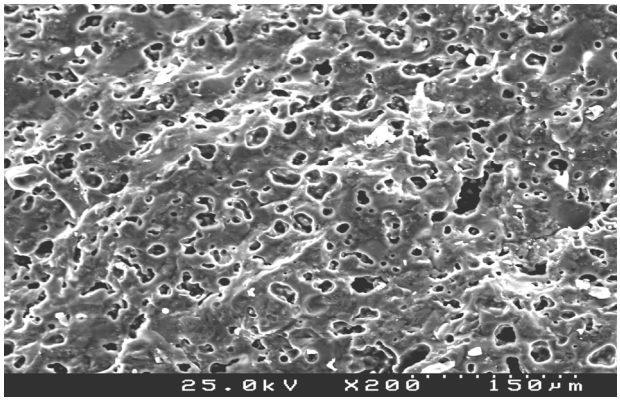

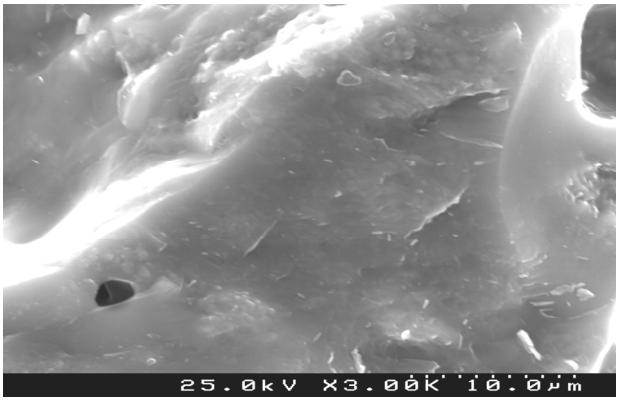

Fig. 4.24: 1350 °C 2 h: (a) porosity study; (b) mullite-cordierite composite microstructure

The mullite has needle-like grains usually from suitable heat treatment conditions, which act as an effective reinforcement for enhancing ceramics mechanical properties to resist fracture. However, SEM images do not show any mullite needle shape grain formation at 1150 °C. Instead, a laminar morphology is apparent, which then transforms into a more homogeneous structure with some needle-shape grains embedded within. This becomes still more evident from higher magnification SEM images (x 10 K and x 20 K) as shown in Fig. 4.25 (a) and (b). The XRD results of the sample heat treated at 1350 °C revealed the presence at mullite has largest fraction in cordierite matrix at 1350 °C and therefore the mullite formation is more visible in Fig. 4.25 with somehow needle-like structure tips pointed outward and embedded in the cordierite matrix. Fig. 4.25 (b) showed microstructure of the same area with magnification of x20 K. It is more clearly shown that the mullite needle shape phase start to grow and appeared out of the cordierite matrix due to mullite's distinct needle-like shape. However Fig. 4.25 (b) showed only tips of the needle shape mullite without knowledge of its length or aspect ratio. Therefore image analysis of mullite phase will not be performed since the area fraction of mullite tips cannot predict properly

the phase fraction of mullite to compare to XRD.

Fig. 4.22 to Fig. 4.24 also revealed a fact that the pore cells has significantly increased over increasing sintering temperature. Although the porosity was decreasing however the pores sizes are increasing suggesting that the pore coalescence takes place as result of fusion of smaller pores into bigger one. This is actually an indication of densification process.

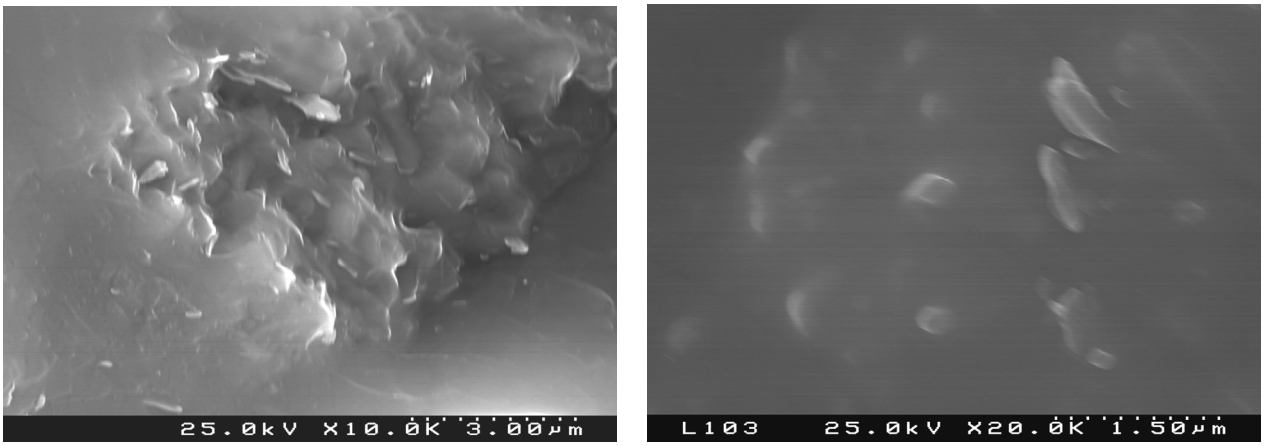

Fig.4.25: 1350^{o}C (a) tips of needle-shape mullite; (b) tips of needle-shape mullite grains

Fig. 4.26 shows two SEM pictures with different magnifications of 'pure' mullite (as detected by XRD) microstructure after sintering at 1500 ^{o}C for 2 h. Needle shape mullite grains embedded in a glassy phase are seen in Fig. 4.26 (b). This intermingled mullite crystals tend to enhance crack and fracture resistance. At higher magnification in Fig. 4.26 (a) a high density of large pores is also evident, which is supposed to have derived from gas release inside a liquid phase. The high porosity fraction tends to significantly decrease the mechanical properties despite the positive contribution of interlocking between the needle shape mullite grains.

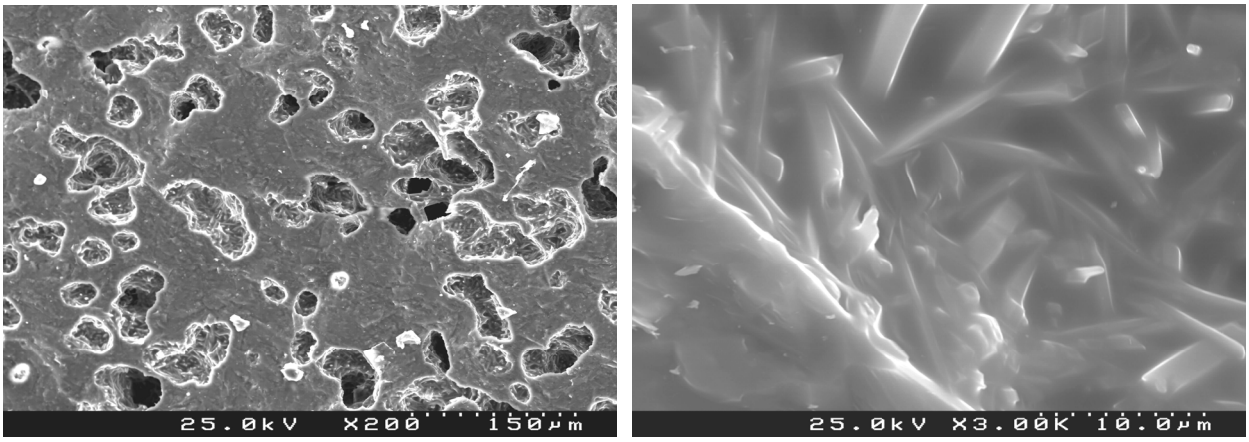

Fig. 4.26: 1500 ^{o}C (a) porosity study (b) needle-shape mullite grains

The SEM method associated with image processing is importance to evaluate the relative density of sintered specimens due to lack of monolithic phase to evaluate the 100% dense density as a function of heat treatment conditions, such as temperature, time and additives. The relative density is proportional to the relative volume fractions of solid and gas (porosity) phases. Therefore, characterizing porosity is an easily way to determine the relative density for the complex composite materials. Conventionally, semi-quantitative method is applied by drawing lines randomly across the images and the length between intersected points and measure the size of pores. The average is then calculated from a collection of such length data and the average pore size is adopted based on the assumption that they are spherical. Nowadays, quantitative image analysis has become trendy in evaluation the information from first hand data. The pore normally has irregular shape and should not be approximated to a sphere. Therefore, Photoshop tool (magnetic lasso) is used to draw the actual shape of the pore and the pore with 2D actual shape is then highlighted as seen on the right hand side of Figs. 4.27 to 4.29. The 2D actual shape is considered as particles and the area fraction of those particles are analyzed in ImageJ. There are also a few assumptions that have to be made in this investigation. Quantitative image Analysis is reliable and applicable to predict the area fraction of the pore structure in 2D dimensions and the assumption has to be made that they have a similar dimension in depth direction. In addition, we took SEM images from 3 individual fracture surfaces and an average was taken to calculate the volume average porosity.

The images were analyzed with ImageJ and one example was shown in Fig. 4.27 on the left to analyze porosity of bulk ceramics sintered at 1350^{o}C for 2h. The structures were pre-processed in Photoshop and input into ImageJ for particle calculation. Similarly all other images are processed and calculated to yield the area fraction of particle and hence the relative density.

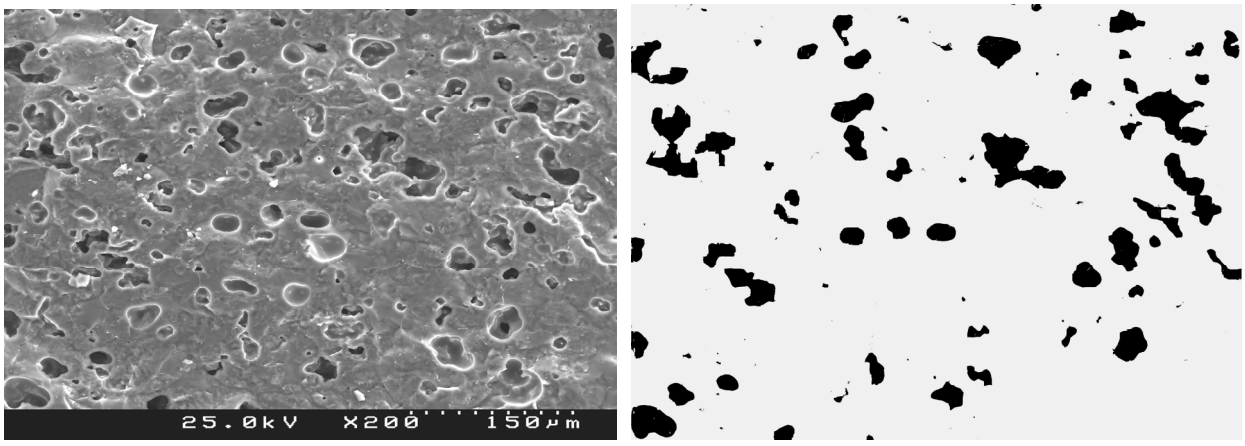

Fig. 4.27: (1350^{o}C for 2h): porosity8.8%, relative density: 91.2%

From the SEM microstructures analyzed by image processing, the calculated average relative porosity of the bulk ceramics sintered at 1350 ^{o}C for 2 h is 8.7%±0.36%. Therefore the relative density is 91.3%.

This result is subject to comparison to the XRD phase fraction study and theoretical density of each phase. The XRD phase analysis showed that the main phases at 1350 ^{o}C for 2 h were α-Cordierite+mullite+α-Alumina+α-SiO_2. The theoretical densities are reported in Table 1.1. The XRD phase fraction is in terms of wt.% and the wt.% is converted to vol.% in order to calculate the theoretical density of composite containing 52 wt.% Cordierite, 34.9 wt.% Mullite, 7.7 wt.% a-alumina and 1.6 wt.% α-SiO_2; The volume fraction for each phase are calculated from their respective density and determined as 56.7 vol.%, 35.3 vol.%, 5.9 vol.%, 2.1 vol.%, respectively. Based on results aforementioned, the theoretical density is calculated as 2.73 g/cm^3. The measured apparent density (previous section) was ~2.52 g/cm^3. Therefore, the relative density determined by the ratio between apparent and theoretical densities is 92%. The relative density estimated from SEM+Image analysis is 91.3%, and the result estimated from XRD and Pyconometry measurements indicates a relative density of 92%. The agreement is excellent. Therefore, the combination SEM and XRD shows good potential to estimate the relative density (and porosity fraction) in comparison to the procedure based on dimensions and weight measurements of the specimens.

Similarly, SEM study was conducted to selected samples sintered at 1250 ºC and 1500 ^{o}C to see morphology and the porosity. The semi-quantitative analysis was not applied to sample at 1150 ^{o}C since the pores are too small to identify in ImageJ. The results are shown in Table 4.3.

Table 4.3: porosity determination by semi-quantitative image analysis

Sample	2D porosity (%)
1500 ^{o}C (2 h)	~32.4
1350 ^{o}C (2 h)	~10
1250 ^{o}C (2 h)	~3.1*

In addition to the SEM and XRD studies, the true density of original powder and sintered material in polycrystalline form at different conditions were studied with Pyconometry method. The SEM study has proved that the bulk ceramics are not fully dense but exhibit a porous structure with ~10% porosity. The pores are enclosed in the bulk sample and not accessible by the measurement media in Pyconometry method which causes significant error. Therefore

Pyconometry studies must be carried out using the sintered powder without closed pores. Prior to measurement, the powder after sintering was subject to hand grinding in alumina crucible with vigorous force for 30 mins until the powder appeared to be fine powder without visible bigger particles. The examples of SEM images for the powdered sintered at 1350 ^{o}C and 1250 ^{o}C for 2 h are illustrated in Fig 4.28 and Fig. 4.29, respectively, suggesting that no pores remained inside the particles. With this proof in hand, we are certain that the Pyconometry measurement provides the true density of the materials after sintering. It should be mentioned that the fraction of open pores versus closed pores are possible to be characterised by boiling water test with sample inserted into boiling water and measure the weight afterwards. However this was not performed yet in the scope of this thesis.

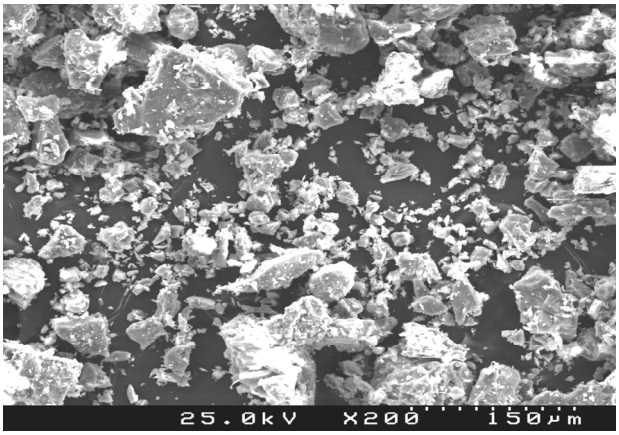

Fig. 4.28: powder at 1350^{o}C for 2h

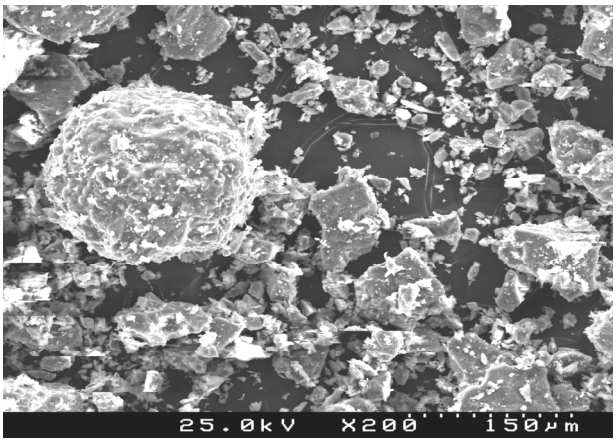

Fig.4.29: powder at 1250^{o}C for 2h

The data on density of green raw powder and sintered polycrystalline sample under different conditions are showed in Table 4.4. However, relative density is somehow difficult to get since the sintered product is a composite materials containing 3 or more phases of ceramics such as cordierite, mullite and corundum and other phases as shown in XRD study. The SEM study also proved that the bulk ceramics is not fully dense composite but a porous structure with ~10% volume porosity. Therefore, relative density seems to be more reliably obtainable from quantitative SEM image analysis associated to XRD phase analysis as demonstrated in section 4.3.4. The graphic representation of the relative density variations under different sintering schedule is shown in Fig. 4.30 and it appeared 1250 ^{o}C is always more preferential to achieve higher relative density whilst longer sintering time also appeared to be beneficiary to increase the relative density at the same temperature. For instance, a relative density of ~98% is obtained for sample sintered at 1250 ^{o}C for 4h. This will be revisited with support of higher mechanical strength. However, SEM study of relative density as previously introduced is planned to verify the measurement by Pyconometry.

Table 4.4: Pyconometry studies of relative densities versus sintering temperature and time

Materials	Real density g/cm^3	Bulk density g/cm^3	Relative density (%)
Green body	3.007±0.45%	1.8591	61.97*
	3.007±0.45%	2.095	69.86**
1500 °C	2.80	2.3537	82.58
1350 °C			
1 h	2.539±1.15%	2.379	***93.70****
2 h	2.519±0.32%	2.347	91.17
4 h	2.55±2.48%	2.373	93.04
8 h	2.554±1.36%	n/a	n/a
1250 °C			
1 h	2.608±1.15%	2.486	95.3
2 h	2.593±0.62%	2.5057	***96.63***
4 h	2.581±2.34%	2.55	***98.79***
8 h	2.581±0.47%	n/a	n/a
1150 °C			
1 h	2.825±1.00%	2.26	80
2 h	2.790±1.76%	2.2675	81.27
4 h	2.793±1.48%	2.2596	80.77

*: Slip cast **: PVA binder modified dry pressing

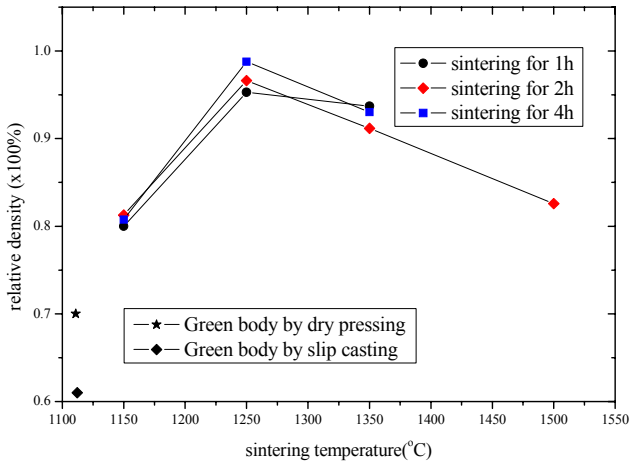

Fig. 4.30: density of bulk ceramics versus sintering temperature or time

4.4 Thermal properties

The cordierite has excellent thermal shock resistance largely due to its extremely low thermal linear expansion coefficient, which reduces the thermal stress generated during quenching or

flame heating with temperature changing rapidly up to ΔT~500-1000 K. However, the sample in our investigation consists of cordierite, mullite, and α-alumina as primary phases, as well as other minor phases such as α-SiO_2 and β-Cristobalite. The thermal expansion and hence the thermal shock resistance will be very much dependent on the phase fraction of the aforementioned composite.

4.4.1 Thermal Expansion

The dilatometry studies were carried out to 4 specimens sintered at 1500, 1350, 1250, and 1150 °C respectively for 2 h. within the temperature range from 50 °C to 1200 °C. The change in length *versus* temperature is shown in Fig. 4.31.

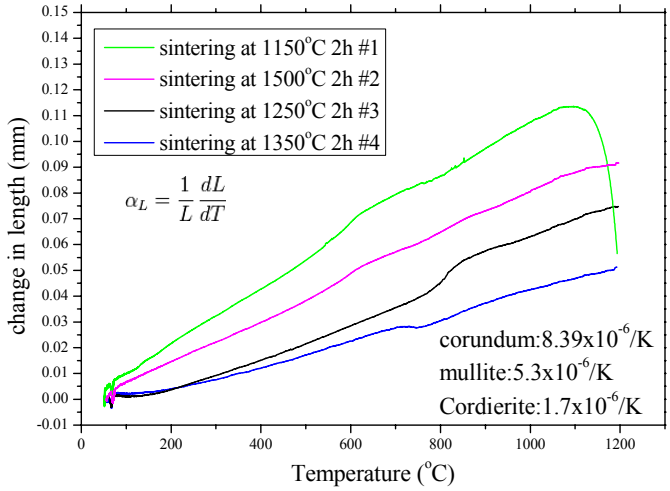

Fig. 4.31: thermal expansion of cordierite-mullite system

All the curves show some slope changes. For #1, #2 specimens the changes start at around 600°C and end at around 750-800°C; while they appear shifted to higher temperatures, ~750 °C for #3, and 800 ºC for #4 specimens, respectively. Mirwald [12] studied the Mg-cordierite which is the same phase as studied in this work. He found two discontinuities in the thermal expansion at 275±25 °C and 600±50 °C, assumed to represent higher-order phase transitions [12]. The first slope change is related to a minimum in specific volume, implying unusual expansion behavior (negative thermal coefficient) at low temperatures. However, we did not find such first discontinuity as seen in Fig. 4.31. Nevertheless, an estimate of slope change at about 700-750° C for the #4 specimen sintered at 1350 °C for 2 h yields a negative TEC. Table 4.5 gives the summary of the measured experimentally and the calculated values of TEC for sample at each temperature for comparison purposes.

Table 4.5: Experimental TEC versus Calculated TEC from XRD Composition

1500 °C 2 h	Cordierite	Mullite	Corundum	α-SiO_2	Calculated TEC(10^{-6}/K)	Experimental TEC(10^{-6}/K) (50-1000°C)
TEC(10^{-6}/K)	1.7	5.3	8.39	0.45		
Wt.%	0	100	0	0	5.3	4.24
Vol.%	0	100	0	0		
1350 °C 2 h	Cordierite	Mullite	Corundum	α-SiO_2		
TEC(10^{-6}/K)	1.7	5.3	8.39	0.45		
Wt.%	52	34.89	7.68	1.64	3.31	3.2
Vol.%	57.43	34.71	5.78	2.06		
1250 °C 2 h	Cordierite	Mullite	Corundum	α-SiO_2		
TEC(10^{-6}/K)	1.7	5.3	8.39	0.45		
Wt.%	49.57	24.59	24.36	1.529	3.77	4.29
Vol.%	54.74	24.45	18.33	1.92		
1150 °C 2 h	Cordierite	Mullite	Corundum	α-SiO_2		
TEC(10^{-6}/K)	1.7	5.3	8.39	0.45		
Wt.%	0	0.209	0.393	0.253	4.52	5.786
Vol.%	0	0.252	0.359	0.387		

The investigations showed that, first of all, a coefficient of linear thermal expansion depends on the sintering temperature. Fig. 4.32 plots the TEC variation *versus* sintering temperature for 2 h. It is found that the minimum TEC value, indicating optimized sintering schedule located at 1350°C. This was somehow expected since cordierite fraction is the highest at 1350°C. On the other hand, high TEC material of alumina reaches minimum at the same temperature. Although mullite fraction is higher at 1350°C but the effect of less corundum is more dominant. The effect of this compositional variation is reflected in reduction of TEC of the cordierite composite in Fig. 4.33. The TEC of 3.31×10^{-6}/K from the investigation is in some agreement with that reported by Kehzrabadi et al [115] of 3.18×10^{-6}/K at the same firing temperature.

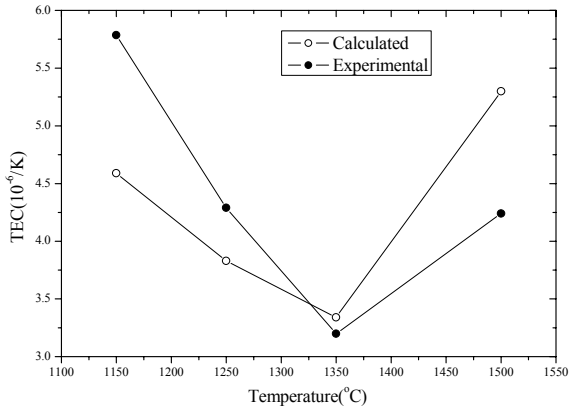

Fig. 4.32: TEC variation versus sintering temperature for 2h.

Further heating up to 1500 ^{o}C does not yield better TEC since the cordierite phase has completely transformed into mullite. It is possible that the TEC at 1350 ^{o}C is not the minimum one and Johnson et al [111] showed that the TEC of cordierite could go as low as $0.74x10^{-6}$/K at 1420^{o}C with more than 90% phase fraction of cordierite. This helps us to further explore the TEC variation versus temperature and heating time due the difference of starting materials composition.

Giovanni Bruno et al [119] used Neutron powder diffraction to show that the variation of lattice parameters *a*, *b*, and *c* of cordierite were compared to the macroscopic thermal expansion. In this work the *a*, *b* axes show different thermal expansion at high temperature, but equivalent thermal expansion behaviour below 800^{o}C. The TEC could be as low as 10^{-7} to $2.5x10^{-6}$, depending on MgO molar ratio [11]. The more MgO the higher content wt. % of cordierite and hence, the lower was the obtained TEC. This suggested us to try to add extra wt.% of MgO in the original raw mixture powder in order to deplete mullite phase at the same sintering temperature 1250 ^{o}C or 1350 ^{o}C for higher wt.% of cordierite in the following-up work. Xu et al studied thermal expansion coefficient variation from mixture of rectorite, talc and alumina without additives. The mixture was similar to that used in this work and the TEC at 1350 ^{o}C was around $3x10^{-6}$/K which is in good agreement to our result $3.2x10^{-6}$/K. The minimum TEC (~$1.96x10^{-6}$/K) was found at 1270 ^{o}C [116] and then increase for higher sintering temperatures. In Fig. 4.32, the TEC for sample sintered at 1500 ^{o}C is higher than TEC of sintered at 1350 ^{o}C, thus exhibiting the expected trend discussed above [116].

The reduction of TEC is one of most important factors for successful application. There are also some reports on lowering the TEC by acid/alkali treatment which reduced the TEC from one third to more than half. However, the phase composition of cordierite ceramics is often complex. For instance, from XRD analysis, cordierite ceramics sintered at 1350 ^{o}C and 1250 ^{o}C contain around 55-60 wt. % cordierite along with 15-20 wt. % mullite and α-corundum. Therefore, the TEC is not only function of cordierite but also the combination of other two phases. Interestingly, the thermal properties are also tuneable with chemical treatment for instance, Bai et al [120] showed that a combination of acid and alkali treatment cordierite ceramics will not only reduce the TEC but also enabled maintaining the treatment effect after high temperature application.

The cause for low thermal expansion is summarised by Roy et al in [14]. According to the authors, there is no a single cause for the very low thermal expansion. They identified at least four causes corresponding to different materials such as nano-porous materials i.e. cordierite;

silica-based glasses; ferromagnetic alloys and ferroelectric relaxors [14]. In our study, the cause for cordierite is due to the cordierite has many channels and holes in the structure and the thermal energy is able to be absorbed by the available holes in the structure [14].

4.4.2 Thermal shock resistance (TSR)

Test was carried out according to the ASTM standard C1525-04 [101]. The TSR measurements were conducted to measure the flexural strength retained after thermal shock at elevated temperature. At each soaking temperature, one batch of five samples was rapidly transferred from the furnace to water at Room Temperature (RT) in water tank. After the thermal equilibrium was reached for the sample in water bath, the samples were placed in an oven at 80 ^{o}C for 24 h to constant mass due to likely water adsorption into the porous structure of sample upon quenching. The mean value of retained flexural strength from five samples per batch and standard deviation were calculated.

The flexural strength at RT denoted σ_f, Poisson ratio v, Young's modulus E and linear thermal expansion coefficient were determined experimentally; therefore, we could predict the thermal shock resistance using equation (2.16). The ΔTc was determined to be 167 K. The sample was subject to flexural measurement and the retained strength was studied as function of temperature difference between soaking temperatures and RT as shown in Fig. 4.33.

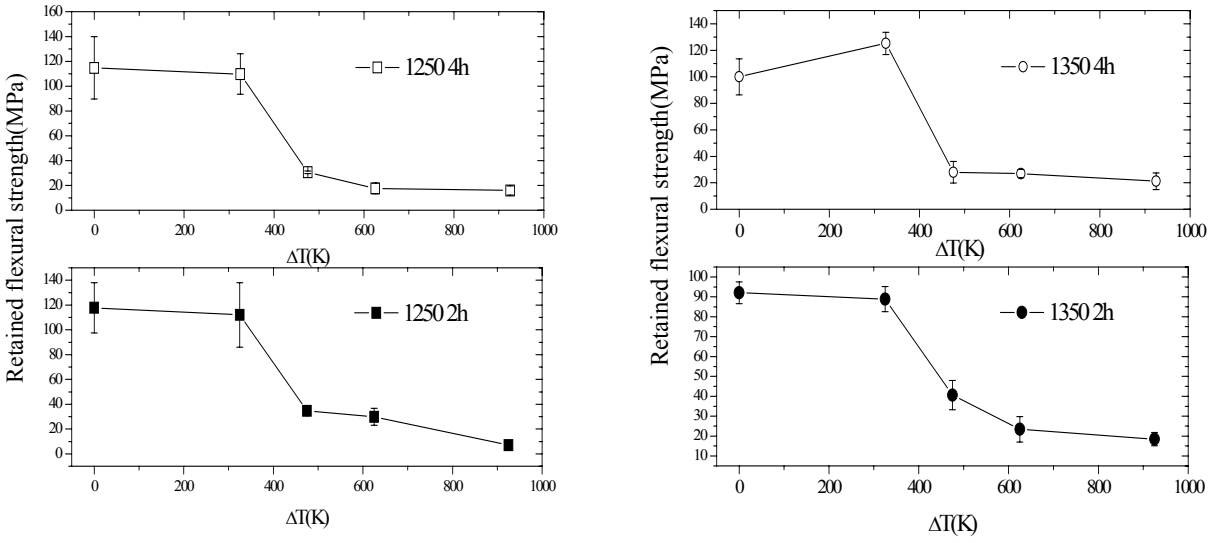

Fig. 4.33: Thermal shock behaviour of bulk ceramics samples with different heat treatments

Fig. 4.33 shows the thermal shock behaviour of bulk ceramics under different heat treatment schedules. Samples sintered at 1250 ^{o}C show relatively higher flexural strength compared to those

sintered at 1350 ^{o}C due to less porosity as discovered earlier. The sudden drop of retained flexural strength was found occurring in ΔT range of 325-625 K. At ΔT=325 K, no samples showed significant decrease of retained strength and a slight increase was even measured for samples sintered at 1350 ^{o}C for 4 h. This is supporting evidence that all samples under all schedules possessing TSR properties better than ΔT=325 K. This result is in good agreement to previous studies conducted by Oliveira et al [15]. Nevertheless, the retained strength dropped to 1/3 or 1/4 of original strength when the sample experienced ΔT=475 K. This is indicative of significant crack growth within dense ceramic bodies. On the other hand, the suggestion to calculate TSR based on equation (2) showed TSR values ranging from 200-230 K, which are significantly lower than the experimental results. This was also explained in Oliveira's work that porous structure of bulk ceramics with around 10% porosity act as energy sink when the crack growth takes place, adsorbing some energy and increasing the crack resistance and hence, the thermal shock induced stress concentration. It is also noteworthy that the retained flexural strength for samples sintered at 1350 ^{o}C for 2 h is the highest retained strength at ΔT=475 K. This is rather expected expectation that the retained strength is higher due to the relative density of the sample or in another word the porosity is higher for 1350 ^{o}C for 2h compared to others with higher relative density.

For industry use, the ceramic foams experience considerable thermal stress under rapid temperature changes, such as in foundry industry when high temperature molten metal flows through the foam to remove non-metallic impurity particles, or the ceramic foam filters are subjected to cooling after metal filtering. Suppliers of some existing products available in the market made of Zirconia or alumina for metal casting do not provide the data on their thermal shock resistances. Nevertheless, ceramic foams made of cordierite have a good potential for thermal shock resistance applications. The TSR property was studied analytically by Gibson and Ashby [121] who proposed an approach to evaluate this property for a cellular structure based on strut's thermal shock resistance property. Then they derived the expression (4.1) for thermal shock behaviour of open-cell dense ceramic foams, denoted as R_b:

$$R_b = R_s \left(\frac{C_2}{C_1} \right) \left(\frac{\rho}{\rho_s} \right)^{-0.5} \quad (4.1)$$

R_s is the thermal shock resistance of dense ceramic struts in the foam, ρ is the apparent density of the foam and ρ_s is the density of ceramic struts. The equation has two empirical coefficients C_2 and C_1, given by Gibson and Ashby for isotropic foam: C_2=0.16, C_1=0.5. For instance, ceramic foams sintered at 1350 ^{o}C for 2 h, considering ΔTc=475 K. Using the above parameters to calculate the thermal shock resistance of the 8 PPI ceramic foam gave R_b=366 K, suggesting that

this temperature difference is sufficient to generate thermal stress and cause damage by extending the cracks. The experimental validation of such TSR property of ceramic foams is under investigation. Fig. 4.34 also illustrates an example of calculated thermal shock resistance of 22 PPI foam sintered at 1250 ^{o}C for 2 h (ΔTc~400 K) based on model of Gibson and Ashby as function of relative density of foam according to (4.1). It is seen that thermal shock resistance decreases rapidly when the relative density increases. However, the fracture strength and Young's modulus increase in opposite way. Therefore, the design of cordierite cellular material is a trade-off between the mechanical and thermal shock resistance properties.

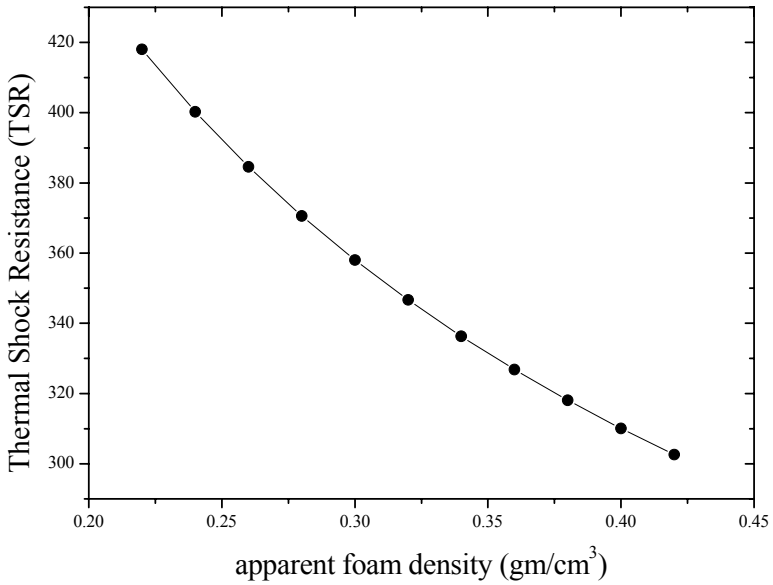

Fig.4.34: Thermal shock behaviour versus relative density

4.5 Microstructural characterization of ceramics foam

4.5.1 Cell cavity volume fraction

The method used to study the volume fraction is very simple and straightforward. It is based on the assumption that the density of the cordierite strut of the foam is the same to bulk ceramics bulk while the density of the cell cavity (containing air = 0.0012g/cm^3) is considered to be zero for simple calculation. Therefore, the fraction of the cell cavity is written in equation (4.2) below:

$$\begin{aligned} &\rho_{dense}c_{dense} + \rho_{cavity}c_{cavity} = \rho_{foam}c_{foam} \approx \rho_{dense}c_{dense} \\ &c_{dense} + c_{cavity} = c_{foam} = 1 \end{aligned} \qquad (4.2)$$

In equation (4.2), the density of the bulk ceramics denoted ρ_{dense} is measured by pcnometer for instance, the bulk ceramics sintered at 1350 ^{o}C for 2h has density of 2.347 g/cm^3; while the density of the ceramics foam denoted ρ_{foam} is measured to be 0.403 g/cm^3. Therefore, equation (4.1) gives the volume fraction of bulk ceramics according to (4.2) and C_{cavity} is determined to be approx 0.8283 for 8 PPI ceramics foam impregnated with suspension modified by 0.5 wt. % CMC. Similarly the cell cavity fraction of 22 PPI is also obtained to be 0.87 with (PS+IS)/PS ratio ~20 at 0.2 wt. % CMC modification. The cavity fraction was not studied for 22 PPI foam impregnated with 0.5 wt. % modified slurry since the foam was not successfully prepared. The study was not conducted towards 30 PPI foam since the microstructure of the polymer replica is not open-cell and actually useless in real application. Fig. 4.35 and Fig. 4.36 demonstrated selective study of the cell cavity for 22 PPI foam with 0.2 wt. % CMC at different (PS+IS)/PS ratio. It is noteworthy that the ceramics cellular structure has rather large discrepancy in cell cavity fraction in the same batch due to the processing control compared to technique of in-situ polymerization making of polyurethane foam. The latter is based on well defined chemical reaction and the cell cavity is homogeneous. In case of impregnation of ceramics slurry to polymer cellular structure, the impregnation is completely hand based. The ceramics slurry is not well controlled to be impregnated on the polymer with exact the same amount of slurry. Therefore Fig. 4.35 or Fig. 4.36 showed an example of controlling microstructure by ratio (PS+IS)/PS. It is considered as only qualitative mean to ceramics slurry processing. This problem has to be tackled by more advanced technique such as developed by Susana et al [122] with prototype of automated machine with multiple stage of pressing the foam to apply slurry weight control after initial impregnation.

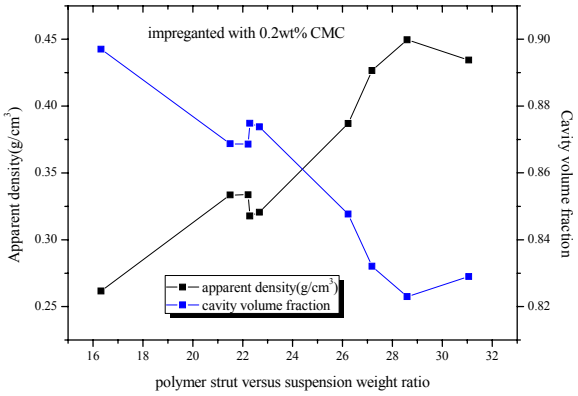

Fig. 4.35 density, cell cavity fractions versus impregnation conditions for 22 PPI foam ;

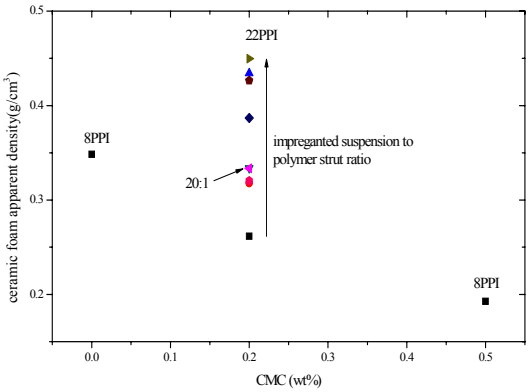

Fig. 4.36 apparent density and cell cavity fractions versus impregnation conditions for 8 PPI and 22 PPI foam.

4.5.2 Computed X-ray tomography study

The instrument used in this investigation is an ultra high-resolution (>2µm) CT system at Institute of National Applied Science (INSA) of University of Lyon II. The machine is manufactured by *PHOENIX|X-RAY* and the general outlook is show in Fig. 4.37. The X-ray source is very powerful up to 240 kV compared conventional X-ray diffraction around 7.8 kV in order to penetrate the sample in great depth to probe inside structure. The instrument is equipped with a powerful workstation with 64 GB memory and multiple processors for image capture, reconstruction of data and Image post-processing. The data is processed and stored in form of stack slices and ready to be analyzed by Image Analysis software such as ImageJ [123] and AMIRA [124].

*Fig. 4.37: The **v|tome|x** ultra high-resolution CT system*

In our work, we studied three ceramics foams with different microstructure scale. We give name to them as 8 PPI, 22 PPI and 30 PPI which originate from their polymer replica structure. However this name does not mean that the ceramics foam may share the same microstructure as to their mother replica since the dip casting and sintering may significantly vary the microstructure depending on the processing conditions. Fig.4.38 (a)-(c) showed the slice images of microstructure for 8 PPI, 22 PPI and 30 PPI ceramic foam respectively.

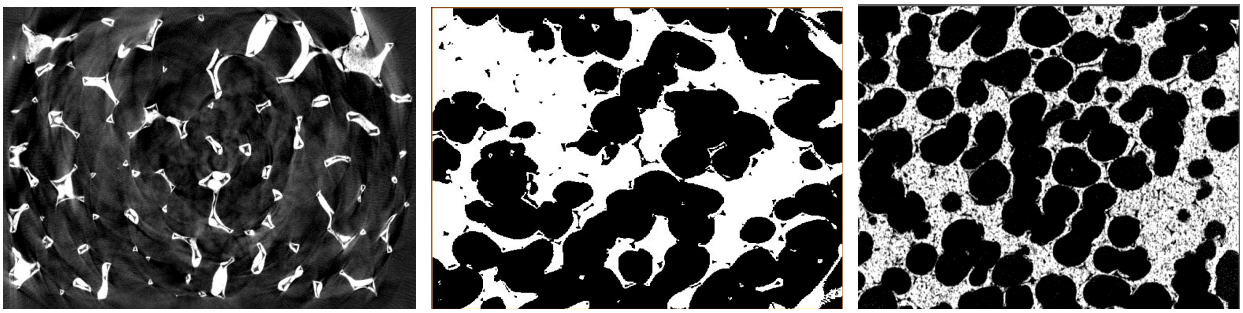

(a) *(b)* *(c)*

Fig. 4.38: slice image of (a) 8 PPI, (b) 22 PPI, and (c) 30 PPI ceramic foam

We notice that the ceramics strut is not fully dense, consisting in a hollow structure with pores across the bulk ceramics body. Big and triangular shaped pores are seen from all samples. The triangular shape pores are formed due to the burning-out of polymer replica during pre-sintering at 600 ^{o}C for 1 h. The polymer burning out is not associated with the fully densified ceramic strut but leaving a hollow structure. This is interesting since the polymer appear to escape from the ceramics suspension coated outside and the behaviour of burning out polymer seem not causing the ceramics strut to collapse at 600 ^{o}C for 1 h. It is also noticed that the hollow structure has shape of triangle.

The 3D structure visualization is not possible for whole structure as scanned due to this computing power limitation. We compromise with cutting the scanned volume into smaller portion around 1/6 of its original size each. The 3D structures are illustrated in perspective view from stack of slices images as shown in Fig. 4.39 to 4.41 for 8 PPI, 22 PPI and 30 PPI foams respectively.

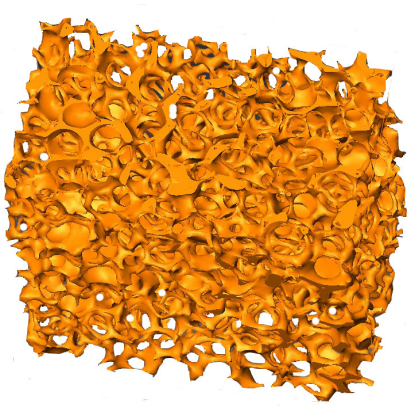

Fig. 4.39: 3D structure of 8 PPI ceramic foam (42 mm x 21 mm x 19 mm)

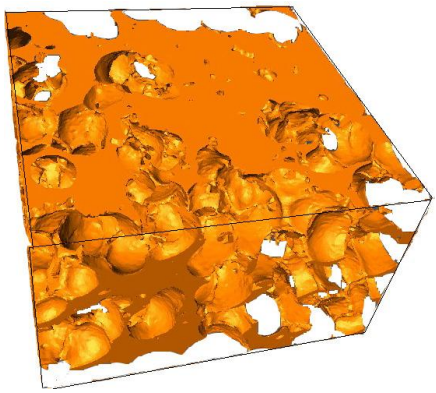

Fig. 4.40: 3D structure of 22 PPI ceramic foam (14 mm x 13 mm x 8 mm)

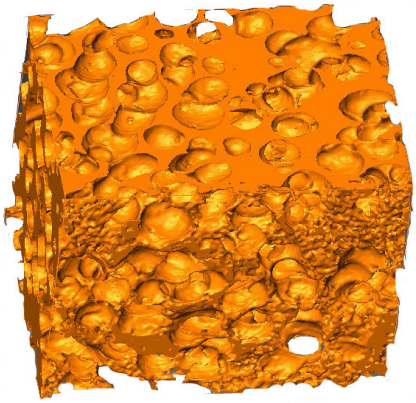

Fig. 4.41: 3D structure of 30 PPI ceramic foam (9.32 mm x 6.24 mm x 4.5 mm)

The 3D structure for foams of different microstructure scale shows very distinct features in terms of porosity and cellular structures. 8 PPI foam appear to be completely open cell structure with pores interconnected with big windows and most struct materials are concentrated on edges. However, the microstructure of 22 PPI, in particular 30 PPI foam showed very poor open cell structure without interconnection. In addition to this, 22 PPI foam appears to be very bulky with some pores not only closed but completely filled. 30 PPI foam appeared to be uniformly coated with ceramic slurry and the materials are distributed not only on edges but also on cell walls. The structure of closed cell is not desirable for ceramics filter or catalyst applications. The reason of seeing good open cell structure for the 8 PPI foam and closed cell or bulky foam with 22 PPI and 30 PPI foam are two-fold. First of all, the rheological properties are critical for the impregnation of polymer foam with the slurry. When slurry viscosity was too low, the slurry could not stay on the surface and settled to the bottom. However, when viscosity was too high the slurry not only

covered the surface of the polymer struts but also blocked the windows between pores and the cell became closed structure or completely filled. The 3D structure of the ceramics foam of 22 PPI showed that the rheological properties of suspension with 0.5 wt. % CMC were suitable to impregnate the 8 PPI foam but very poor for impregnating the 22 PPI foam. The aforementioned 8 PPI foam was selected and further treated in AMIRA software to render smaller scale 3D structure in Fig. 4.42 for generating grids to perform FEA calculation in order to study the mechanical properties as illustrated in Fig. 4.43.

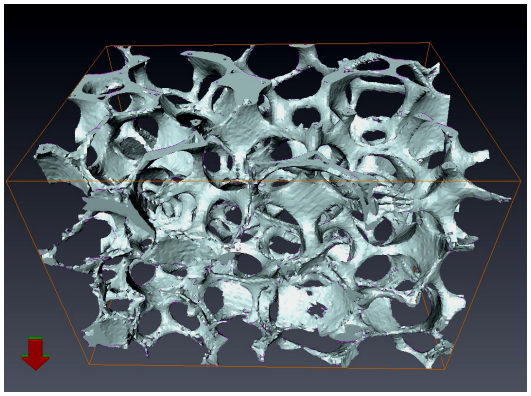

Figure 4.42: Partial structure of 8 PPI ceramics foam

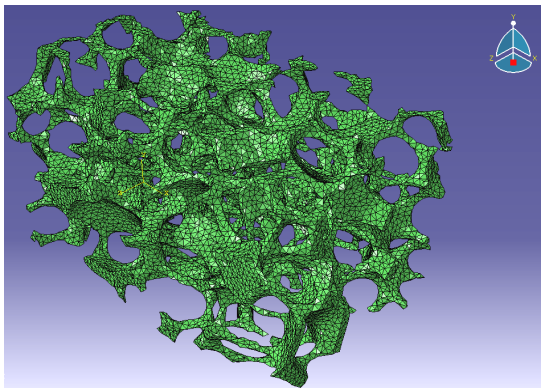

Figure 4.43: grids for FEA modelling 8 PPI foam (16.8 mm x 10.5 mm x 9.8 mm)

It is worthy noting that although the grid generation was successful, the memory required for calculation was out of range of the current computing resources after testing. Therefore, the calculation was actually done for a structure even smaller than that shown in Fig. 4.43. However, a request is being made to some collaborator in order to perform such calculation using a higher spec PC.

4.6 Mechanical characterization

4.6.1 Impulse Excitation

The measurement of dynamic modulus was carried out at National Laboratory of Energy and Geology (LNEG). The equipment is called Resonant Frequency& Damping Analyser (RFDA) and the manufacturer is IMCE (Belgium). The measurement follows ASTM standard (ASTM E1876) and the sample is prepared with large aspect ratio to simplify the calculation of Young's modulus according to ASTM E1876. A precaution should be given in measuring small length due to the screw calibre in the equipment could not locate the node at 0.224 L from the ends if the length of sample is less than 32 mm. The typical setup of IE experiment for bulk ceramics and

foam are shown in Fig. 4.44 and Fig. 4.45 respectively.

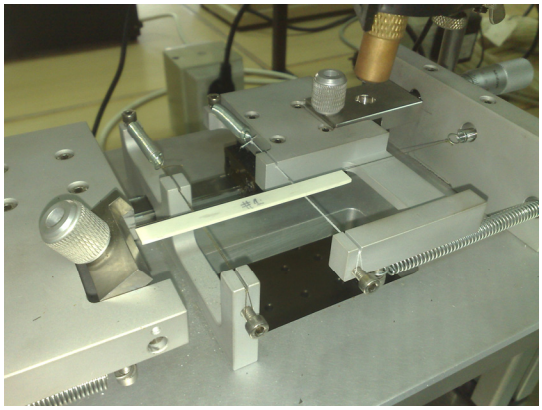

Fig.4.44: set-up for ceramics bulk

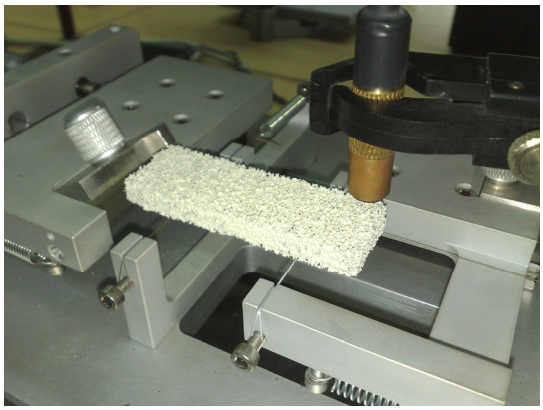

Fig.4.45: set-up for ceramics foam

The RFDA is also provided with software which read and analyzes the input sound signal from the tapping. The signal's waveform is shown on the screen and the Fourier transform is performed simultaneously. The calculation of Young's modulus is carried out at the same time and displayed on the screen. It should be mentioned that the software also allow analysis of Shear modulus by applying torsion tapping force from which the Poisson ratio is possible to be determined experimentally with relationship between Young's modulus and shear modulus. The result of Young's modulus, shear modulus and Poisson ratio for the bulk cordierite-mullite-alumina system and foam are listed in Table 4.7.

Table 4.7: Young's modulus of dense and foam ceramics from IE measurement

Measurement parameters	1350 ^{o}C 2 h dense	1250 ^{o}C 2 h dense	1350 ^{o}C 2 h 8PPI	1250 ^{o}C 2 h 22 PPI
Width (mm)	7.45	6.82	30.90	27.53
Thickness (mm)	1.58	1.45	16.47	9.425
Length (mm)	53.16	49.53	130.13	80.7
Weight (g)	1.442	1.164	40.22	10.933
Flexural Freq (Hz)	3707	3815	1204	2036
Damping factor	0.000498	0.000566	0.007339	0.012698
Young's Modulus (GPa)	96.63	94.29	0.97	1.08
Poisson ratio (υ)	0.267	*0.267	0.004	0.014
Shear Modulus (GPa)	38.13	-	n/a	0.54

*: the Poisson ratio is considered to be the same

The modulus measured from the IE technique show advantages that the sample is not

destructive and the Young's modulus has also been studied by compression method at the similar conditions sintered at 1350 ^{o}C for 4 h. And the modulus shows much lower value of ~500 MPa [125]. The modulus measured by IE technique is around 1.08 GPa is twice higher than bulk ceramics. This exotic result of disagreement is not surprised since the difficulty in machining the ceramics specimen with an even flat surface and the machine pressing plate has also flatness problem. The likely reason for this is discussed that static compression could hardly avoid the problem of brittleness of the ceramics specimen that the sample will crack first before elastically deformed.

4.6.2 Flexural strength

The flexural strengths of ceramics composite of cordierite and other phases are measured with three point bending method. Due to structural defect and cavity in ceramics sample, at least 5 specimens from the same batch conditions were tested as shown in Table 4.9. Due to the specimens were prepared via Slip casting route. The specimens have different dimensions due to hand grinding of green body. After the sintering, the sintered ceramics were checked and it was discovered that the sintered ceramics do not have good parallelism of surface. Therefore further grinding and polishing are necessary to improve the uniformity of the sample size. The mean value from 5 measurements are taken average and compared to other samples.

The ceramics specimens prepared at variable temperature and time were also tested by flexural strength measurement. The results are illustrated in Fig. 4.46. First of all, we note that the specimen at 1500 ^{o}C, the sample of monolithic mullite does not show highest flexural strength as indicated by Table 1.1. It is because of the large cavity present in the body due to liquid phase formation. On the other hand, the ceramics decreases in flexural strength as the sintering temperature decreases. The sample prepared at lower temperature (1250 ^{o}C) showed higher strength around 100-120 MPa. From this trend, we proposed that the optimal sintering temperature is 1250 ^{o}C without pores or crack. This is somehow proved in relative density measurement for bulk ceramics that sample sintered at 1250 ^{o}C has highest relative density of 96-98%. Meanwhile, the longer sintering time appeared to affect the mechanical properties.

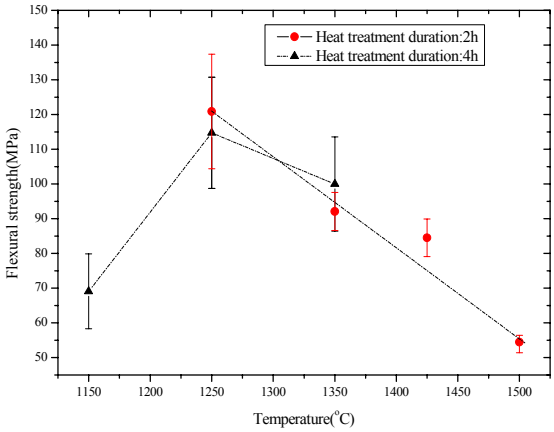

Fig. 4.46: flexural strength at different heating temperature

4.6.3 Compression strength of bulk

The Compression strength is also an important property of the ceramic cellular structure used in refractory application. The property is measured by compression and the speed of cross head is 0.2 mm/min. Since the elastic regime of the ceramics foam is very small compared to metal or polymer and the compressed surface generally present a significant roughness. Therefore a layer of softer material called compliance layer made of rubber between the cross head and ceramics foam upper surface must be used to the rough surface of the ceramics foam in order to apply force in more evenly manner. The layers of polymer compliance are applied at both the bottom surface and upper surface.

The strength of cellular structure of cordierite is studied first of all for the slip cast green body which is an indication of the strength for handling and cutting of the green body shape. The stress-strain curve is presented in Fig. 4.47. The green body shows a linear deformation with multiple yield events due to crack occurrences. However, the first yield event was due to falling-off piece from green body and the second yield event was related to the crack occurred across the body and hence the Compression strength is determined until the second crack appeared. After the appearance of the second crack, the specimen was still in place but completely cracked. Therefore, the Compression strength is defined where the first crack showed up at ~0.15 strain as 4.17 MPa.

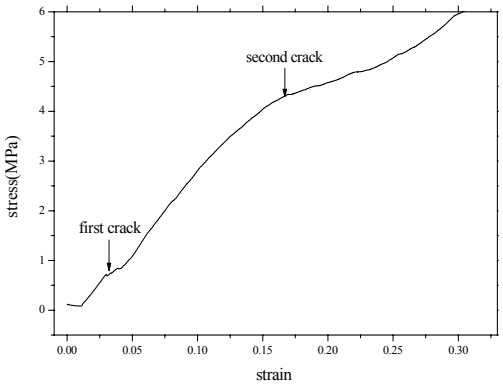

Fig. 4.47: stress-strain curve for slip cast green body

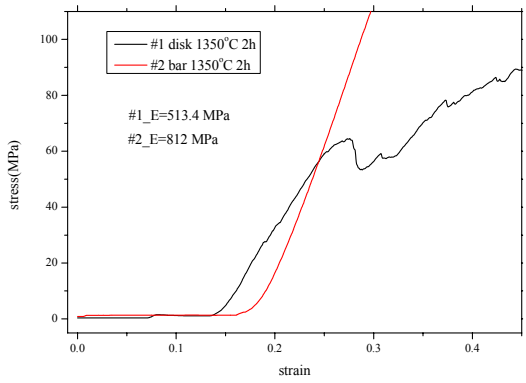

Fig. 4.48: Elastic property of bulk ceramics under compression

The study of Compression strength is important for dense and cellular ceramic samples. However, the Compression strength of bulk ceramics is not presented due to lack of experimental bench that operate with adequate compressive force. Fig. 4.48 shows an example of compression measurement in which the stress-strain curve shows behaviour of multi-crack events with low Young's modulus compared to those from IE measurement. These facts demonstrate that compression measurement of dense sample could cause significant error and risk to damage the load cell with maximum force (10,000N) with big force applied (~80% of maximum force), therefore the measurements for bulk ceramics was abandoned.

4.6.4 Effective modulus and strength of foam

The stress-strain curves are presented in Fig. 4.49 and the linear portion of deformation is used for Young's modulus. It is noteworthy that the foam has extremely low modulus compared to IE measurement. The results regarding the Young's modulus from compression tests are totally untrustworthy. The Compression strength was determined for a point at which the foam disintegrated with a sudden structural failure as illustrated in Fig. 4.50 and Fig. 4.51. Because of the problem encountered in validating the effective modulus by compression tests, therefore, the reliability of Compression strength is in doubt and subject to further analysis by modelling. Also in Fig. 4.49, the relative density of each ceramics foam are varied a lot from one to another due to impregnation was carried out at different conditions such as concentration of CMC polymer. The microstructure of 22 PPI and 30 PPI impregnated with highly viscous slurry was almost closed cell whilst 8 PPI was homogeneous open cell structure. Therefore the modulus was seen increased from 8 PPI to 30 PPI. Likewise, the compression strength was also increased with decreasing pore size of microstructure.

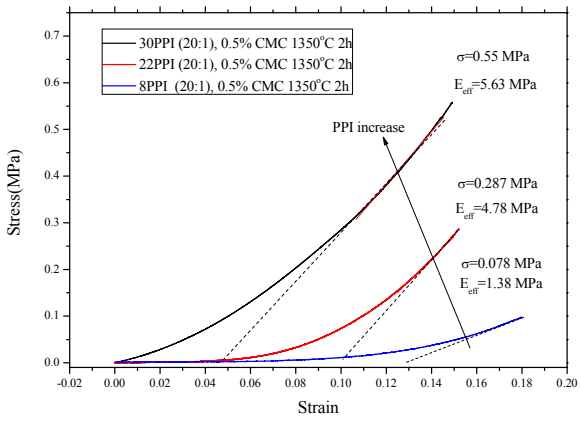

Fig. 4.49: example of stress-strain curve of 3 ceramics foams

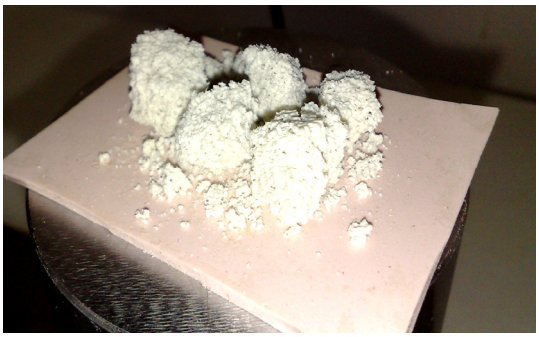

Fig. 4.50: crush of a 30 PPI ceramic foam

Fig. 4.51: crush of a 8 PPI ceramic foam

The abovementioned results suggested that characterising ceramic foam materials under compression is very difficult due to its surface roughness and brittleness. The IE technique could effectively solve the problem of Young's modulus, but does no enable to measure the strength of foam. In addition, the compliant layer made of rubber is completely destroyed since the fractured ceramics are very hard with sharp corners. Due to brittleness of ceramics, the structural failure was too sudden to be accurately detected by the cross head force sensor. The cross head continues to compress with increasing force and can hit the bottom plate and damage the machine. As consequence, further Compression strength measurements were suspended.

4.7 Dielectric properties

The dielectric properties were measured with LCR (Inductance-Capacity-Resistance) meter from 1000 Hz to 1 MHz. The experimental apparatus includes a ceramics tube (alumina) as show in Fig. 4.52 and the sample with the upper and lower surfaces partially coated with a

gold layer as electrodes, as demonstrated in Fig. 4.53, was placed in the middle of the tube.

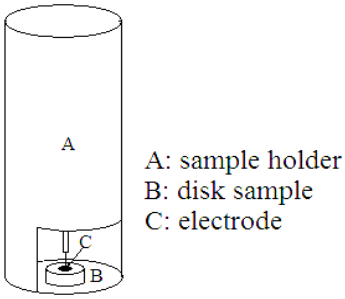

Fig. 4.52: Setup of dielectric measurement

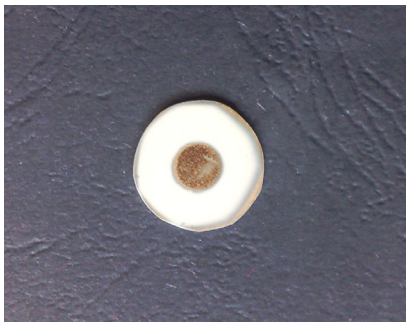

Fig. 4.53: disk with Au electrode, ϕ=5.6 mm

The measurement of dielectric properties was performed at room temperature for 6 samples of different sintering schedules and also at elevated temperature up to 600°C for a sample selected on the basis of maximum flexural strength. No previous literature has ever reported on the effect of temperature on dielectric properties of cordierite ceramics and the ceramics have to work at elevated temperature environments. Therefore, it is desirable to study the dependence of dielectric constant on temperature variations. In this regard, sample batch with optimum mechanical strength was chosen (1250 °C, 2 h) to test while the others are under investigation and will not be reported in the thesis.

The measurement of dielectric properties are based on measurement of capacitance of the ceramics capacitor deposited with Au electrode on the both surfaces. The area of the capacitance is the area of the deposited Au electrode and the thickness of the dielectric material is the thickness of the ceramics capacitor as given in the Table 4.8 below.

Table 4.8: sample specification and heat treatment conditions

Heat treatment	Sample thickness (mm)
1250 °C, 2 h	1.09 mm
1250 °C, 4 h	1.26 mm
1250 °C, 8 h	0.69 mm
1350 °C, 2 h	1.68 mm
1350 °C, 4 h	1.26 mm
1350 °C, 8 h	0.78 mm

The typical equation for parallel plate and circular cross section sample is given as:

$$\varepsilon_r = \frac{Cd}{\varepsilon_0 \pi r^2} \qquad (4.3)$$

Where the thickness d was taken into account in equation (4.3) and the capacitance C in measured in pF by LCR, r is the radius of Au electrode of 5.6 mm, ε_0 is dielectric permittivity of vacuum (8.85×10^{-12} F/m). Therefore the relative dielectric constant of ceramics is calculated. On the other hand, the dielectric loss factor is obtained from the ratio of the imaginary part of complex resistance ε'' to the real part ε'=ε_r. The loss factor is expressed by the following equation:

$$\tan\delta = \varepsilon'' / \varepsilon' \quad (4.4)$$

Where ε'' is obtained from ε''=ωRC, and the ω is the measuring frequency from 1000 Hz to 1 MHz. The dielectric loss factor is an important measure of quality to the sample and electrode. Typically, tanδ < 0.02 is considered very good for application.

Fig. 4.54 shows the dielectric constant as function of the frequency from 1000 Hz to 1 MHz at room temperature. The minimum dielectric constant of ceramics is around 6 at 1 MHz. The result shows that the dielectric constant is slightly larger than monolithic phase of cordierite and equal to that of monolithic phase of mullite in Table 1.1.

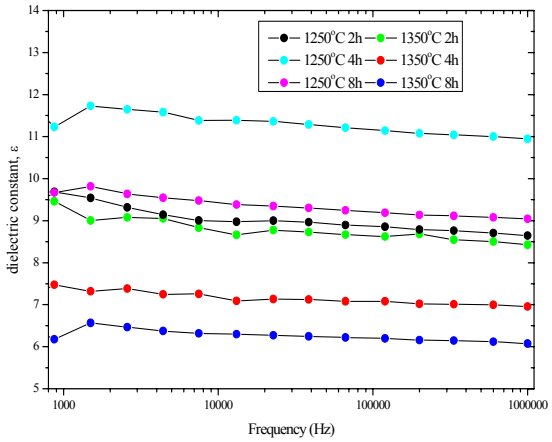

Fig. 4.54: dielectric constant, versus frequency at RT;

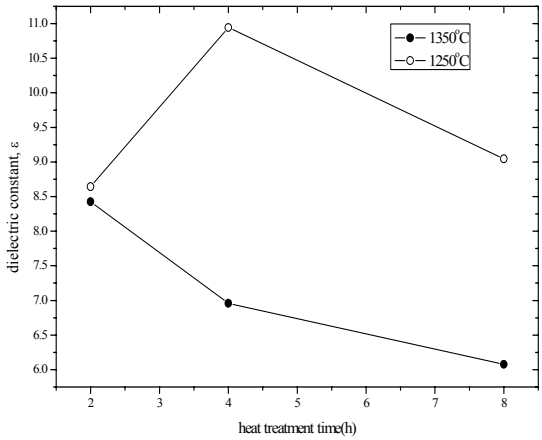

Fig. 4.55: sintering time dependent dielectric constant at 1 MHz

The dielectric constant appeared to be constant over the whole range of frequency for all samples. This suggests that the no induced weakening or disappearance of ionic polarization takes place due to increase frequency [11]. The dielectric constants for all samples at 1 MHz are plotted in Fig. 4.55 and the values are in agreement with previous results [11, 126]. However, there are significant differences of dielectric constant between the samples prepared under different conditions. The dielectric constant shows not only sintering temperature

dependence but also sintering time dependence in a rather systematic way. With increasing sintering time at 1350 ^{o}C, the dielectric constant at 1 MHz decreases from 8.5 to 6.0; however, the sample sintering at 1250 ^{o}C for various times shows a non linear behaviour. The dielectric constant starts from 8.5 and increases to around 11 and then decreases again to around 9 as function of sintering time. The complexity of dielectric properties for ceramics materials has been addressed and is dependent on many factor such as content of crystalline phase, glass phase, porosity and so on [127]. The larger dielectric constant is supposed to be due to larger value of mullite phase and alumina phase which will increase the composite dielectric constant based on wt. % fraction of ingredient phases from XRD. On the other hand, the SEM studies revealed approx 10% porosity in the 1350^{o}C for 2 h specimen which should reduce the dielectric constant. However, our observation shows opposite trend to dielectric constant than prediction.

The dielectric loss tangent is the imaginary part of complex number and the real part is dielectric constant as we see previously. The imaginary part is called loss factor and represented by loss tangent (ratio between loss factors to dielectric constant). The loss tangent is an important parameter since the electric energy will be dissipated into heat and this has implication of how much the materials will convert the EM to heat. Since the loss tangent is also a parameter to evaluate the microwave-materials coupling capability. The bigger loss tangent the better material-microwave coupling capability is, and vice versa. Fig. 4.56 illustrates the variation of dielectric loss factor for all samples over 1000 and 1 MHz range. The curves demonstrate that the dielectric loss is relative small and consistent with literatures. The lowest dielectric loss is well below 0.02 for samples sintered at 1250 ^{o}C for 8 h followed by 1250 ^{o}C for 2 h. In the meantime, the dielectric loss at 1 MHz showed systematic behaviour the dielectric losses from samples sintered at 1350 ^{o}C are all higher than those prepared at 1250 ^{o}C; Fig. 4.57 is dedicated to illustrate the variation of dielectric loss of all samples at 1 MHz. It appears that the longer sintering time tends to decrease dielectric loss factor at given temperature. Therefore, the lowest dielectric loss factor is also seen from the sample sintered at 1250 ^{o}C for 8 h at 1 MHz.

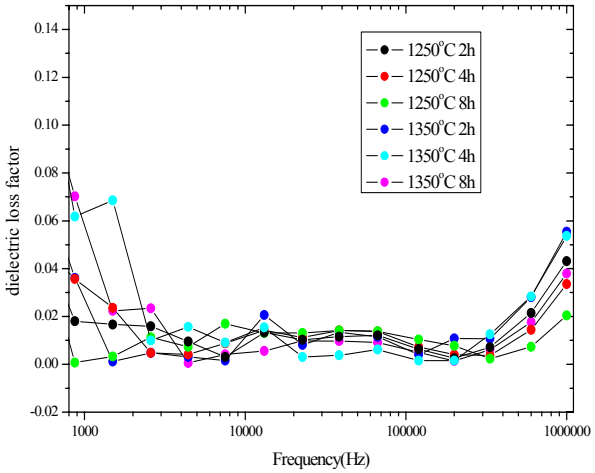

Fig. 4.56: tanδ versus frequency at RT;

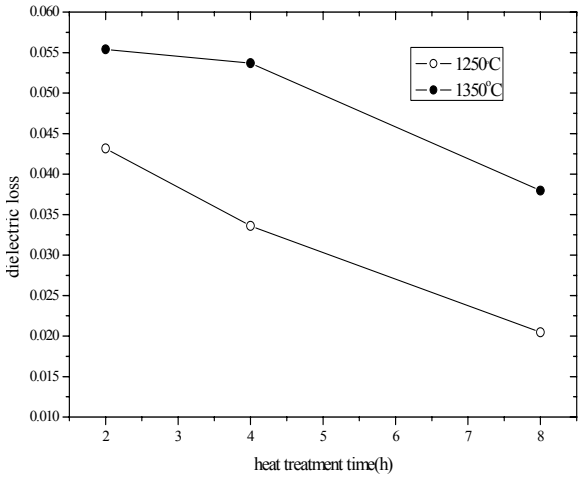

Fig. 4.57: dielectric loss at 1MHz

The temperature dependent dielectric constant is shown in Fig. 4.58 from 1000 Hz to 1 MHz between RT and 600°C. The measurement was very time consuming and took 24 h to be accomplished with small temperature steps. Therefore, we selected the sample sintered at 1250 °C for 2 h to study. The measurement showed a clear trend of decreasing dielectric constant with increasing frequency at high temperature range while no significant differences could be observed for all frequencies approximately below 200 °C. It is also noticed that the lower frequency the steeper is the increase of dielectric constant above 200°C. On the other side, the dielectric constant at RF range of 1 MHz showed a flat dielectric constant around 10 across the temperature from RT to 600°C. The sharp increase of dielectric constant for 1000 Hz to 1 MHz is followed by a radical drop at around 600°C. In order to determine more precisely the temperature of Curie point, a close lookup of temperature dependent dielectric constant between 520 °C to 600 °C is illustrated in Fig. 4.59, indicating that all the dielectric constant drops radically at 590 °C.

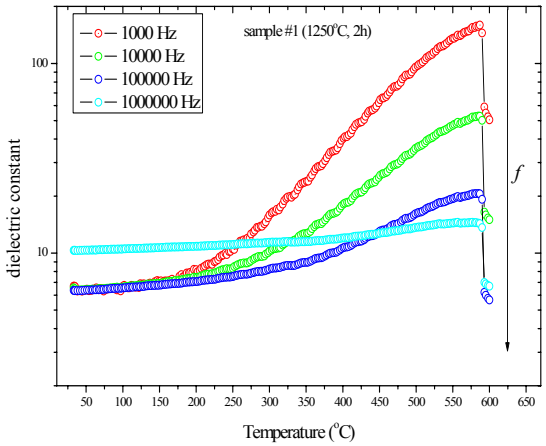

Fig. 4.58: Temperature dependent dielectric constant of sample #1(1250 °C, 2 h)

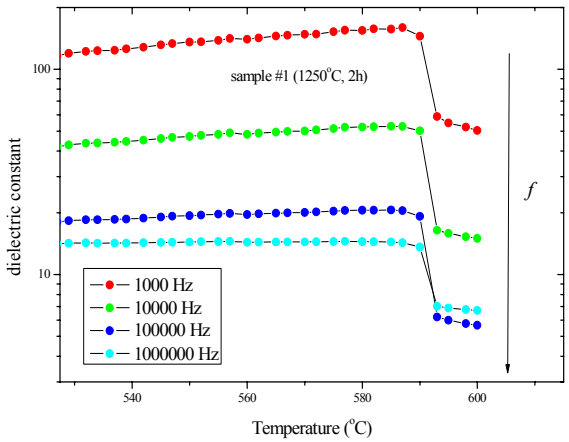

Fig. 4.59: Search for temperature to de-functionalize the ceramics

As previous mentioned, that the ceramics capacitor will experience such as aging after long time use due to decrease of dielectric constants. The most common approach to restore the ceramics capacitor or de-aging to increase the dielectric constant is based on the heat treatment above the Curie temperature. However, we discovered the opposite trend in composite ceramics of cordierite. The dielectric constant of sample sintered at 1250 °C, 2 h showed dramatic decrease at 590 °C. Further check was made after experiment with multimeter and the cause was identified as the Au electrode has been completely evaporated above 590 °C. This is rather surprisingly to us since it may imply that the dielectric constant is constant over large temperature change until the electrode material is failed. The reason of such property in case of low dielectric material is extremely interesting however yet undiscovered. More careful investigation is under way to confirm the effectiveness of heat treatment on reducing the dielectric constant and effect on other properties such as mechanical and so on to validate its application in real industry.

The following Fig. 4.60 shows the dielectric loss of the sample sintered at 1250 °C for 2 h as a function of temperature. It is apparent that the ceramics has stable dielectric loss resistance at 1 MHz over a wide range of temperature from RT to 600°C. The dielectric loss has strong dispersion behaviour below 1 MHz. However, as previously discussed, for good electronic application the dielectric loss factor has to be smaller than 0.02 and the sample demonstrated dielectric loss factor not more than 0.05 until 400 °C which promises very good temperature stability.

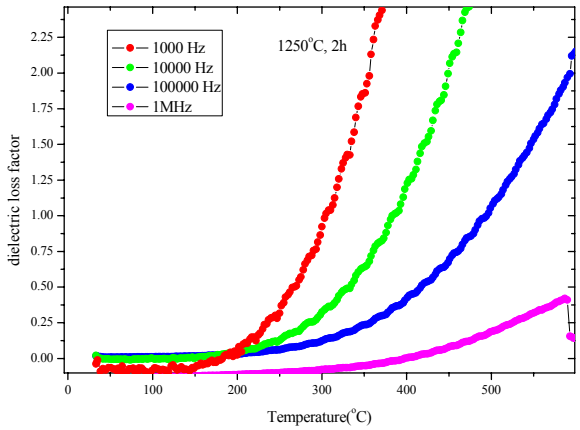

Fig. 4.60: temperature dependent dielectric loss factor (1250 °C, 2 h)

The dielectric properties are closely linked to the microstructure. For instance, porous structure is favoured since air has lowest ε~1.00005 and the presence of pores could decrease the ε lower than 2. However, the porous structure is also responsible for the low mechanical strength. There has been few cases of commercial grade Cordierite ceramics that has application in electric isolator material and marketed in the by CeramTec North America, USA. Table 4.9 list the company's product versus the cordierite composite ceramics obtained in this study. It is interesting to find out that the sample from our work has comparable dielectric properties and even superior properties.

Table 4.9: dielectric properties, mechanical and thermal properties of commercial cordierite benchmark to samples in the study
(Data source: http://www.ceramtec.com/index/materials/oxide_ceramics/silicate_ceramics)

Commercial code	dielectric constant (1 MHz)	dielectric loss	Flexural strength (MPa)	Thermal expansion coeff (20-1000 °C),10^{-6}/K	Company
Cordierite-447	4	0.048	23.4	1.7	CeramTec North America, USA
Cordierite-701	5.3	0.025	103	3.2	
Cordierite-sikor	5	0.007	n/a	2.2	
Cordierite composite	6-10	0.04-0.06	90-120	3.2-4	This work

However the need of improving other properties of low-dielectric materials such as high dielectric strength（breakdown voltage>4MV/cm), high thermal stability>450 °C, and good

adhesion strength and so on [128] is also necessary. It is not easy to acquire materials satisfying all abovementioned conditions. Composite cordierite prepared from this non-standard composition has shown many technical aspects to match some of the requirements in terms of thermal stability, shock resistance, low-ε, low dielectric loss at RT and higher temperature as well as high modulus and mechanical strength and therefore become a potential candidate to future IC industry.

Chapter 5: FEA modeling of cellular ceramics

Micromechanical theory of heterogeneous materials has been developed to address the mechanical property of one material embedded in another. The theory was originally developed by Eshelby [129] who gave the expression of tensor depending on Poisson ratio of the embedded phase regardless of dimension in case of spherical inclusion of embedded particles or objects. The Eshelby theory was further developed by Mori and Tanaka who use Eshelby tensor to calculate the effective stiffness of heterogeneous material. Eshelby tensor was constructed as a Fourth-order tensor relating average inclusion's strain to average matrix strain and could also be modified with inclusion's orientation in case of non-random distribution [130]. MT method was found very successful in simulating elastic property of open-cell Polyurethane foam with carbon nanotubes reinforcement under effective dispersing conditions in [33]. However, no literature has been ever found using MT method to ceramic foams. Therefore, the MT micromechanical model for cellular materials and its application to the ceramic foams is discussed in this chapter. The modelling result was compared the experiment results and a poor agreement was found unfortunately. In addition, a new technique was used to simulate the mechanical behaviour by Finite Element Analysis based on actual 3D structure from X-ray tomography. The advantages and drawbacks from each approach will be discussed and reviewed.

5.1 Problems' Review

According to Christensen [131], General Self Consistent Model (GSCM) with assumption of spherical cavity in a cellular material gives the most physically realistic results when the cavity volume fraction approaches 1. The effective Young's modulus is given in [131]:

$$\frac{E_{eff}}{E_m} = \frac{2}{5+3\nu_m}(1-c_2) \quad (5.1)$$

Where E_{eff} denotes as effective modulus of the cellular material and E_m, ν_m are the modulus and Poisson ratio of strut material. In all calculations shown later on, subscripts 1 and 2 refer to strut material and the cell cavity respectively. Therefore c_1 and c_2 are the struts and cell cavity fractions, respectively. Here, the cell cavity fraction used in modelling is obtained from density method as introduced in Chapter 4.

The Poisson ratio and bulk's Young's modulus are v=0.267 and E_m=99 GPa for instance when sample is sintered at 1250 ^oC for 2 h from Impulse Excitation experiments. The effective

Young's modulus for ceramics foam from (5.1) was calculated by taking into account of the foam's cavity fraction for 8 PPI and 22 PPI as shown in Table 5.1.

Table 5.1: effective Young's modulus from Christensen model

Samples	8 PPI (1350 ^{o}C, 2 h)	22 PPI (1250 ^{o}C, 2 h)
Dense modulus (GPa)	96	99
Dense Poisson ratio	0.267	0.267
Cavity fraction (%)	0.8283	0.87
Calculated Effective modulus (GPa)-GSCM	4.52	4.43
Experimental modulus (GPa)	0.97	1.08

The E_{eff} is compared to Impulse Excitation (IE) measurement. The results from IE experiment are around 1 GPa and 5 times or 4 times lower respectively for 8 PPI and 22 PPI foams than those predicted by Christensen model. This study indicates a lack of exact match for Young modulus. However, surprisingly good results were obtained, since such a simple calculation could predict the effective mechanical properties for cellular ceramics. Nevertheless, we also noticed a trend that when cavity fraction approaches 1, the agreement between the calculated effective modulus and experimental modulus is improved which is consistent to the suggestion made by Christensen.

5.2 Modeling with Mori-Tanaka Approach

In order to examine the modelling ability of other method, the modelling was carried out with approach developed by Mori & Tanaka in 1970's [132] and re-developed in 1980's [133]. This method gives the general expression of effective stiffness of two heterogeneous materials with stiffness tensor C^{1}_{ijkl} and C^{2}_{ijkl}, the two materials occupy a volume fraction of c_1 and c_2 respectively. Before the emergence of X-ray tomography and finite element analysis based on actual 3D structure, MT method was the most effective approach to study mechanical property of composite material with great success.

One of the advantages of micromechanical method is to consider the material properties without request empirical parameters from experiments prior to the calculation. The general expression of effective stiffness tensor of composite materials consisting of two homogeneous phase 1 and 2 is shown below [130]:

$$C_{ijkl}^{eff} = C_{ijkl}^{1} + c_2\left\{\left(C_{ijpq}^{2} - C_{ijpq}^{1}\right)T_{pqmn}\right\}\left[c_1 I_{mnkl} + c_2\left\{T_{mnkl}\right\}\right]^{-1} \qquad (5.2)$$

Where I_{mnkl} is the identity tensor, the contents of 4th order identity tensor is given by Kronecker's symbol [130]. When dealing with cellular structure materials, the simple approach is to equate stiffness tensor C^2_{ijpq} in (5.2) to zero since phase 2 now is treated as cell cavity. Also the term in (5.2) $T_{mnkl} = \left[I_{mnkl} - S_{mnkl}\right]^{-1}$ is given only in case when $C^2_{ijpq}=0$. Therefore a modified expression of effective stiffness tensor of cellular materials with cavity volume fraction c_2 is obtained:

$$C_{ijkl}^{eff} = C_{ijkl}^{1} - c_2 C_{ijst}^{1}\left[I_{stpq} - S_{stpq}\right]^{-1}\left[c_1 I_{pqmn} + c_2\left[I_{pqmn} - S_{pqmn}\right]^{-1}\right]^{-1} \qquad (5.3)$$

In addition, the General expression of stiffness tensor C^1_{ijkl} of dense matrix of isotropic materials is given as [130]:

$$C_{ij} = \begin{bmatrix} C_{11} & C_{12} & C_{12} & 0 & 0 & 0 \\ C_{12} & C_{11} & C_{12} & 0 & 0 & 0 \\ C_{12} & C_{12} & C_{11} & 0 & 0 & 0 \\ 0 & 0 & 0 & C_{44} & 0 & 0 \\ 0 & 0 & 0 & 0 & C_{44} & 0 \\ 0 & 0 & 0 & 0 & 0 & C_{44} \end{bmatrix} \qquad (5.4)$$

The stiffness matrix component system is also given as [130]:

$$C_{11} = \frac{E}{1+v}\frac{1-v}{1-2v}, C_{12} = \frac{E}{1+v}\frac{v}{1-2v}, C_{44} = \frac{E}{2(1+v)} = \mu \qquad (5.5)$$

And then taking into account material property parameters, for instance E=99 GPa and v=0.267 for bulk ceramics sintered at 1250 ^{o}C for 2 h, therefore we can determine the stiffness matrix of ceramics foam with cavity shown in (5.6). Then substituting the cell volume fraction found previously into (5.3), for instance, C_2=0.8283, therefore we have effective stiffness as demonstrated in (5.7):

$$C^{1}_{ij} = \begin{bmatrix} 122.91 & 44.76 & 44.76 & 0 & 0 & 0 \\ 44.76 & 122.91 & 44.76 & 0 & 0 & 0 \\ 44.76 & 44.76 & 122.91 & 0 & 0 & 0 \\ 0 & 0 & 0 & 39.07 & 0 & 0 \\ 0 & 0 & 0 & 0 & 39.07 & 0 \\ 0 & 0 & 0 & 0 & 0 & 39.07 \end{bmatrix} \quad (5.6) \qquad C^{eff}_{ij} = \begin{bmatrix} 16.81 & 6.12 & 6.12 & 0 & 0 & 0 \\ 6.12 & 16.81 & 6.12 & 0 & 0 & 0 \\ 6.12 & 6.12 & 16.81 & 0 & 0 & 0 \\ 0 & 0 & 0 & 5.34 & 0 & 0 \\ 0 & 0 & 0 & 0 & 5.34 & 0 \\ 0 & 0 & 0 & 0 & 0 & 5.34 \end{bmatrix} \quad (5.7)$$

The stiffness tensor of the ceramic foam was then transformed to the compliance tensor by inverse operation demonstrated in (5.8):

$$M_{ij}^{eff} = [C_{ij}^{eff}]^{-1} = \begin{bmatrix} S_{11} & S_{12} & S_{12} & 0 & 0 & 0 \\ S_{12} & S_{11} & S_{12} & 0 & 0 & 0 \\ S_{12} & S_{12} & S_{11} & 0 & 0 & 0 \\ 0 & 0 & 0 & 2(S_{11}-S_{12}) & 0 & 0 \\ 0 & 0 & 0 & 0 & 2(S_{11}-S_{12}) & 0 \\ 0 & 0 & 0 & 0 & 0 & 2(S_{11}-S_{12}) \end{bmatrix} \quad (5.8)$$

where the Elastic modulus and Poisson ratio can be determined from the components of compliance tensor as given in [130]:

$$S_{11} = \frac{1}{E}; S_{12} = -\frac{v}{E}; \quad (5.9), \quad 2(S_{11}-S_{12}) = \frac{2(1+v)}{E} = \frac{1}{\mu} \quad (5.10)$$

From above discussion, the effective stiffness tensor is ready to be calculated only if we know the tensor contents of S_{pqmn} in equation (5.3). The S_{pqmn} is known as "Eshelby tensor" which is a function of the bulk ceramics properties as well as shape of the embedded inclusion. In this investigation the embedded materials are cell cavity and considered to be sphere. The mechanical properties with cellular structure of foam has also to be based on assumption that the ceramics strut is fully dense without crack and the mechanical strength is uniform across the whole body struts. However Computed X-ray studies revealed that this is not the case and the ceramics struts present a triangular hollow structure which is not be able to quantify by any optical or physical method since its closed structure. Nevertheless, under such assumption the corresponding components of Eshelby tensor for ceramic foam with spherical cavity is found by Schjødt-Thomsen et al [130]. First of all, Eshelby tensor in general form is shown in (5.10) [129].

$$S_{ijkl} = \begin{bmatrix} S_{1111} & S_{1122} & S_{1133} & S_{1123} & S_{1113} & S_{1112} \\ S_{2211} & S_{2222} & S_{2233} & S_{2223} & S_{2213} & S_{2212} \\ S_{3311} & S_{3322} & S_{3333} & S_{3323} & S_{3313} & S_{3312} \\ S_{2311} & S_{2322} & S_{2333} & 2S_{2323} & 2S_{2313} & 2S_{2312} \\ S_{1311} & S_{1322} & S_{1333} & 2S_{1323} & 2S_{1313} & 2S_{1312} \\ S_{1211} & S_{1222} & S_{1233} & 2S_{1223} & 2S_{1213} & 2S_{1212} \end{bmatrix} \quad (5.11)$$

However, the form in (5.11) can be considerably simplified with only components S_{1111}, S_{1122}, S_{1212} since all other non-zero components can be related to S_{1111}, S_{1122}, S_{1212} assuming the material of ceramics struts has isotropic mechanical properties. The non-zero components in Eshelby tensors are introduced by Mura [134]:

$$S_{1111} = S_{2222} = S_{3333} = \frac{7-5v_m}{15(1-v_m)},$$
$$S_{1122} = S_{2233} = S_{3311} = S_{1133} = S_{2211} = S_{3322} = \frac{5v_m - 1}{15(1-v_m)}, \quad (5.12)$$
$$S_{1212} = S_{2323} = S_{3131} = \frac{4-5v_m}{15(1-v_m)}$$

The v_m is the Poisson ratio for the base materials (composite ceramics). Taking into account the general form of Eshelby tensor given by Schjødt-Thomsen [130], one can therefore calculate the components of Eshelby tensor from (5.12), and substitute into equation (5.3) in order to perform calculation, taking into account of volume fraction of cavity in ceramics foam of 8PPI c_2=0.8283 and hence c_1=0.1386, then (5.2) becomes:

$$C_{ijkl}^{eff} = C_{ijkl}^{1} - 0.8283 \cdot C_{ijst}^{1} \cdot T_{stpq} \left[0.1717 \cdot I_{pqmn} + 0.8283 \cdot T_{pqmn} \right]^{-1} \quad (5.13)$$

Where $T_{stpq}=(I_{stpq}-S_{stpq})^{-1}$, therefore the effective stiffness tensor of ceramics foam of 8 PPI is obtained. The Young's modulus of ceramics foam can be obtained from (5.9). The modulus is calculated to be 8.991 GPa. Similarly, the same procedures applied to obtain effective modulus of 22 PPI foam with cavity fraction of 0.87 sintered at 1250 ^{o}C for 2 h gave the value of 6.86 GPa.

Unfortunately, the modelling with MT method also shows poor agreement with experiment. This is somehow beyond our expectation prior to the simulation as MT method has proved its effectiveness in many cases that is superior to other models. The likely source of this discrepancy is attributed to hollow structure of ceramics struts instead of being dense struts as illustrated in Fig. 4.37. The hollow structures are demonstrated by CT. The hollow structure was left due to burning-out of polymer replica could considerably decrease the mechanical properties of cellular structure. Moreover, the struts with hollow structure are not considered in micromechanical approach with assumption that the inclusion has to be spherical. In addition to this, lack of knowledge of distribution of the cell size and approximation of cavity could also affect the result which is yet to be studied. In one word, MT method predicting stiffer properties of ceramic foams compared to Christensen model is likely to match the experiment when the struts ceramics are completely dense instead of being hollow. We want to stress the aforementioned study does not suggest Christensen model is superior to MT method. For instance, when cell cavity approach to 0, meaning the material becomes completely dense, hence, the simulation should give properties of dense material. In case of Christensen model, the Young's modulus is 34 GPa. Instead, MT model gives 99 GPa when the C_2 is 0. This proves the numerical effectiveness of MT method in simulating of all

scenarios. Hence, the internal crack and defect are considered as main source of error.

5.3 Tomography based Finite Element Analysis

The Finite Element Analysis is carried out based on the 3D structure from X-ray tomography. However, a calculation for large structure such as seen in Fig. 4.38 or Fig. 4.41 requires more elements in calculation which is usually very difficult to carry out on personal computer. Therefore we chose a relative small structure but showing the same porosity~82% to the ceramics foam of larger scale. The structure in Fig. 5.1 is cut from the larger 3D structure of original scanned volume in AMIRA software.

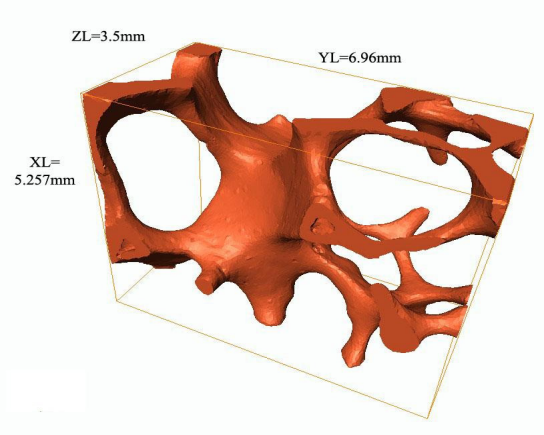

Fig. 5.1: 3D reconstructed structure of 8 PPI ceramics foam by Tomography

In actual FEA simulation, the displacement instead of force was applied to the top surface of the structure in Fig. 5.1. The volume is set free to expand except the bottom surface is fixed with zero displacement for compression condition. The materials parameters such as Young's modulus and Poisson ratio are adopted from the IE measurement in Chapter 4. When the cellular structure is compressed downward, the stress will produced at the cell edges. The stress is simulated for 0.7% strain and the reaction force is calculated as resultant force from displacement.

Oliveira et al [82] studied the modulus of the cordierite bulk ceramics and demonstrated E=88±10 GPa. The measurement was performed using the same technique. However, the modulus was found to be 99±2 GPa in case of 1350 ^{o}C of 2 h. This was not surprising since bulk ceramics are not monolithic but a composite containing ~20 wt.% mullite with higher modulus of 150 GPa. The composite also has ~10% porosity, therefore the composite modulus

should fall in between cordierite modulus E=70 GPa to Mullite E=150 GPa. In the meantime, the Poisson ratio is measured experimentally v=0.267. One more assumption is also made that the bulk cordierite is isotropic materials in terms of mechanical properties and does not exhibit orientational properties. Therefore the modulus and Poisson ratio are taken as materials properties parameter to calculate the reaction force on the structure.

It is well known that ceramics are very hard but brittle; therefore, it is not easy to machine the ceramic foams with a perfect flat surface. Some alternative approach is used by inserting soft polymer or rubber compliance layer between the compression plate and the top surface of the ceramics foam. However, we did not follow this approach successfully and the ceramics still crack very suddenly before it can be firmly touched and compressed. Meanwhile, the fractured piece of ceramics is extremely hard and tears off the polymer or rubber compliance. In order to study Compression strength the stress at displacement when ceramics structure with more than 50% structure fractures, we performed this study in FEM simulation. We compared to flexural strength of to the batch of ceramics which is sintered and supposedly has the fracture strength, σ_f=92 MPa to strut of ceramic foams. This strut is supposed to break and hence removed in simulation when the stress of strut exceeds σ_f. The elastic deformation has to end and further compression could only break the ceramics structure.

It should be noted that stress values used in this calculation to evaluate the ceramics fracture behaviour is based on Von Mises (VM) stress. In materials science and engineering the Von Mises stress is formulated in terms of the principal stress:

$$\sigma_v = \sqrt{\frac{(\sigma_1 - \sigma_2)^2 + (\sigma_2 - \sigma_3)^2 + (\sigma_1 - \sigma_3)^2}{2}} \quad (5.14)$$

σ_1, σ_2, σ_3 are principal stress components which are defined elsewhere [135] for further interests. The significant of the VM stress lies with fact that it is used as typical criterion in predicting of yield point under multi-axial complex loading conditions using results at which point the simple uniaxial stress (principal) results [98]. The VM stress represents the maximum surface stress generated at specific location. The fracture criterion is beyond scope of this study and therefore we only use the VM stress to predict the material fracture behaviour when the VM stress exceeds the flexural strength measured experimentally.

The FEM simulation is carried out in a continuous step from zero displacement until the flexural strength has been exceeded certain % that created disconnection of the structure.

Table 5.1 shows the steps we used in the FEM simulation for the structure of 8 PPI foam in Fig. 5.1. Considering the variation of the compressive properties is only linear within elastic regime, only 3 steps are chosen to obtain linear property.

Table 5.2: list of steps in FEM calculation

Steps	Displacement (mm)	Strain
1	0.0025	0.00071
2	0.005	0.0014
3	0.025	0.0071

Fig. 5.2 (a) shows the contour plot of the VM stress and the scale of stress in terms of colour at right top corner. We can see that the highest stress concentrated at thinnest cell edges and somewhere close to the cell edges. The contour plot is calibrated with 68 MPa as threshold therefore the more reddish in structure the higher the Von Mises stress. However, under such small strain only small portion of the structure has exceeded the flexural strength and supposed to fracture as shown in Fig. 5.2 (b) by removing those elements with VM stress higher than 68 MPa. The 68 MPa was obtained from flexural strength measurement of bulk ceramics prepared from the same batch of slurry for the struct of foam obtained. In Fig. 5.2 (b), we conclude that the fracture of few cell edges will not likely make the whole structure fail completely.

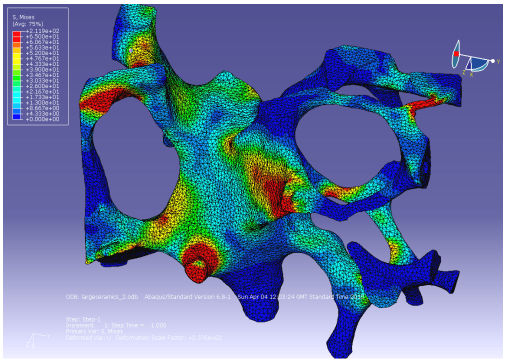

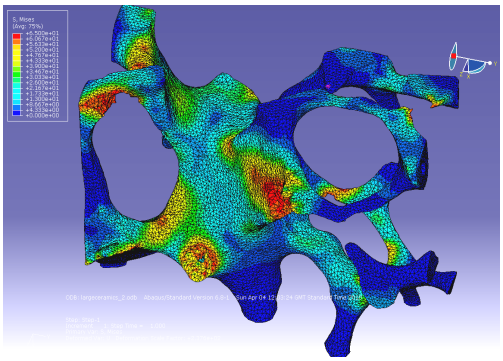

Fig. 5.2(a): stress at strain 0.00071; *Fig. 5.2(b): fracture pattern at strain 0.00071*

Fig. 5.3(a) shows the VM stress distribution under higher strain. Now the portion with stress that has exceeded the flexural strength is much more than that in Fig. 5.2(a). Similarly we also illustrate the fracture pattern in which the elements more than flexural strength is removed. However, as one can see in Fig. 5.3(b), although the portion which is likely to fail

has increased but the main structure still remain intact and we will expect some fluctuation of the compression force in experiment due to structure that fails. This expectation is in agreement with the typical static compression measurement of ceramics foam.

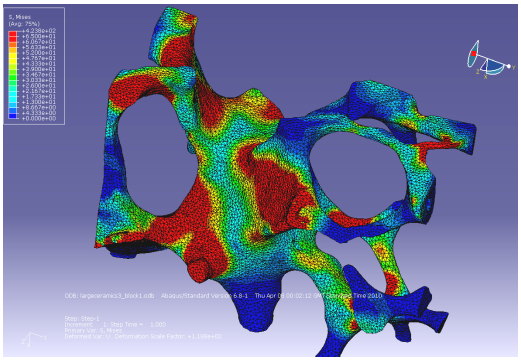

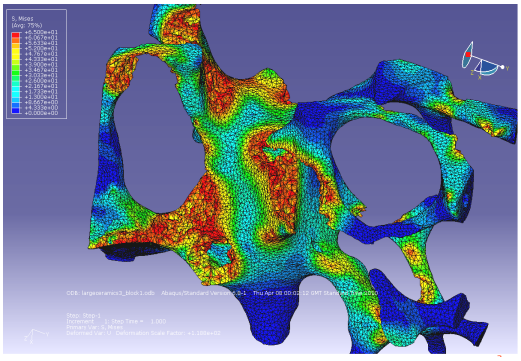

Fig. 5.3(a): Mises stress under strain 0.0014; Fig. 5.3(b): fracture pattern under strain 0.0014

In Fig. 5.4 (a) and Fig. 5.4 (b) we show the VM stress distribution and fracture pattern with a larger displacement and strain at 0.0071. Now the portion with stress more than flexural strength has dramatically increased and the fracture pattern shows that more than 50 vol.% of structure has completely failed and the structure is unlikely to keep stable and hence the foam is expected to fail catastrophically.

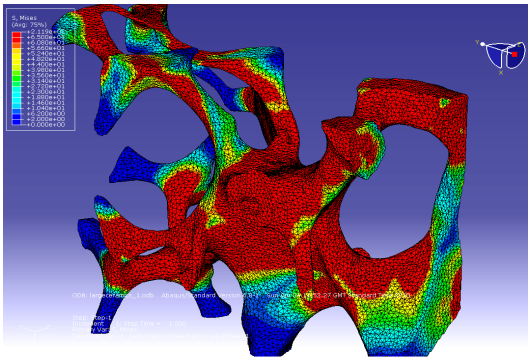

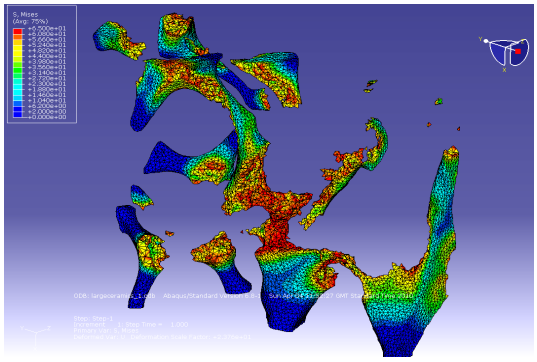

Fig. 5.4(a): stress at 0.007 strains; *Fig. 5.4(b): fracture pattern at strain 0.007*

Fig. 5.4 also demonstrates that in order to have elastic deformation before the structure fractures, one must apply at least much less than 0.007 strain to the sample in case of perfect specimen geometry conditions. In our compression test, the sample has height of 5 mm, therefore the deformation of the sample within the elastic regime will be less than 3.5 μm. This is not easy, or is even impossible, since the sample surface has roughness which is much

more than 3.5 μm. In addition, the machine has typical step of 1~2 μm ramp and if the elastic region is not more than 3.5 μm for our sample, the compression stress-strain curve will have too few points to study the modulus.

The reaction force corresponding to the displacement along unidirectional Z axis is calculated for each step as seen in Table 5.3. The apparent stress on the foam during compression is then obtained as well as Young's modulus. In addition to this, the porosity is also determined by 3D image analysis and the cavity fraction is determined for the section of volume in Fig. 5.1 is around 0.8456. This porosity study is necessary to ensure that the structure studied in FEM analysis is as consistent as possible to that in reality due reduced structure.

Table 5.3: calculated reaction force, apparent stress

Reaction force (N)	Apparent stress (MPa)
45.26	1.235
90.52	2.47
452	12.35

From Table 5.3, the Young's modulus of elastic deformation is determined as 1.729 GPa. The experimental value of Young's modulus from IE measurement is 0.97 GPa. The agreement improves significantly compared to analytical model in previous section. The reason we found such agreement is due to the fact only tomography could render 3D actual structure including all structural defects, e.g hollow structure of the struts or irregularities in the modelling. In addition to the Young's modulus, the compressive strength at which the ceramics foam will break is also investigated by FEA method which is not available in any other methods of analytical model. From Fig. 5.3 and Fig. 5.4, we discovered that the ceramics cellular structure completely failed at 0.007 strains and this is indication that the compressive strength must be below the stress applied at strain of 0.007. The stress was calculated by FEA at such strain as 2.47 MPa. The result from compression study in Chapter 5 suggested that the compressive strength of 8 PPI foam was 0.078 MPa. It is speculated that although the agreement between FEA result and experiment was large, however, the main error should come from the compression test due to irregularity of the sample dimension. The compressive strength should increase in case of perfect machining of the compressed surface. Therefore FEA study provided an potential mean to evaluate the compressive strength of the cellular structure, which is otherwise unpredictable in particular in case of brittle material.

In abovementioned case, the FEA modelling was only applied to the case of 8 PPI foam due to the model is only available for this case. We have not conducted yet FEA modelling to foams of 22 PPI produced with different processing specifications. However, the study demonstrated best agreement up to date and effectiveness of CT-FEA modelling and further collaboration with X-ray tomography lab is being sought.

5.4 Conclusive marks and future works

Bulk ceramics and ceramics foam made of cordierite and mullite as well as corundum or quartz are produced and characterized with compositional, microstructural and thermo-mechanical properties. Bulk ceramics showed a Young's modulus around 96-99 GPa and flexural strength at room temperature between 90-120 MPa. The composition of starting materials was revealed by XRD containing talc, corundum, quartz, feldspar and kaolinite as primary phase. The sintered product at variable temperature by XRD show maximum relative wt.% of cordierite at 1250 ^{o}C and further increasing the temperature for the same time of heat treatment is not effective in increasing the cordierite phase perhaps due to the Mg-containing compounds has depleted. The temperature XRD study also reveals that the formation of cordierite only takes place above 1250 ºC until the cordierite melt at 1460 ^{o}C. Sample sintered at 1425 ^{o}C showed dual phase of cordierite and mullite. The mechanical, thermal and dielectric properties are supposed to be optimized; however, an investigation is under way to verify this.

Mullite is found continuously increasing from the batch of raw powder upon heated from 950 ^{o}C. Above 1350 ^{o}C up to 1425 ^{o}C the cordierite wt.% fraction does not further increase when temperature rises due to Mg-deficiency however the SiO_2-Al_2O_3 continue to form mullite wit increasing wt.% and will transform to mullite completely at 1500 ^{o}C while cordierite has melt around 1460 ^{o}C. However the mullite specimen is macro-porous with visible crack and pores. This is due to liquid phase formation when cordierite melts and leave bubble entrapped inside the body after sintering. The mechanical strength was decreased significantly despite mullite has superior mechanical properties over cordierite in terms of bulk ceramics.

From the same batch of raw materials, it is found that not only sintering temperature but also the lasting time of sintering play critical role. For instance, at 1150 ^{o}C the powder sintered

for 2 h showed no sign of cordierite, but the same batch sintered for 4 h showed formation of cordierite low temperature polymorph, indialite. At 1350 ^{o}C, the batch sintered for 2 h showed only cordierite and XRD revealed that when the powder was sintered for 8 h, the transformation took place from cordierite to some spinel. However, the composition variation effect to mechanical or physical properties has not been investigated yet. But it is unlikely to affect the mechanical properties in a significant way as much as sintering temperature.

The thermal expansion studies suggest that 1350 ^{o}C is the optimal temperature in current investigation to give lowest TEC from the batch of original materials. However, further studies should be carried out between 1350 ^{o}C up to cordierite melting point 1460 ^{o}C. Also the time of heat treatment effect on the thermal properties should be also examined to support to invalidate the XRD result with variable time. It is expected that longer heat treatment will benefit the cordierite formation and depleted higher TEC materials such as Alumina.

SEM studies suggest that the porosity of bulk ceramics is around 10%. This result is compared to relative density by Pyconometry measurement and XRD composition study which determine the phase volume fractions of each constituents and hence the density of composite ceramics. The agreement was found well. The composite showed a TEC which is different from that of each ingredient materials, therefore the volume fraction of each ingredient is also used to model the TEC. Experiments pointed out that the ceramics bulk sintered at 1350^{o}C for 2h has good agreement with around 10% of porosity.

The lower TEC ensures very good thermal shock resistance (TSR) properties due to less thermal strain and hence stress generated in rapid heating or cooling. The cordierite composite with variable composition of mullite and alumina and SiO_2 are characterized by water quench method in line with ASTM standard. The experimental TSR is much higher than prediction and this is likely due to the porosity which acts as energy sink when the structure thermally expands. Further work is expected to perform in using FEA with thermal properties to simulate the thermal stress during rapid cooling to establish the scenario of thermal shock test.

Cordierite ceramics are potential materials in low-k and low current leakage applications in the IC industry. Therefore, dielectric properties measurement was carried out. The dielectric constant was found low within wide frequency range and around 7 at 1 MHz. The dielectric loss factor appears to be low as well. Therefore, the high modulus, relative high strength and good thermal shock resistance cordierite composite ceramics with abovementioned dielectric

properties is promising for electronic packaging industry.

Mori-Tanaka method was applied first to model the experiment for ceramics foam with averaging the cell morphology. Since the pores embedded in bulk ceramics are not considered equivalent to a sphere. Nevertheless, the effective modulus property is evaluated under assumption of spherical inclusion. The modelling shows a rough agreement. In the meantime, the modelling is based on 3D actual structure from CT experiment. This is supported with the fact that the strut of cellular structure is hollow which is different from other cellular materials that fully dense strut was found. The 3D actual structure was subject to FEA modelling in Abaqus/CAE and the best agreement between modelling and experiment is found for samples with 8 PPI pore size. This was an expected result since only CT rendered structure could take fully account of the defect and crack which affect the overall property of mechanical response. This CT-FEA modelling proves its usefulness in modelling material micromechanical behaviour under complex loading. Upon a full search of web of science, to the best our knowledge there is no such method or research has ever been conducted to ceramics foam yet. On the other hand, ceramics foam has become more and more popular product in today's academics and commercial market required urgent and more advanced characterization.

The future work is recommended in the following categories:

1) Improve the homogeneity of the foam by using suspension with smaller particle mean size and distribution. The suspension's viscosity should be further optimized with thickening agent and weight ratio between impregnated suspensions to polymer struts should be more closely controlled. Therefore, the shrinkage and deformation during drying and sintering could be reduced to minimum.
2) Extra efforts should be made to consider adding sintering additives to increase the densification, perhaps P_2O_5 or excessive MgO in order to obtain single phase of cordierite at lower temperature. From Rietveld refinement it appears that Mg-containing oxides have been depleted while corundum is still abundant. This is perhaps why the mullite is formed instead of cordierite between 1250-1350 ^{o}C. Work should be done with variable wt.% MgO or P_2O_5 added to the starting powder to see if the sintering temperature and cordierite fraction can be optimized and the properties-compositional relationship should be revisited.
3) The dielectric measurement is performed and the result was assuring its potential application. The dielectric constant show very low constant (7-10) depending on sintering schedule. Bearing that in mind the cordierite ceramics are supposed to be

used as low-dielectric loss materials. Therefore, further work should be also considered to increase the fraction of cordierite in the composite. In the meantime, the ceramic components could work at elevated temperature environment. The temperature-dependent dielectric properties of one representative samples were also characterized and analyzed. Study suggests the cordierite ceramics prepared from this non-standard powder has comparable or superior properties than commercial grade product and therefore continued efforts should be given.

4) The brittleness of bulk and cellular ceramics is one of most main disadvantages to limit the application of cordierite especially ceramics foam made of cordierite. CNTs are considered unlikely in oxygen-based ceramics for reinforcing agent due to thermal instability during sintering. However, a few works have shown a possibility of using Spark Plasma Sintering in reduced atmosphere to incorporate CNTs in alumina. Hence it is interesting to apply this technique in cordierite. Continuing efforts in searching technique to disperse and sintering cordierite with CNTs should be supported with encouragement of some researches that demonstrated successful reinforcement of mullite with CNTs reinforcement should be given attention in this regard.

5) A series of ceramic cellular materials made of e.g. ZrO, Alumina, SiC are developed for metal casting and catalyst converters. However, the cost of producing and applying such ceramic foams is high. The study above showed that cordierite-mullite composite has no advantageous properties compared to those ceramics aforementioned, i.e. the composite has flexural strength from 90~120 MPa whilst SiC has flexural strength of 500-1080 MPa. The Compression strength of cordierite foam is around 1-2 MPa and flexural strength of ceramics foam made of composite cordierite in this investigation while the SiC foam demonstrated Compression strength of 8-50 MPa and flexural strength of 3-30 MPa. However low cost of cordierite ceramics is attractive and therefore efforts should be continued to find the most optimized route. In addition, the material is supposed to be applied in thermo-mechanical engineering. The mechanical behaviour of cordierite at high temperature is expected to be visited.

6) Finally, FEM modelling should be considered by taking into account of thermal expansion coefficient which enables thermo-mechanical modelling of stress generated during quenching experiment. The modelling could be used to compare the experiment to simulate the defect dependent thermal shock resistance properties.

References

1. H. L. Lee, S. W. Nam, B. S. Hahn, B. H. Park and D. Han, *Joining of silicon carbide using MgO-Al_2O_3-SiO_2 filler.* Journal of Materials Science, 1998. **33**: p. 5007–5014.
2. M.V.Twigg, and J.T. Richardson, *Theory and Applications of Ceramic foam catalysts.* Chemical Engineering Research and Design, 2002. **80**: p. 183-189.
3. J.T. Richardson, Y.Peng, D. Remue, *Properties of ceramic foam catalyst supports: pressure drop.* Applied Catalysis A: General, 2000. **204**: p. 19-32.
4. Halstead, L.T., *Ceramic-matrix composite nozzle assembly for a turbine engine.* Composites, US Patent 4-861-229 (29 August 1989) 1991. **22**(1): p. 73-76.
5. G.A. Rankin, H. E. Merwin, *Ternary system MgO–Al_2O_3 –SiO_2.* J. Am. Ceram. Soc. , 1918. **45**: p. 301-325.
6. http://serc.carleton.edu/research_education/equilibria/ternary_diagrams.html.
7. S.M.Logvinkov, G. D. Semchenko, D.A.Kobyzeva, *Change in the phase composition of corrundum-mullite-cordierite refractories under heat treatment.* Refractories and Industrial Ceramics, 1997. **38**: p. 383-387.
8. *Rojan Cordierite ceramics*: www.rojan.au.com.
9. W.A. Deer, R. A. Howie, Y. Zussman, *Rock-forming minerals*. Double Chain Silicates 2001, vol. 2B: p.625. The Geological Society of London.
10. R. Müller, R. Naumann, S. Reinsch, *Surface nucleation of μ-cordierite in cordierite glass: thermodynamic aspects.* Thermochimica Acta, 1996. **280-281**: p. 191-204.
11. Johar Banjuraizah, H.M., Zainal Arifin Ahmad, *Thermal expansion coefficient and dielectric properties of non-stoichiometric cordierite compositions with excess MgO mole ratio synthesized from mainly kaolin and talc by the glass crystallization method.* Journal of Alloys and Compounds, 2010. **494**: p. 256–260.
12. P. W. Mirwald, *Thermal expansion of anhydrous Mg-cordierite between 25 and 950°C* Physics and Chemistry of Minerals, 1981. **7**(6): p. 268-270.
13. M.F. Hochella, Jr, G. E. Brown, Jr, *Structural Mechanisms of Anomalous Thermal Expansion of Cordierite-Beryl and Other Framework Silicates.* J. Am. Ceram. Soc., 1986. **69**(1): p. 13-18.
14. R. Roy, D. K. Agrawal, and H. A. McKinstry, *Very Low Thermal Expansion Coefficient Materials.* Annu. Rev. Mater. Sci., 1989. **19**: p. 59-81.
15. Costa Oliveira F. A, Dias S, Cruz Fernandes J., *Thermal Shock Behaviour of Open-cell Cordierite Foams.* Materials Science Forum, 2006. **514-516**: p. 764-767.
16. Z. Acimovica, L. Trumbulovic, L. Andricb, M. Stamatovic, *Synthesis and characterization of the cordierite ceramics from nonstandard raw materials for application in foundry.* Materials Letters, 2003. **57**: p. 2651-2656.
17. A.Yamuna, R. Johnson, Y.R. Mahajan, M. Lalithambika, *Kaolin-based cordierite for pollution control.* Journal of the European Ceramic Society, 2004. **24** p. 65–73.
18. S. H. Knickerbocker, A. H. Kumar and L. W. Herron, Am. Ceram. Soc. Bull., 1993. 72: p. 90.
19. D. PAL, A. K. Chakraborty, Suchitra Sen, S. K. Sen, *The synthesis, characterization and sintering of sol-gel derived cordierite ceramics for electronic applications.* Journal of Materials Science, 1996. **31**(15): p. 3995-4005.
20. Luo L., Zhou H., Xu C., *Synthesis, characterization, and sintering of sol-gel derived cordierite ceramics for high-frequency MLCIs.* Journal of Materials Science: Materials in Electronics, 2002. **13**: p. 381-386.
21. Guo-hua Chen, *Effect of ZnO addition on properties of cordierite-based glass-ceramics.*

Journal of Materials Science:Materials in Electronics, 2007. **18**(12): p. 1253-1257.
22. B. Zhang, C. Cao, H. Zhu, G. Li., *Preparation low dielectric constant material of cordierite with polyacrylamide gel method.* Journal of Materials Science, 2005. **40**: p. 1781-1783.
23. M.Terada, K.Kawamura, I. Kagomiya, K. Kakimoto and H. Ohsato, *Effect of Ni substitution on the microwave dielectric properties of cordierite.* Journal of the European Ceramic Society, 2007. **27**: p. 3045-3048.
24. MORRELL, R., Proc. Br. Ceram. Soc. , 1979. 28: p. 53.
25. R.R. Tummala, *Ceramic and Glass-Ceramic Packaging in the 1990s*. J. Am. Ceram. Soc., 1991. **74**: p. 895-908.
26. Nandi, A.K., *Thermal Expansion Behavior of Boron-Doped Cordierite Glass-Ceramics.* J. Am. Ceram. Soc., 1999. **82**(3): p. 789-790.
27. Yi Hu and H.-T. Tsai *Compositional effect on the crystallization of the cordierite-type glasses.* Journal of Materials Science, 2001. **36**(1): p. 123-129.
28. T. A. Khabas, V. I. Vereshchagin, T. V. Vakalova, A. A. Kirchanov, N. A. Kulikovskaya and N. G. Kozhevnikova *Low-Temperature Synthesis Of The Cordierite Phase In Ceramic Mixtures Of Natural Raw Materials.* Refractories and Industrial Ceramics, 2003. **44**(3): p. 181-185.
29. B. Johar., M. Hasmaliza, Ahmad, Z. A. Ahmad, *Crystal structure of single phase and low sintering temperature of alpha-cordierite synthesized from talc and kaolin.* Journal of Alloys Compound, 2009. **482**: p. 429-436
30. V. N. Antsiferov, S. E. Porozova, S. N. Peshcherenko, *Effect of the Raw Materials on the Properties of Cordierite Ceramics.* Refractories and Industrial Ceramics, 1997. **38**(9-10): p. 388-391.
31. N. V. Pitak, *Morphological Characteristics of Mullite: An Important Factor for Evaluating the Quality of Refractories.* Refractories and Industrial Ceramics, 1997. **38**(7-8): p. 274-277.
32. A. A. Griffith, A. A. *The Phenomena of Rupture and Flow in Solids*. *Phil. Trans R. Soc. Lond*., 1920 **A221**: p.163-198
33. L. Zhang, E.Yilmaz, J. Rauhe, J. Thomsen, *Multi-wall carbon nanotube reinforced Polyurethane foam processing and Mori-Tanaka modelling of the mechanical properties.* Composites Science and Technology, 2010. (In press).
34. HansangKwon, Dae Hoon Park, Jean François Silvaina, Akira Kawasaki, *Investigation of carbon nanotube reinforced aluminium matrix composite materials.* Composites Science and Technology, 2010. **70**(3): p. 546-550
35. Hansang Kwon, M.E., Kenta Takagi, Takamichi Miyazaki, Akira Kawasaki*, *Combination of hot extrusion and spark plasma sintering for producing carbon nanotube reinforced aluminum matrix composites.* Carbon, 2009. **47**: p. 570-577.
36. K. Morsi, A.M.K. Esawi, S. Lanka, A. Sayed, M. Taher, *Spark plasma extrusion (SPE) of ball-milled aluminium and carbon nanotube reinforced aluminium composite powders.* Composites Part A: Applied Science and Manufacturing, 2010. **41**: p. 322-326.
37. Wu-Bian Tian, Yan-Mei Kan, Guo-Jun Zhang, Pei-Ling Wang, *Effect of carbon nanotubes on the properties of ZrB_2-SiC ceramics.* Materials Science and Engineering A 2008. **487:** p. 568-573.
38. Sriharsha Pasupuleti, Ramseshu Peddetti, Sridhar Santhanam, Kei-Peng Jen, Zachary N. Wing, Mathias Hecht and Joseph P. Halloran, *Toughening behavior in a carbon nanotube reinforced silicon nitride composite.* Materials Science and Engineering: A, 2008. **491**(1-2): p. 224-229.

39. Johann Cho, Aldo R. Boccaccini, Milo S. P. Shaffer, *Ceramic matrix composites containing carbon nanotubes.* Journal of Materials Science, 2009. **44**(8): p. 1934-1951.
40. Mehdi Estili, Hansang Kwon, Akira Kawasaki, Seungchan Cho, Kenta Takagi, Keiko Kikuchi, Masayoshi Kawai, *Multiwalled carbon nanotube-reinforced ceramic matrix composites as a promising structural material.* Journal of Nuclear Materials, 2009. **398**: p. 244-245.
41. Mehdi Estili, Akira Kawasaki, Hiroki Sakamoto, Yutaka Mekuchi, Masaki Kuno, Takayuki Tsukada, *The homogeneous dispersion of surfactantless, slightly disordered, crystalline, multiwalled carbon nanotubes in a-alumina ceramics for structural reinforcement.* Acta Materialia, 2008. **56**: p. 4070-4079.
42. Mehdi Estili, Akira Kawasaki, *Engineering Strong Intergraphene Shear Resistance in Multi-walled Carbon Nanotubes and Dramatic Tensile Improvements.* Advanced Materials, 2010. **22**: p. 607-610.
43. J. Wang, H. Kou, X. Liu, Y. Pan, J. Guo, *Reinforcement of mullite matrix with multi-walled carbon nanotubes.* Ceramics International, 2007. **33**: p. 719-772.
44. J.T. Oh, P.Hing, H.S. Fong, S.F. Chin, C.L. Zeng, *The processing of cordierite glasses containing AIN.* Journal of Materials Processing Technology, 1997. **63**: p. 851-854.
45. J. Ma, K. Liao, P. Hing, *Effect of aluminium nitride on the properties of cordierite.* Journal of Materials Science, 2000. **35**(16): p. 4137-4141.
46. E. M. Dyatlova, G. Ya. Minenkova and T. V. Kolontaeva, *Intensification Of Sintering Of Mullite-Cordierite Ceramics Using Mineralizers.* Glass and Ceramics, 2000. **57**(11-12): p. 427-430.
47. R. Gopi Chandran, K. C. Patil and G. T. Chandrappa, *Combustion synthesis, characterization, sintering and microstructure of mullite-cordierite composites.* Journal of Materials Science Letters 1995. **14**(8): p. 548-551.
48. O. A. Belogurova and N. N. Grishin, *Modified Mullite-Cordierite Materials.* Refractories and Industrial Ceramics, 2009. **50**(5): p. 368-371.
49. M.A. Camerucci, G.U., M.S. Castro, A.L. Cavalieri, *Electrical properties and thermal expansion of cordierite and cordierite-mullite materials.* Journal of the European Ceramic Society, 2001. **21**: p. 2917–2923.
50. Junichi Takahashi, Y.K., Shiro Shimada, *Hot corrosion of cordierite/mullite composites by Na-salts.* Journal of the European Ceramic Society, 2002. **22**(12): p. 1959-1969.
51. Emel Ozel, S.K., *Effect of the processing on the production of cordierite–mullite composite.* Ceramics International 2010. **36**: p. 1033–1039.
52. M. A. Camerucci, G.U., A. L. Cavalieri, *Mechanical behavior of cordierite and cordierite-mullite materials evaluated by indentation techniques.* Journal of the European Ceramic Society, 2001. **21**(9): p. 1195-1204.
53. Junichi Takahashi, Maya Natsuisaka and Shiro Shimada, *Fabrication of cordierite-mullite ceramic composites with differently shaped mullite grains.* Journal of European Ceramics Society. **22**(4): p. 479-485.
54. Young-Jei Oh, Tae-Sung Oh, Hyung-Jim Jung, *Microstructure and mechanical properties of cordierite ceramics toughened by monoclinic ZrO_2.* Journal of Materials Science 1991. **26**: p. 6491-6495.
55. M. AWANO, and H. Takagi, *Synthesis of cordierite and cordierite-$ZrSiO_4$ composite by colloidal processing.* Journal of Materials Science, 1994. **29**(2): p. 412-418.
56. F. A. Costa Oliveira and J. Cruz Fernandes, *Mechanical and thermal behaviour of cordierite-zirconia composite.* Ceramics International, 2002. **28**(1): p. 79-91.
57. T. D. Senguttuvan, H.S.K., S. K. Sharda, B. K. Das, *Sintering behavior of alumina rich cordierite porous ceramics* Materials Chemistry and Physics, 2001. **67**(1-3): p.

146-150.
58. T. M. Ul'yanova, N. P. Krut'ko, Yu. V. Matrunchik, E. M. Dyatlova, E. S. Paémurd, *A Thermostable Composite Ceramic Based On Cordierite.* Glass and Ceramics, 2006. **63**(11-12): p. 411-414.
59. Seiichi Taruta, Takeshi Hayashi and Kunio Kitajima, *Preparation of machinable cordierite/mica composite by low-temperature sintering.* Journal of the European Ceramic Society, 2004. **24**(10-11): p. 3149-3154
60. Sen Mei, Juan Yang, José M. F. Ferreira, *The densification and morphology of cordierite-based glass-ceramics* Materials Letters, 2001. **47**(4-5): p. 205-211.
61. E.M. Hamzawy, A.A. El-Kheshen, M.F. Zawrah, *Densification and properties of glass/cordieritenext term composites.* Ceramics International, 2005. **31**(3): p. 383-389.
62. Sung, Y.M., *Mechanical and Thermal Properties of Graphite Fiber-Reinforced Cordierite Glass-Ceramic Matrix Composites.* Journal of Materials Science Letters, 1999. **18**(8): p. 647-649.
63. Haikui Zhu, Hongqing Zhou, Ying Xie, Min Liu, *Study on properties of forsterite/cordierite ceramic composites.* J Mater Sci: Mater Electron 2010. **21**(3): p. 231–235.
64. M. Dimitrijevic, M. Posarac, J. Majstorovic, T. Volkov-Husovic, and B. Matovic, *Behavior of silicon carbide/cordierite composite material after cyclic thermal shock.* Ceramics International 2009 **35**(3): p. 1077–1081.
65. Sumin Zhu, S.D., Hong'an Xi, Qin Li, Ruoding Wang, *Preparation and characterization of SiC/cordierite composite porous ceramics.* Ceramics International, 2007. **33**(1): p. 115-118.
66. I. Wadsworth, R. Stevens, *The influence of whisker dimensions on the mechanical properties of cordierite/SiC whisker composites.* Journal of the European Ceramic Society, 1992. **9**(2): p. 153-163.
67. I. Wadsworth, R. Stevens, *Strengthening and toughening of cordierite by the addition of silicon carbide whiskers, platelets and particles.* Journal of Materials Science, 1991. **26**: p. 6800-6808.
68. Shifeng Liu, Yu-Ping Zeng and Dongliang Jiang, *Fabrication and characterization of cordierite-bonded porous SiC ceramics.* Ceramics International,2009. **35**(2): p. 597-602.
69. D. M. Ibrahim, S. M. Naga, Z. Abdel Kader and E. Abdel Salam, *Cordierite-Mullite Refractories.* Ceramics International 1995. **21**: p. 265-269.
70. M. Posarac, M. Dimitrijevic, T. Volkov-Husovic, A. Devecerski, B. Matovic, *Determination of thermal shock resistance of silicon carbide/cordierite composite material using nondestructive test methods.* Journal of the European Ceramic Society 2008. **28** p. 1275–1278.
71. Stanisava Marenovic, M.D., Tatjana Volkov Husovic, Branko Matovic, *Thermal shock damage characterization of refractory composites.* Ceramics International 2008. **34** p. 1925–1929.
72. M. Posarac, Marija Dimitrijevic, T. Volkov-Husovic, J. Majstorovic, B. Matovic, *The ultrasonic and image analysis method for non-destructive quantification of the thermal shock damage in refractory specimens.* Materials and Design, 2009. **30**: p. 3338–3343.
73. Aksel, C.,*Mechanical properties and thermal shock behaviour of alumina–mullite–zirconia and alumina–mullite refractory materials by slip casting.* Ceramics International, 2003. **29:**p. 311–316.
74. A. Yamuna, S. Honda, K. Sumita, M. Yanagihara, S. Hashimoto, H. Awaji, *Synthesis, sintering and thermal shock resistance estimation of porous cordierite by IR heating*

technique. Microporous and Mesoporous Materials, 2005. **85:** p. 169–175.
75. A. G. Tomba Martinez, M. A. Camerucci, A. L. Cavalieri, *Thermal stress analysis of cordierite materials subjected to thermal shock.* Journal of Materials Science, 2008. **43**: p. 2731–2738.
76. Rathindra Nath Das, C. D. Madhusoodana, P. K. Panda, Kiyoshi Okada, *Evaluation of thermal shock resistance of cordierite honeycombs.* Bulletin of Materials Science, Indian Academy of Sciences., 2002. **25**(2): p. 127-132.
77. Shiang-Po Hwang, Jenn-Ming Wu, *Effect of Composition on Microstructural Development in MgO–Al_2O_3–SiO_2 Glass-Ceramics.* J. Am. Ceram. Soc., 2001. **84**(5): p. 1108–1112.
78. Marta Valášková, Martynková Gražyna Simha, *Preparation and Characterization of Porous Cordierite for Potential Use in Cellular Ceramics.* Chemical Papers, 2009. **63**(4): p. 445-449.
79. L.Montanaro, Y. Jorand, G.Fantozzi, A.Negro, *Ceramic Foams by Powder Processing* Journal of the European Ceramic Society, 1998. **18**: p. 1339-1350.
80. Jai Koo Park, Jung Shick Lee and Seung In Lee, *Preparation of Porous Cordierite Using Gel casting Method and its Feasibility as a Filter.* Journal of Porous Materials, 2002. **9**: p. 203-210.
81. João B. Rodrigues Neto, R.M., *Rheological behaviour of kaolin/talc/alumina suspensions for manufacturing cordierite foams.* Applied Clay Science, 2007. **37**: p. 157-166.
82. F.A.Costa Oliveira, S. Dias, M.Fatima Vaz, J.Cruz Fernandes, *Behaviour of open-cell cordierite foams under compression.* Journal of the European Ceramic Society, 2006. **26**: p. 179-186.
83. Olhero, S., *Characterization of ceramic suspensions and Studies to optimize the burning of polymeric foam.* Project: CORDFOAM. **Anexo V**.
84. H. Taib, C.C.S., *Journal of the Australian Ceramic Society.* 2008. **44**(4): p. 47-51.
85. D. Swift, et al. 2000: http://web.ges.gla.ac.uk/~dswift/ls230.pdf.
86. Rietveld, H.M., *Line profiles of neutron powder-diffraction peaks for structure refinement.* Acta Cryst., 1967. **22**: p. 151-152.
87. Rietveld, H.M., *A Profile Refinement Method for Nuclear and Magnetic Structures.* J. Appl. Cryst., 1969. **2**: p. 65-71.
88. Lutterotti, L., *Quantitative phase analysis and errors* http://users.unimi.it/mzucali/Didattica/text_2009/PDFs/QPA.key.pdf
89. Lutterotti, L., *Introduction to Rietveld refinements* http://www.ccp14.ac.uk/ccp/web-mirrors/lutterotti/~luttero/laboratoriomateriali/Rietveld.pdf.
90. Brian O'Connor, Deyu Li., *Influence of Refinement Strategies on Rietveld Phase Composition Determinations.* JCPDS-International Centre for Diffraction Data 2000, Advances in X-ray Analysis, 1998. **42**: p. 204-211 . http://www.icdd.com/resources/axa/vol42/V42_22.pdf
91. Allen C. Larson, Robert B. Von Dreele, *General Structure Analysis System (GSAS).* Los Alamos National Laboratory Report, 2000. **LAUR 86-748**.
92. Lutterotti, L., *MAUD.* http://www.ing.unitn.it/~maud/index.html.
93. ASTM D1621-04a, *Standard Test Method for Compressive Properties of Rigid Cellular Plastics*.
94. S. Youssef, E. Maire, R. Gaertner, *Finite element modelling of the actual structure of cellular materials determined by X-ray tomography.* Acta Materialia 2005. **53**(3): p. 719-730.

95. D.U.Tulyaganov, H. R. Fernandes, S. Agathopoulos, J.M.F.Ferreira, *Preparation and Characterization of high compressive strength foams from sheet glass.* Journal of Porous Materials, 2006. **13**: p. 133-139.
96. http://upload.wikimedia.org/wikipedia/commons/e/ec/Threepoint.jpg.
97. ASTM D790, *Standard test methods for flexural properties of unreinforced and reinforced plastics and electrical insulating materials.*
98. *Von Mises stress.* http://en.wikipedia.org/wiki/Von_Mises_yield_criterion.
99. ASTM E1876., *Standard Test Method for Dynamic Young's Modulus, Shear Modulus, and Poisson's Ratio for Advanced Ceramics by Impulse Excitation of Vibration.*
100. K.K. Phani, D.Sanyal., *The relations between the shear modulus, the bulk modulus and Young's modulus for porous isotropic ceramic materials.* Materials Science and Engineering A, 2008. **490**: p. 305-312.
101. ASTM C1525-04, *Standard Test Method for Determination of Thermal Shock Resistance for Advanced Ceramics by Water Quenching.*
102. Morrell, R., *Hanbook of Properties of Technical & Engineering Ceramics Part 1 An Introduction for the Engineer and Designer* Her Majesty's Staionery Office, UK, 1985.
103. A.M. Trater, S. Alavia, and S.S.H. Rizvi, *Use of non-invasive X-ray microtomography for characterizing microstructure of extruded biopolymer foams.* Food Research International, 2005. **38**: p. 709-719.
104. Salvo L., Maire E, *X-ray micro-tomography an attractive characterisation technique in materials science.* Nuclear Instruments and Methods in Physics Research Section B: Beam Interactions with Materials and Atoms, 2003. **200**: p. 273-286.
105. Maire, E., *X Ray Tomography Study of Cellular Materials: Experiments and Modelling*, in *IUTAM book series, IUTAM Symposium on Mechanical Properties of Cellular Materials*. 2007: September 17-20, Cachan, France. p. 35-42.
106. F. Fischer, Lim G. T., Handge U. A., Altstädt V., *Numerical Simulation of Mechanical Properties of Cellular Materials Using Computed Tomography Analysis.* Journal of Cellular Plastics, 2009. **45**(5): p. 441-460.
107. M. Duchamp, J. D. Bartout, S. Forest, Y. Bienvenu, G. Walther, S. Saberi and A. Boehm, *Mechanical Behavior of Nickel Base Foams for Diesel Particle Filter Applications.* IUTAM Symposium on Mechanical Properties of Cellular Materials. 2009. vol.12: Springer, Netherlands.
108. A. Goel, D. Tulyaganov, Essam R. Shaaban, C.S. Knee, S. Eriksson, José M.F. Ferreira, *Structure and crystallization behaviour of some $MgSiO_3$-based glasses* Ceramics International, 2009. **35**(4): p. 1529-1538
109. J. M. F. Ferreira, *Role of the Clogging Effect in the Slip Casting Process.* Journal of the European Ceramic Society, 1998. **18**: p. 1161-1169.
110. Milewski, J.V., *Efficient use of whiskers in the reinforcement of ceramics.* Advanced Ceramic Materials, 1986. **1**: p. 36-41.
111. R. Johnson, I. Ganesh, B. P. Saha, G. V. Narasimha Rao and Y. R. Mahajan, *Solid state reactions of cordierite precursor oxides and effect of CaO doping on the thermal expansion behaviour of cordierite honeycomb structures.* Journal of Materials Science, 2003. **38**: p. 2953-2961.
112. Balek V., J.Šubrt, L.A.Pérez-Maqueda, M.Beneš, I.M.Bountseva, I.N. Beckman, J.L.Pérez-Rodríguez, *Thermal behavior of ground talc mineral.* Journal of Mining and Metallurgy, Section B: Metallurgy, 2008. **44**(1): p. 7-17.
113. J. R. González-Velasco, M. A. Gutiérrez-Ortiz, R. Ferret, A. Aranzabal, J. A. Botas, *Synthesis of cordierite monolithic honeycomb by solid state reaction of precursor oxides.* Journal of Materials Science, 1999. **34**: p. 1999-2002.

114. http://www.thermexcel.com/english/tables/eau_atm.htm.
115. M. Nouri. Khezrabadi, R. Naghizadeh, P. Assadollahpour and S.H. Mirhosseini, *An investigation on the properties and microstructure of mullite-bonded cordierite ceramics.* Journal of Ceramic Processing Research, 2007. **8**(6): p. 431-434.
116. Xu Xiao-hong, Wu Jian-feng, Hu Shu-guang, *Synthesis of Cordierite from Rectorite-Talc-Alumina without Additives.* Journal of Wuhan University of Technology-Mater.Sci. Ed., 2004. **19**(2): p. 14-16.
117. E. F. Sutormina, L. A. Isupova, N. A. Kulikovskaya, L. M. Plyasova, and N. A. Rudina, *Effects of Iron, Bismuth, and Vanadium Oxides on the Properties of Cordierite Ceramics*. ISSN, Kinetics and Catalysis, 2010. **51**(1): p. 131–134.
118. M. A. Montorsi, R. Delorenzo, E. Verne, *Cordierite-Cerium (IV) oxide system: Microstructure and properties*. Ceramics International, 1994. **20**: p. 353-358.
119. G. Bruno, A.M. Efremov, B. Clausen, A. Balagurov, V. Simkin, Bryan R. Wheaton, James E. Webb, Donald W. Brown, *On the stress-free lattice expansion of porous cordierite.* Acta Materialia 2010. **58** p. 1994–2003.
120. Bai Jiahai, Guo Lucun., *Effects of Chemical Treatments on Thermal Expansion Properties of Cordierite Ceramics.* Journal of Wuhan University of Technology- Mater. Sci. Ed., 2006. **21**(3): p. 100-102.
121. Lorna J. Gibson, Michael F. Ashby, *Cellular Solids: Structure and Properties*. 1997: Cambridge University Press, UK.
122. Susana Olhero, F. A. Costa Oliveira, *Design and construction of prototype equipment necessary for impregnation.* Projecto CORDFOAM Documento nº: 16, 2002.
123. *ImageJ,* http://rsbweb.nih.gov/ij/index.html.
124. *AMIRA*, *http://www.amira.com/*.
125. M. L. Sandoval, M. H. Talou, A. G. Tomba Martinez, M. A. Camerucci, *Mechanical testing of cordierite porous ceramics using high temperature diametral compression.* Journal of Materials Science, 2010. **45**: p. 1573-4803.
126. Sen Mei, Juan Yang, Xin Xu, Sandra Quaresma, Simeon Agathopoulos, José M.F. Ferreira, *Aqueous tape casting processing of low dielectric constant cordierite-based glass-ceramics—selection of binder.* Journal of the European Ceramic Society 2006. **26** p. 67-71.
127. B.H. Kim, K. H. Lee, *Crystallization and sinterability of cordierite-based glass powders containing CeO_2.* Journal of Materials Science, 1994. **29**(24): p. 6592-6598.
128. *low-dielectric materials.* http://en.wikipedia.org/wiki/Low-k_dielectric.
129. Eshelby, J.D., *The Determination of the Elastic Field of an Ellipsoidal Inclusion, and Related Problems.* Proceedings of the Royal Society of London. Series A, Mathematical and Physical Sciences, 1957. **241**(1226): p. 241.
130. Jan Schjødt-Thomsen, et al., *Continuum Mechanical Modelling of Composites and Cellular Materials Part1 Elasticity.* Task C: Mircromechanics and microstructure property correlations, 2003.
131. Christensen, R.M., *Mechanics of cellular and other low-density materials.* International Journal of Solids and Structures, 2000. **37**: p. 93-104.
132. T. Mori and K.Tanaka, *Average stress in matrix and average elastic energy of materials with misfitting inclusions.* Acta Metallurgica, 1973. **21**(5): p. 571-574.
133. Benveniste, Y., *A new approach to the application of Mori-Tanaka's theory in composite materials.* Mechanics of Materials, 1987. **6**(2): p. 147-157.
134. Toshio Mura, *Micromechanics of Defects in Solids, 2nd edition; 1991,* Dordrecht, the Netherlands, Kluwer Publishing.
135. “Mechanical stress”, http://en.wikipedia.org/wiki/Stress_(mechanics).